

# Optical Path Design and System Integration for High Speed Scanning Lever Atomic Force Microscopes

## DISSERTATION

Ausgeführt zum Zwecke der Erlangung des akademischen Grades eines  
Doktors der technischen Wissenschaften (Dr.techn.)

unter der Leitung von  
Univ.-Prof. Dr.sc.techn. Georg Schitter

eingereicht an der  
Technischen Universität Wien  
Fakultät für Elektrotechnik und Informationstechnik

von  
Dipl.-Ing. Jürgen Steininger

Matrikelnummer: 0226024

Millergasse 17/2/20  
1060 Wien, Österreich

Wien, im August 2015

---

Technische Universität Wien  
Karlsplatz 13, 1040 Wien, Österreich

---

---

## Danksagung

---

Für die ausgezeichnete wissenschaftliche Betreuung meiner Arbeit bedanke ich mich bei Herrn Univ.Prof. Dr. Georg Schitter. Weiters möchte ich mich bei allen Kollegen an der TU Wien für die vielen interessanten Diskussionen und die Unterstützung meiner wissenschaftlichen Arbeit bedanken.

Ganz besonders möchte ich mich an dieser Stelle bei meinen Eltern für die bisherige Unterstützung auf meinem Lebens- und Ausbildungsweg bedanken. Ein spezieller Dank gilt auch meiner Lebensgefährtin Brigitte, welche mit ihrer Motivation und Unterstützung wesentlich zum Gelingen dieser Arbeit beigetragen hat. Abschließend möchte ich mich bei allen Freunden für die stete Unterstützung in beruflichen und privaten Angelegenheiten bedanken.

---

## Abstract

---

Since the invention in 1986 the atomic force microscope (AFM) became one of the most important tools for imaging, metrology, and manipulation of matter at the nanoscale. In contrast to other nanoscale imaging tools the AFM works under various environmental conditions as vacuum, air, and liquid. Therefore the instrument is used by many physicists and biologists as well as in industrial applications, e.g. in the semiconductor industry.

The working principle is to probe the surface of the sample by a sharp tip mounted on the free end of a micro cantilever while raster scanning the sample and tip relatively to each other. The major drawback utilizing AFMs is the slow imaging speed by acquiring the image line by line. Although recent work shows that imaging is possible with several thousand lines per second, the size and mass of the sample is very limited as in these systems the sample is scanned against a fixed cantilever.

Imaging large samples is best done by using so called scanning lever systems, where the cantilever instead of the sample is scanned in x-, y-, and z-direction. Although the actuation of the cantilever can be done in a similar way as the actuation of the sample in conventional AFM systems, the integration of the optical system, that is used to measure the cantilever deflection, is far more challenging as the optical path varies with the motion of the cantilever.

This theses focuses on the analysis, design, and evaluation of a high speed deflection readout system and its integration into high speed scanning lever AFMs. This results in a high bandwidth deflection readout system with a measurement bandwidth of 64.5 Mhz, and the realization of a new scanning lever AFM that allows high speed imaging with up to 625 lines/s.

---

## Zusammenfassung

---

Nach der Erfindung des Rasterkraftmikroskops (engl. Atomic Force Microscope, AFM) im Jahr 1986 entwickelte sich dieses zu einem grundlegenden Verfahren zur Abbildung, Vermessung und Manipulation von Oberflächen im Nanometer Bereich. Der Vorteil des AFMs gegenüber anderen bildgebenden Verfahren liegt vor allem im breiten Anwendungsbereich durch die Möglichkeit der Messung in unterschiedlichsten Umgebungen (Vakuum, Luft, Flüssigkeit,...). Häufige Anwendung findet das AFM sowohl im wissenschaftlichen Bereich, beispielweise durch Physiker und Biologen, als auch im industriellen Umfeld, beispielsweise durch die Halbleiterindustrie.

Das grundlegende Messprinzip besteht darin, die Oberfläche mit einer feinen Spitze, welche am freien Ende eines Federbalkens montiert ist, abzutasten. Eine wesentliche Einschränkung stellt die erreichbare Messgeschwindigkeit dar, welche durch das zeilenweise abtasten der Oberfläche beschränkt wird. Obwohl neuere Publikationen Messungen mit mehreren Bildern pro Sekunde zeigen, wird in diesen Systemen die Scanbewegung üblicherweise durch die Aktuation einer äußerst kleinen und leichten Probe erreicht.

Die Messung auf größeren Proben mit höherer Masse erfolgt üblicherweise durch sogenannte „Scanning Lever“ Systeme bei denen die Messspitze über der feststehenden Probe bewegt wird. Obwohl die Aktuation der Messspitze ähnlich zur Aktuation der Probe in herkömmlichen Systemen erfolgen kann, gestaltet sich die üblicherweise optisch durchgeführte Messung der Auslenkung des bewegten Federbalkens schwierig, da sich der optische Pfad durch die Aktuation verändert.

In dieser Arbeit erfolgt die Analyse, das Design und die Evaluation von neuen Ideen zur Integration des optischen Pfades in schnellen „Scanning Lever“ Systemen. Dabei wird sowohl ein Messsystem zur optischen Messung der Auslenkung des Federbalkens mit einer hohen Messbandbreite von 64.5 MHz sowie ein komplettes „Scanning Lever“ AFM entwickelt. Dieses neu entwickelte System erlaubt die Abbildung von Oberflächen auf der Nanometerskala mit bis zu 625 Linien pro Sekunde.

---

# Contents

---

<b>1</b>	<b>Introduction</b>	<b>1</b>
1.1	Scope of the thesis . . . . .	3
1.2	Outline . . . . .	3
<b>2</b>	<b>State-of-the-art</b>	<b>4</b>
2.1	Scanning principles . . . . .	4
2.1.1	Scanning sample . . . . .	4
2.1.2	Moving-z . . . . .	5
2.1.3	Scanning lever . . . . .	5
2.2	Modes of operation . . . . .	6
2.3	Components . . . . .	8
2.3.1	Sample . . . . .	8
2.3.2	Cantilever . . . . .	8
2.3.3	Deflection readout . . . . .	10
2.3.4	z-Actuator . . . . .	13
2.3.5	z-Feedback controller . . . . .	13
2.3.6	x/y-Scan stage . . . . .	14
2.3.7	Data acquisition . . . . .	16
2.3.8	User interface . . . . .	18
2.4	Research questions . . . . .	19
<b>3</b>	<b>High bandwidth deflection readout</b>	<b>20</b>
3.1	The deflection readout circuit . . . . .	20
3.1.1	Differential amplifiers . . . . .	22
3.1.2	Signal normalization . . . . .	24
3.1.3	The transimpedance amplifier . . . . .	24
3.2	The influence of the detector geometry . . . . .	27
3.2.1	Experimental verification . . . . .	28
3.2.2	Quadrant photodetector sensitivity . . . . .	31
3.3	Implementation and measurement results . . . . .	37
3.3.1	Selection of the QPD . . . . .	37

## Contents

3.3.2	Laser power considerations . . . . .	38
3.3.3	Selection of the feedback resistor . . . . .	38
3.3.4	Selection of the operational amplifier . . . . .	38
3.3.5	Selection of the feedback capacitor . . . . .	38
3.3.6	Bandwidth measurement setup . . . . .	39
3.3.7	Bandwidth measurement results . . . . .	39
3.3.8	Deflection noise measurement . . . . .	40
3.3.9	Conclusion . . . . .	41
<b>4</b>	<b>Crosstalk reduction by an optical design approach</b>	<b>43</b>
4.1	Crosstalk . . . . .	43
4.2	Compensation of the crosstalk . . . . .	45
4.3	Measurements . . . . .	45
4.4	Diffraction limited sensitivity . . . . .	50
4.5	The effect of an additional focusing lens on a diverging beam . . . . .	51
4.5.1	The spot size on the QPD . . . . .	52
4.5.2	Compensation of the crosstalk . . . . .	55
4.6	Conclusion . . . . .	56
<b>5</b>	<b>Scanning Lever AFM Design</b>	<b>57</b>
5.1	The design of the optical path . . . . .	57
5.1.1	Folding the optical path . . . . .	59
5.1.2	Ray tracing . . . . .	60
5.1.3	Folding the path according to a serial actuation configuration . . . . .	60
5.2	Realization of the three dimensional scanner . . . . .	69
5.2.1	z-Scanner . . . . .	69
5.2.2	x-Scanner . . . . .	71
5.2.3	y-Scanner . . . . .	73
5.2.4	Laser alignment on the cantilever . . . . .	73
5.2.5	Assembly . . . . .	75
5.3	Conclusion . . . . .	76
<b>6</b>	<b>Operation and validation of the presented scanning lever AFM</b>	<b>78</b>
6.1	Realization and implementation of additional components . . . . .	78
6.1.1	Trajectories for raster scanning . . . . .	78
6.1.2	Generating arbitrary scan trajectories . . . . .	81
6.1.3	Driving the stack piezos . . . . .	84
6.1.4	z-Feedback controller . . . . .	85
6.1.5	Data acquisition . . . . .	85
6.1.6	The graphical user interface . . . . .	85
6.2	System dynamics . . . . .	87
6.2.1	Frequency domain . . . . .	87
6.2.2	Time domain . . . . .	90
6.3	Imaging . . . . .	94
6.4	Conclusion . . . . .	101
<b>7</b>	<b>Conclusions</b>	<b>102</b>

*Contents*

**8 Outlook**

**105**

---

## List of Figures

---

1.1	The atomic force microscope (AFM).	2
2.1	Scanning principles	5
2.2	Force curve	7
2.3	Scanning electron image of a cantilever.	9
2.4	STM based deflection readout.	11
2.5	Deflection readout based on capacitive sensing.	11
2.6	Piezoelectric tube scanner	15
2.7	High speed scanner	16
2.8	Comparison of high speed scanners	17
3.1	Schematic of a common deflection readout circuit design.	21
3.2	Setup to investigate the common mode noise density.	23
3.3	Transimpedance amplifier (TIA) configurations	24
3.4	Transimpedance amplifier (TIA) with source capacitance $C_s$ .	25
3.5	Open loop transfer function.	26
3.6	Geometry of the QPD.	27
3.7	Measurement of the QPD output with respect to spot size and position.	29
3.8	Simulated output voltage $U_{vert}$ for a spot diameter of 3mm.	30
3.9	Measured output voltage $U_{vert}$ for a spot diameter of 3mm.	30
3.10	Deviation of measured (Fig. 3.9) and calculated (Fig. 3.8) output.	31
3.11	Simulated output voltage $U_{vert}$ for a spot diameter of $30\mu\text{m}$ .	32
3.12	Measured output voltage $U_{vert}$ for a spot diameter of $30\mu\text{m}$ .	32
3.13	Deviation of measured (Fig. 3.12) and calculated (Fig. 3.11) output.	33
3.14	Directional sensitivity for a spot diameter of 30mm.	34
3.15	Directional Sensitivity of QPD for a spot diameter of $30\mu\text{m}$ .	34
3.16	Overlay of vertical and horizontal sensitivity.	35
3.17	Maximum sensitivity with respect to the normalized spot size.	35
3.18	Measurement of transfer function from the laser to the TIA.	39
3.19	Frequency response of the photodiode and the TIA.	40
3.20	Voltage noise density	41

## List of Figures

4.1	Crosstalk between the z-actuation and the deflection. . . . .	44
4.2	Additional lens in the optical path. . . . .	45
4.3	Test setup to evaluate crosstalk reduction. . . . .	46
4.4	Position and tilt of laser source. . . . .	47
4.5	Deflection components at an exemplarily position of the focusing lens. . . . .	48
4.6	Relative error of the curve fitting result shown in Fig. 4.5. . . . .	49
4.7	Deflection components with focusing lens close to the optimal position. . . . .	49
4.8	Crosstalk and sensitivity with respect to the focusing lens position. . . . .	50
4.9	Spot size dependent output. . . . .	51
4.10	Additional lens in optical path . . . . .	53
4.11	Additional lens in optical path . . . . .	54
5.1	Optical beam deflection method for scanning lever AFMs . . . . .	58
5.2	Move along the optical beam with a multidimensional scan stage. . . . .	59
5.3	Scanning lever AFM Laserpath based on folding. . . . .	61
5.4	Simulated cantilever deflection. . . . .	63
5.5	Simulated deflection on QPD. . . . .	64
5.6	Simulated x-actuation. . . . .	65
5.7	Simulated y-actuation. . . . .	66
5.8	Simulated crosstalk for a deflected cantilever. . . . .	68
5.9	z-Scanner . . . . .	70
5.10	x-Scanner . . . . .	72
5.11	nPoint NPXY100-100 stage . . . . .	74
5.12	Laser alignment . . . . .	74
5.13	Serial Scanner . . . . .	75
5.14	Scanning Lever AFM . . . . .	77
6.1	Input shaping . . . . .	80
6.2	Scan size . . . . .	83
6.3	Minimum jerk trajectory. . . . .	84
6.4	GUI . . . . .	86
6.5	Frequency response of x-Scanner . . . . .	88
6.6	Frequency response of y-Scanner . . . . .	89
6.7	Frequency response of z-Scanner . . . . .	90
6.8	Capped triangle scan at 100 Hz. . . . .	91
6.9	Capped triangle scan at 300 Hz. . . . .	92
6.10	Capped triangle scan at 600 Hz. . . . .	93
6.11	Optimization based triangular scan at 100 Hz. . . . .	94
6.12	Optimization based triangular scan at 300 Hz. . . . .	95
6.13	Optimization based triangular scan at 600 Hz. . . . .	95
6.14	Capped triangle triangle scan at 10 Hz. . . . .	96
6.15	Capped triangle triangle scan at 100 Hz. . . . .	97
6.16	Capped triangle triangle scan at 625 Hz. . . . .	98
6.17	Optimization based triangle scan at 100 Hz. . . . .	99
6.18	Optimization based triangle scan at 625 Hz. . . . .	100

---

## List of Tables

---

2.1	Examples of commercially available cantilevers. . . . .	9
-----	---	---

# CHAPTER 1

---

## Introduction

---

Is imaging of atoms possible? Ernst Abbe found in 1873 that the resolution defined by the distance  $d$  of distinguishable points is diffraction limited for the optical microscope to approximately one half a wavelength  $\lambda$  [1]. For example using visible light with a wavelength in the order of 500 nm leads to a resolution of 250 nm not sufficient to image molecules or atoms in the range of nanometer and sub-nanometer.

To overcome the resolution limit of the optical microscope, G. Binnig and H. Rohrer invented the Scanning Tunneling Microscope (STM) [2] in 1982 at IBM Zurich what allows topography imaging of conductive surfaces on the atomic scale. The Royal Swedish Academy of Science awarded one half of the 1986 Nobel Prize in Physics to G. Binnig and H. Rohrer for their design of the STM [3].

To allow imaging of non-conductive surfaces too, in 1986 the Atomic Force Microscope (AFM) was invented by G. Binnig, C. F. Quate, and H. Rohrer [4]. The working principle of an AFM (Fig. 1.1) is to probe the surface of a sample by a sharp tip mounted on the free end of a micro cantilever while raster scanning the sample and tip relatively to each other. The interaction between the tip with a radius of only a few nanometers and the sample comprises several attractive and repulsive forces such as Van der Waals forces and Pauli repulsion [5]. The deflection of the cantilever typically is measured by an optical lever system [6][7], in which a laser beam is reflected off the back of the cantilever onto a quadrant photodetector (QPD), which consists of four photodiodes that are separated by a small gap. As the distance between the cantilever and the QPD is much longer than the length of the cantilever, the small angular deflection of the cantilever is geometrically amplified [5].

In most AFM applications the highly nonlinear tip-sample interaction force is held constant via feedback operation [8] in order to avoid damage to the tip and the sample and to obtain reliable measurement data. The output of the feedback controller corresponds to the displacement required to maintain a constant imaging force, thereby converting the force measurement into a displacement measurement with well known characteristics. This allows to measure the sample topography by recording the control signal of the vertical (Z) feedback loop as a function of the lateral (X and Y) scanning

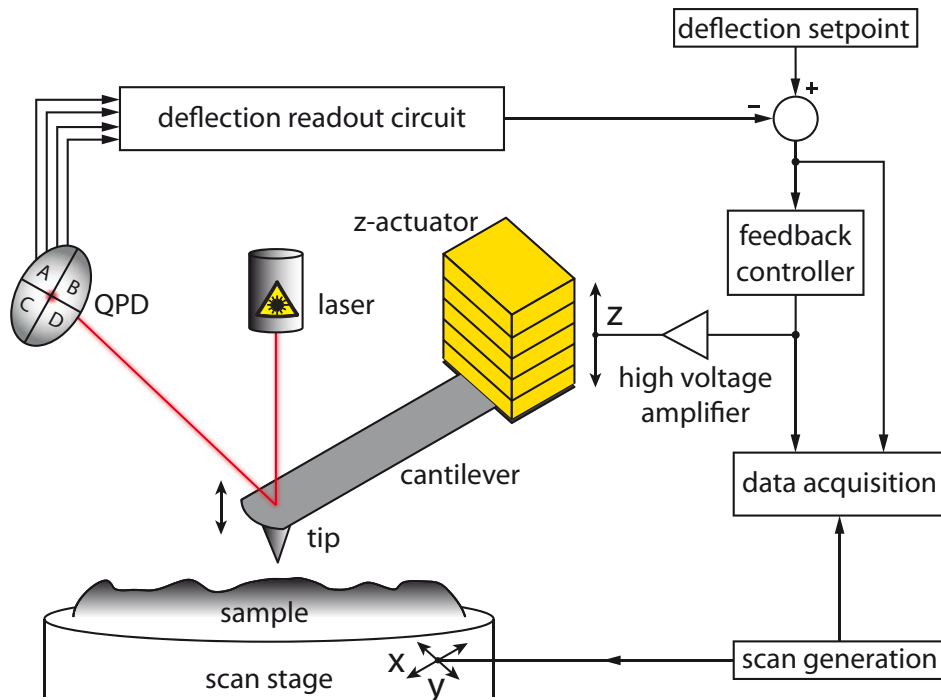


Figure 1.1: The atomic force microscope (AFM) [4] with the sharp tip at the free end of the cantilever. The deflection is measured by the optical beam deflection method and compensated by the feedback controller driving the z-actuator via an high voltage amplifier. While scanning the sample, the residual deflection and the output signal of the controller, containing the height information, is recorded by the data acquisition system.

position of the tip (Fig. 1.1).

The AFM is widely used for imaging [9] and metrology [10] at the nanometer scale. Examples are bio-nanotechnology, nano-metrology, semiconductor manufacturing, chemical science, and material science [11]. Although imaging frame by frame leads to an image sequence, the slow line scan rate of standard AFMs limits the observation of real time processes. For example, imaging at  $1024 \times 1024$  pixel with a standard AFM takes several minutes per frame and therefore real time observation as with a conventional optical microscope is impossible. Furthermore the application in industry is limited by the low throughput. Recent research activities have shown that imaging at video rate is possible with so called scanning sample AFMs [12]. In scanning sample AFMs the scanning motion is generated by scanning the sample as shown in Fig. 1.1, limiting the application to small and lightweight samples. In contrast to scanning sample AFMs, the scanning lever AFM where the cantilever is scanned across the surface gives maximum flexibility about the sample size and mass [11]. Scanning on large samples in industry or scanning biological samples in petri dishes is best done by a scanning lever system. To keep the high throughput in industrial processes and gain the ability of real time observation at the nanometer scale high speed scanning lever AFMs are necessary.

## 1.1 Scope of the thesis

This theses focuses on the design and integration of the optical path into a high speed scanning lever AFM that enables imaging at a line scan rate of several 100 lines/s. Therefore key components such as the deflection readout or scan stage are analyzed concerning there bandwidth limitations. Additionally the crosstalk between the moving lever and the deflection readout is considered. The revised components are composed to proof the feasibility of high speed imaging of with a scanning lever AFM.

## 1.2 Outline

In Chapter 2 the state of the art is discussed and still open research questions are addressed. In Chapter 3 the design of a low noise high speed optical deflection readout is presented. In Chapter 4 the crosstalk between a compensating z-movement of the cantilever and the deflection readout is analyzed as well as a novel method to compensate for the crosstalk is presented. While Chapter 5 shows the design of a scanning lever AFM, the operation and imaging is shown in Chapter 6. All the research questions from Chapter 2 are revisited in Chapter 7 while Chapter 8 gives an outlook on future high speed scanning lever development possibilities.

Since the invention of the AFM in 1986, several design principles and a lot of different modes to operate the AFM have been introduced. The different scanning principles with respect to flexibility and scan speed are discussed in Sec. 2.1. The most basic and common ones widely used in AFM imaging are discussed in Sec. 2.2. With the focus on high speed scanning the single components of a common AFM as shown in Fig. 1.1 are discussed in Sec. 2.3. Missing knowledge for the design and integration of the optical path into a high speed scanning lever AFM that enables imaging at a line scan rate of several 100 lines/s is addressed in Sec. 2.4.

## 2.1 Scanning principles

There are different possibilities to scan the sample on the one hand (x/y-movement) and to compensate the deflection of the cantilever on the other hand (z-movement).

### 2.1.1 Scanning sample

For the scanning sample system as shown in Fig. 2.1a, the x-, y-, and z-movement is done by actuating the sample itself. For example using a piezoelectric tube scanner as shown in Fig. 2.6b the sample is moved in x-, y-, and z-direction while the cantilever is fixed. The main advantage of this configuration is the static cantilever holder to avoid crosstalk between the actuation and the deflection readout. A major drawback of moving the sample in x-, y-, z-direction is the limited sample size and sample mass. Especially for high speed scanning a high sample mass may limit the maximum possible scan speed by reducing the first dominant mechanical resonance of the scanner. Considering the actuator with an intrinsic stiffness  $k$  and the moving mass  $m$  as a mass spring system, the angular resonance frequency  $\omega_0 = \sqrt{k/m}$  [13]. The varying sample mass influences the system dynamics and makes a robust control design difficult.

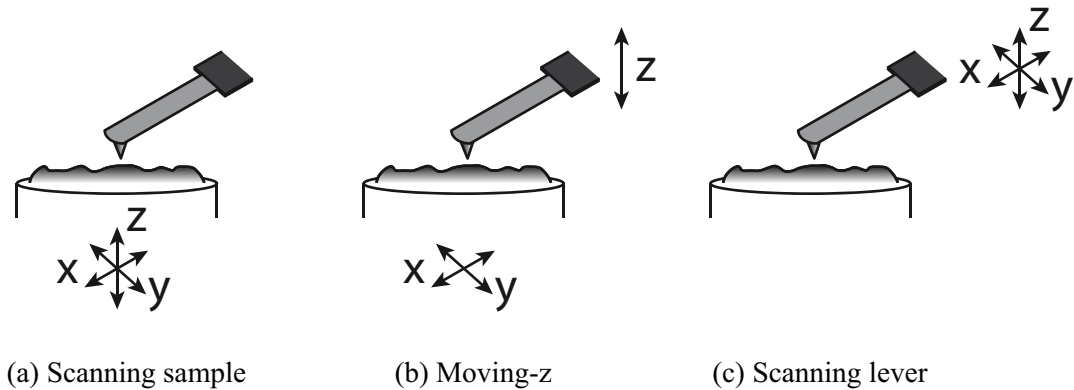


Figure 2.1: In a scanning sample system (a), the cantilever is fixed while the x/y raster scan and the compensating z-movement is done by actuating the sample. In a moving-z system (b), the compensating z-movement is done by actuating the cantilever, while the x/y raster scan is done by actuating the sample. In a scanning lever system (c), the sample is fixed while the x/y raster scan and the compensating z-movement is done by actuating the cantilever.

### 2.1.2 Moving-z

As the z-feedback loop including the z-actuator is one possible limiting factor for high speed imaging the cantilever instead of the sample can be moved to compensate for the cantilever deflection as shown in Fig. 2.1b. The configuration of this moving-z AFMs leads to almost constant system dynamics of the z-actuator as the mass variation of different cantilevers is small compared to the effective mass of the actuator including the cantilever holder. Designing the controller for a system with almost constant system dynamics is much easier and can be done with less margins to gain additional system performance. It is not analyzed so far if the vertical displacement of the cantilever influence the deflection measurement and to which extent crosstalk has to be considered?

### 2.1.3 Scanning lever

To get rid of sample size and sample mass limitations the scanning lever system as shown in Fig. 2.1c actuates the cantilever in x-, y-, and z-direction. Although the sample is static, care has to be taken about the deflection readout. For example using the optical beam deflection method the whole optical path is influenced by moving the cantilever. The laser spot has to track the moving cantilever as well as the crosstalk between the moving cantilever and the photodetector has to be considered. The straight forward approach to keep the relative position between moving cantilever and all components of the optical path constant, is to scan all components including the alignment mechanism [14]. At least for quasi static positioning the deflection readout is not affected by the x/y-actuation. When increasing the scan speed the structural dynamics of the interconnected parts have to be considered as the fast scanning motion may ex-

cite mechanical resonances and the whole structure may be deformed due to the inertial forces. The major drawback of scanning all the components is the high total moving mass. Scanning all components only a compact lightweight design in combination with a stiff flexure based x/y-actuation results in a high first dominant resonance frequency of about 10 kHz for the design presented in [14].

To reduce the moved mass an optical assembly (e.g. lens or mirror) that guides the laser on the cantilever can be scanned with the piezoelectric tube scanner used to scan the cantilever itself [15]. A special geometrical arrangement incorporating the bending of the tube avoids crosstalk between the scanning motion and the deflection readout. Although this system allows the integration of the optical beam deflection method in a scanning lever system, it is based on a piezoelectric tube scanner. The open question is, if the OBD method can be applied to flexure-based (in plane movement) scanning lever AFMs without moving the laser source, the detector, and the alignment mechanisms. If that is possible, can the flexure-based scanning lever AFM with the OBD be used for high speed scanning? Therefore, the **first and second research question** is formulated as follows:

Can the optical beam deflection method be applied to flexure-based (in plane movement) scanning lever AFMs without the need to move the laser source, the detector, and the alignment mechanisms?

Can the flexure-based scanning lever AFM with the OBD be used for high speed scanning?

## 2.2 Modes of operation

Basically scanning the sample can be done with and without feedback [16]. Scanning the sample with a constant height of the cantilever with respect to the sample mount, the cantilever is deflected by forces due to the varying distance between the tip and the sample. The force between the cantilever tip and the sample surface with respect to their distance is shown in Fig. 2.2. As a drawback the constant height mode leads to force variations according to the varying topography, where high forces can damage the tip or sample, especially at higher scan rates [11]. Although the recorded deflection signal is proportional to the force between the tip and the sample, the relation between force and distance is highly nonlinear as shown Fig. 2.2. Therefore a reliable and accurate surface reconstruction is hardly possible.

In constant force mode the measured deflection is compensated by displacing the cantilever. The deflection is measured and compared to a certain setpoint by the feedback controller. The output of the feedback controller drives an actuator displacing the cantilever to keep the deflection constant. With the known characteristic of the actuator including its amplifier, the force measurement is converted to a displacement measurement. Therefore the topography is imaged by recording the output signal of the feedback controller. As for accurate measurements the vertical actuator has to follow the topography, the positioning bandwidth of the feedback loop is a potential limitation for high speed scanning [12].

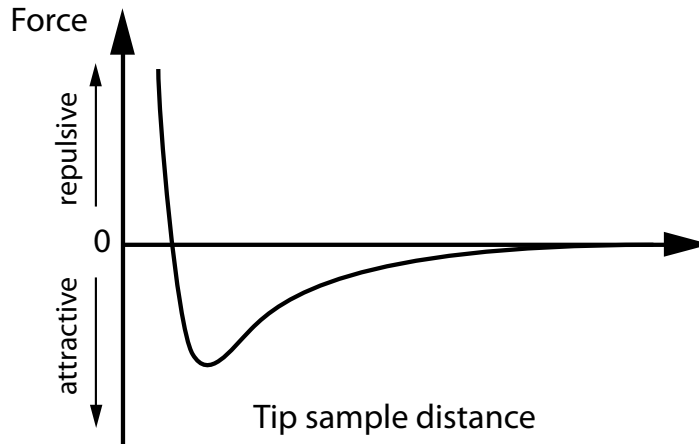


Figure 2.2: Force between the cantilever tip and the sample with respect to the tip sample distance [17].

Operating the AFM in feedback can be categorized in two basic measurement modes: The static mode where the tip should be in permanent contact with the sample surface, and the dynamic mode where the cantilever is oscillated at or close to its natural resonance frequency [17]. In static mode also known as contact mode, the feedback operation is based directly on the measured deflection of the cantilever, whereas in dynamic mode the two sub-cases amplitude modulation (AM) and frequency modulation (FM) must be considered [18]. In the so called tapping mode based on AM, the cantilever is excited slightly off its resonance. A change in interaction force leads to a change in the oscillation amplitude, which can be used as sensor signal, and the feedback operation tracks a constant oscillation amplitude [19]. In the FM mode, the cantilever is excited at its resonance. Changes in the interaction detune this resonance, where the frequency deviation is used as sensor signal to drive the feedback loop [20]. Due to the necessary AM- or FM-demodulation in dynamic mode an additional delay is introduced into the feedback loop. The additional delay reduces the phase margin and therefore limits the maximum possible positioning bandwidth in comparison to static mode imaging. Therefore, for high speed imaging the static mode is preferable as the deflection of the cantilever is directly measured without an additional delay due to the demodulation.

Although the feedback signal in tapping mode is usually gained from the amplitude, the interaction between the cantilever and the sample is highly non-linear. The complex interaction of the cantilever with the surface leads, beside a change in amplitude and phase, to the excitation of higher harmonic movements of the cantilever [21][22]. Recording the higher harmonics allows reliable topography imaging as well as recovering additional mechanical surface properties of the sample [23]. Recording higher eigenmodes of the vibrating cantilever in tapping mode can be more sensitive to certain inhomogeneities and surface contamination [24] as well as more sensitive to surface properties like the stiffness of the sample [25] in comparison to standard tapping mode. Therefore besides high speed imaging, a high bandwidth of the deflection readout is an additional asset for extracting additional mechanical surface sample

properties.

## 2.3 Components

A common AFM as shown in Fig. 1.1 consists of the following main components:

- Sample
- Cantilever
- Deflection Readout
- z-Scanner
- z-Feedback Controller
- x/y-Scan Stage
- Data Acquisition
- User Interface

These single components are explained and evaluated in detail in the following sections.

### 2.3.1 Sample

The sample is the piece of matter of which the surface is imaged by the AFM. Samples can be as different as biological samples, minerals, coatings, and semiconductors with a wide variation in the topography features as well as on the mechanical properties like stiffness or friction.

### 2.3.2 Cantilever

The cantilever as key element of the AFM is a small micro machined lever with a sharp tip at its free end. It acts as a force sensor to probe the tip-sample interaction. The interaction force between the cantilever tip and the sample surface with respect to their distance is shown in Fig. 2.2. It comprises several attractive and repulsive forces like Van der Waals forces and the Pauli repulsion, by translating the force to a deflection [5]. Based on the application and measurement mode different properties like the stiffness or resonance frequency of the cantilever are of interest. Furthermore for some special type of measurements other properties such as electric [26] or magnetic [27] ones can be of interest.

The length of common cantilevers ranges from several  $10\ \mu\text{m}$  to several  $100\ \mu\text{m}$  while the width of the usually rectangular or triangular shaped cantilevers is in the order of several  $10\ \mu\text{m}$ . The radius of the sharp tip is in the order of a few nanometer. The stiffness of the cantilevers ranges from around  $0.01\ \text{N/m}$  to several  $100\ \text{N/m}$  while the resonance frequency range starts from around  $1\ \text{kHz}$  and goes up to more than  $1\ \text{MHz}$ . To show the wide variation some exemplary cantilevers are listed in Tab. 2.1.

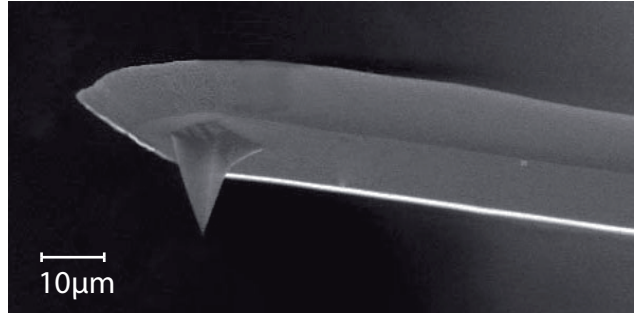


Figure 2.3: Scanning electron image of a cantilever with the sharp tip at its free end.

Name	Resonance Frq.	Stiffness	Length	Width	Shape
MSNL-10 (C)	7 kHz	0.01 N/m	310 $\mu\text{m}$	20 $\mu\text{m}$	Triangular
FastScan A	1400 kHz	18 N/m	27 $\mu\text{m}$	32 $\mu\text{m}$	Triangular
MPP-13100-W	525 kHz	200 N/m	125 $\mu\text{m}$	40 $\mu\text{m}$	Rectangular

Table 2.1: Examples of commercially available cantilevers (Bruker AFM Probes, CA, USA).

### Cantilever noise

Although the bandwidth of the deflection readout is an important property for high speed imaging as well as imaging higher harmonics and modes, the imaging resolution is mainly determined by the total system noise. The total system noise is a combination of several noise sources like the laser, QPD, and amplifier noise, external and internal mechanical vibrations, the actuator noise and the cantilever noise. The effect of the cantilever noise on the optical lever system depends on the temperature, the spring constant, and the support of the end of the cantilever by the probe [28]. Therefore the cantilever noise can be seen as the lower limit of the system noise limiting the maximum achievable imaging resolution.

For the unsupported case where the tip is not in contact with the sample the optical beam deflection method measures a mean deflection noise [28]

$$\sqrt{z_{free}^2} = \sqrt{\frac{4k_B T}{3k}}, \quad (2.1)$$

with the Boltzmann constant  $k_B$ , the absolute temperature  $T$  and the cantilever stiffness  $k$ . For the supported case where tip is in contact with a hard sample the mean deflection noise [28]

$$\sqrt{z_{supported}^2} = \sqrt{\frac{k_B T}{3k}}. \quad (2.2)$$

The support of the cantilever depends mainly on the measurement mode and the relation between the sample and cantilever stiffness. The real situation will be somewhere in between the supported and the unsupported case, depending on the measurement mode. With the supported case as ultimate limit, the deflection noise for a cantilever

with a stiffness of 1 N/m is 37 pm at an ambient temperature of 296 K.

### 2.3.3 Deflection readout

The cantilever acts as force sensor to probe the tip-sample interaction. The actual deflection of the cantilever, which is related to the tip-sample interaction force, is measured by the deflection readout mechanism. Besides the optical beam deflection method shown in Fig. 1.1, several other methods can be used to measure the small deflection of the cantilever.

Especially for high speed imaging certain properties like the bandwidth, phase and delay of the deflection readout are of special interest. One limitation for the maximum imaging speed is the maximum vertical tracking speed [16]. The maximum vertical tracking speed is determined by the tracking bandwidth of the vertical feedback loop. Therefore the deflection readout mechanism included in the feedback loop is a determining component for the achievable tracking speed. Although it is possible to compensate for a phase error in imaging, the control bandwidth of the z-feedback controller is limited by the reduced phase margin due to the phase lag of the deflection readout.

As the measurement noise is a determining factor for the vertical imaging resolution, a trade off between the measurement noise of the deflection readout and the achievable bandwidth has to be considered. For contact mode imaging the noise can be reduced by limiting the measurement bandwidth while in tapping mode low frequency noise can be filtered out.

Considering tapping mode the resonance frequency of the cantilever is the determining factor of the required deflection readout bandwidth. Furthermore, recording higher harmonics or recording higher eigenmodes of the cantilever, requests an even higher bandwidth. For example the second eigenmode of the high frequency cantilever prototype USNMCB-3.5MHz (Nanosensors, Neuchatel, Switzerland) is at 21.4 MHz [29].

In the following sections possible deflection readout mechanisms are evaluated.

#### Deflection readout based on STM

The method used in the first AFM [4] is the measurement of the tunneling current through a tunneling electrode in close proximity to the conductive backside of a cantilever as shown in Fig. 2.4. In contrast to the Scanning Tunneling Microscope (STM) the AFM allows imaging of non-conductive surfaces. Although it is possible to achieve atomic resolution [30], this method has several drawbacks. The tunneling current is highly sensitive to contamination and even under ultra high vacuum the tip scans the atomic structure of the levers backside which is superimposed to the sample topography [5]. Furthermore the force between the tunneling electrode and the cantilever is superimposed to the force between the tip and the sample. Due to the close proximity of the tunneling electrode to the cantilever the risk of damaging the tunneling electrode when crashing the cantilever is high.

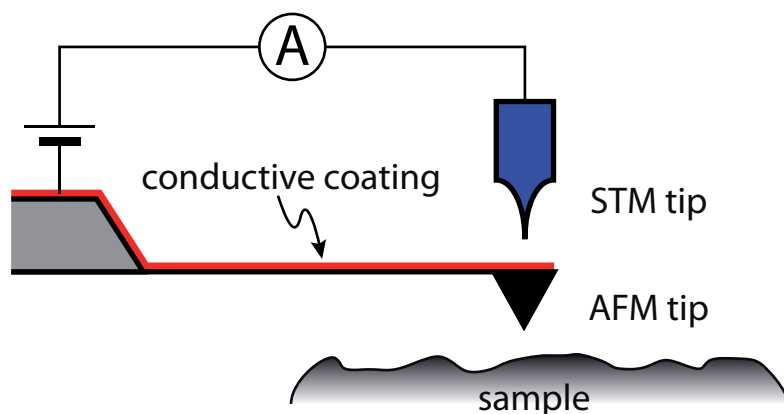


Figure 2.4: STM based deflection readout.

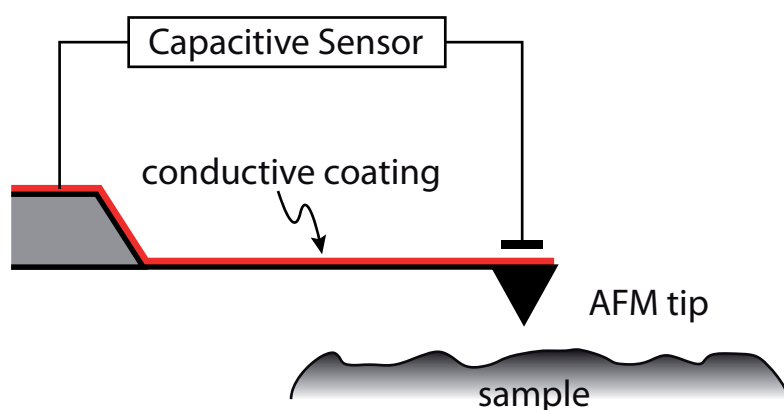


Figure 2.5: Deflection readout based on capacitive sensing.

### Deflection readout based on capacitive sensing

Another method for the deflection readout is the use of capacitive sensing as shown in Fig. 2.5. The capacitance is formed by the sensing electrode and the conductive coating of the cantilever. Neglecting the stray capacitance, the small change of the capacitance is inverse proportional to the deflection. Due to the small area of the cantilever the sensing electrode must be in close proximity to the cantilever leading to the risk of damaging the sensing electrode when crashing the cantilever. The first application of capacitive sensing of the cantilever deflection was shown by imaging the magnetic storage medium of a 3.5 in floppy disk [31].

### Deflection readout based on laser interferometry

The risk of damaging the readout mechanism can be reduced by using optical long range displacement measurement techniques like laser interferometry. Atomic scale resolution with a deflection readout based on homodyne laser interferometry was shown by imaging atomic-scale features on the basal plane of a graphite surface [32].

All aforementioned deflection readout mechanisms are sensitive to thermal drift

and mechanical vibrations of the measurement path [5]. To reduce the sensitivity to drift, heterodyne laser interferometry can be used with tapping mode, leading to an output signal with the amplitude proportional to the deflection amplitude of the cantilever, but independent of the average distance between the readout mechanism and the cantilever [33].

A new design freedom is gained by the possibility to place the laser interferometry based readout mechanism at a certain distance from the cantilever. Additionally a fiber coupled interferometric measurement simplifies the design of the optical path [34]. Using the optical and mechanical properties of the fiber, a monolithic fiber-top sensor can be used to measure the deflection. Directly cutting a lever out of the end of a fiber allows for manufacturing a monolithic fiber-top sensor [35]. Although production costs of fiber-top sensors can be reduced [36] it is not possible to use the high variety of commercial available cantilevers. The applicability of fiber-top sensors in high speed scanning AFMs is demonstrated by [37].

### **Deflection readout by optical beam deflection method**

Common to all aforementioned deflection readout mechanisms is the direct measurement of the deflection perpendicular to the sample surface. Therefore the resolution of the sensor must be at least as high as the desired vertical resolution.

The most common deflection measurement method is the optical beam deflection method [6][7] in which a laser beam is reflected off the back of the cantilever onto a quadrant photodetector (QPD), which consists of four photodiodes separated by a small gap (Fig. 1.1). As the distance between the cantilever and the QPD is much longer than the length of the cantilever, the small angular deflection of the cantilever is geometrically amplified [5]. Therefore, in contrast to the aforementioned deflection readout mechanisms, the resolution of the displacement measurement on the QPD can be much lower than the requested vertical resolution.

Using integrated circuits for the electronic design of the deflection readout circuit a noise density as low as  $17 \text{ fm}/\sqrt{\text{Hz}}$  is possible with the optical beam deflection method [38]. To reduce the optical interference noise the coherence length is reduced by modulating the laser source with a high frequency signal between 300 MHz and 500 MHz [39][40]. It has to be mentioned that the given noise density of  $17 \text{ fm}/\sqrt{\text{Hz}}$  denotes the noise floor at 260 kHz neglecting  $1/f$ -noise. Although the  $1/f$ -noise can be filtered for tapping mode imaging, it is a determining factor of the achievable imaging resolution in contact mode. The major limitation of the presented system for high speed scanning is the rather low bandwidth of 1.5 MHz. More recent work on the deflection readout shows, that designing the electronics at the transistor level further reduces the noise density to  $4.5 \text{ fm}/\sqrt{\text{Hz}}$  while increasing the bandwidth to 20 MHz [29]. Again the  $1/f$ -noise is neglected as the given noise density of  $4.5 \text{ fm}/\sqrt{\text{Hz}}$  denotes the noise floor at 1 MHz.

Although the optical beam deflection method is the most widely used deflection readout mechanism, their detection bandwidth hardly covers the second eigenmode of high frequency cantilevers particularly suitable for high speed scanning [12]. Therefore, the **third research question** is formulated as follows:

What are the bandwidth and resolution limiting factors for the optical beam

deflection method used in AFMs?

### 2.3.4 z-Actuator

Although a silicon cantilever can be deflected by ten's of micrometer without damaging, the relation between the distance from the tip to the sample and the resulting interaction force is highly nonlinear. Therefore in most AFM applications a change in the interaction force between the cantilever and the sample is compensated by the z-actuator displacing the cantilever, the sample or both perpendicular to the scan plane. The output of a feedback controller driving the z-actuator corresponds to the displacement required to maintain a constant imaging force, thereby converting the force measurement into a displacement measurement with well known characteristics. This allows to measure the sample topography by recording the control signal of the vertical feedback loop.

Depending on the feedback controller the dynamics of the z-actuator is the determining factor for the achievable feedback bandwidth [41]. The achievable tracking bandwidth is limited by weakly damped mechanical resonances. High mechanical resonances of the z-actuator are achieved by a stiff and lightweight design. A rigid design of the z-actuator in combination with small piezo elements results in a high first resonance frequencies [42][43][44] and therefore in a high control bandwidth. Mechanical oscillations can be reduced by a balanced design counteracting the actuation forces [42][45][46]. To overcome the tradeoff between a high actuation range and a high first mechanical resonance frequency, long range and short range actuators are combined in dual actuated AFMs [47][48][49].

If the compensating movement is done by actuating the sample the deflection readout mechanism is not affected. However, if the cantilever is actuated like in Fig. 2.1b&c the position of the cantilever with respect to the deflection readout mechanism changes. Depending on the readout mechanism the compensating cantilever movement may affect the deflection readout mechanism. It is not analyzed so far if the vertical displacement of the cantilever influences the deflection measurement and to which extent crosstalk between the compensating cantilever movement and the deflection readout has to be considered. Therefore, the **fourth research question** is formulated as follows:

Does the vertical displacement of the cantilever influence the deflection measurement and to which extent crosstalk has to be considered?

### 2.3.5 z-Feedback controller

As mentioned in Sec. 2.3.4 in most AFM applications a change in the interaction force between the tip and the sample is compensated by the z-actuator displacing the cantilever, the sample or both. The difference between the measured deflection in contact mode or amplitude in tapping mode and a certain setpoint represents the error signal used as the input to the z-feedback controller. The common z-feedback controller in AFMs is a proportional-integral (PI) controller with an optional low-pass filter to suppress the amplification high frequency noise. Additional filters like notch filters can help to suppress the excitation of mechanical resonances of the scanner to increase the

bandwidth. The output of the z-feedback controller is used as input to the high voltage amplifier driving the z-Actuator.

### 2.3.6 x/y-Scan stage

To get an image of the sample, the tip and the sample are scanned with respect to each other. In most AFMs raster scanning is performed by using a triangular signal for the vertical and horizontal actuation in order to achieve a constant relative tip-sample velocity. For imaging frames with  $m$  lines at a line scan rate of  $f_{line}$  the actuation frequency of the fast scan axis  $f_{fast} = f_{line}$  while the frequency of the slow scan axis  $f_{slow} = f_{line}/(2m)$  leads to a frame rate of  $f_{frame} = f_{line}/m$ .

For scanning the sample or the tip in x- and y-direction a two dimensional actuator is needed. A multidimensional actuator can either be based on a serial or a parallel configuration or a combination of both [50]. In the serial configuration single actuators are nested in a way that the stator of one actuator is mounted on the moving part of a second actuator with the actuation direction perpendicular to each other. In the parallel configuration the actuator is built in a way that single actuators, sharing a common stator, are acting on a common moving part.

A common example for a parallel design is the widely used piezoelectric tube actuator [8] as shown in Fig. 2.6a. A tube of piezoelectric material is contacted by four outer electrodes and a counter electrode on the inner side. The tube is bent by applying an opposing voltage to the opposite electrodes of the tube elongating on one side while shortening the other side. An additional actuation in z-direction is possible by adding a different structure of the electrodes above the x/y-electrodes, as shown in Fig. 2.6b. Although the x-, y-, and z-actuators are on the same tube, the x/y-actuation is based on a parallel design while the z-actuator is nested. Therefore the total x/y/z-actuator is a combination of the serial and parallel design.

When scanning at a high line scan rate the higher harmonics of the triangular scan signal can excite mechanical resonances of the scan stage which impairs the tracking accuracy of the scanning motion, modulates the relative tip-sample velocity, and results in distortions of the recorded images [51][52]. Unfortunately the distortions are not always limited to the fast scan axis as resonances of other axis can be excited due to the mechanical coupling [53].

In new mechatronic designs [12][42][43][44][54] the first mechanical resonance of the AFM-scanner is shifted towards higher frequencies by making the scanner more rigid and reducing the moved masses. However, increasing the resonance frequency by a stiff design often limits the positioning range. While AFM imaging with a piezoelectric tube scanner with a range of  $125 \times 125 \mu\text{m}^2$  allows a line scan rate of up to 122 Hz [52], the flexure based high speed scanner [44] shown in Fig. 2.7 has a reduced range of  $13 \times 13 \mu\text{m}^2$  but allows imaging at a line rate of more than 8000 Hz [12]. The first dominant resonance frequency of the flexure based high speed scanner is at 22 kHz in comparison to the 0.7 kHz of the tube scanner.

Both, serial and parallel kinematic scanners are developed for high speed scanning. The trade off between the resonance frequency and the actuation range can be seen in Fig. 2.8 [11] where SK denotes a serial kinematic design, PK a parallel kinematic design and SA denotes single axis actuators. The main advantages of the parallel kinematic

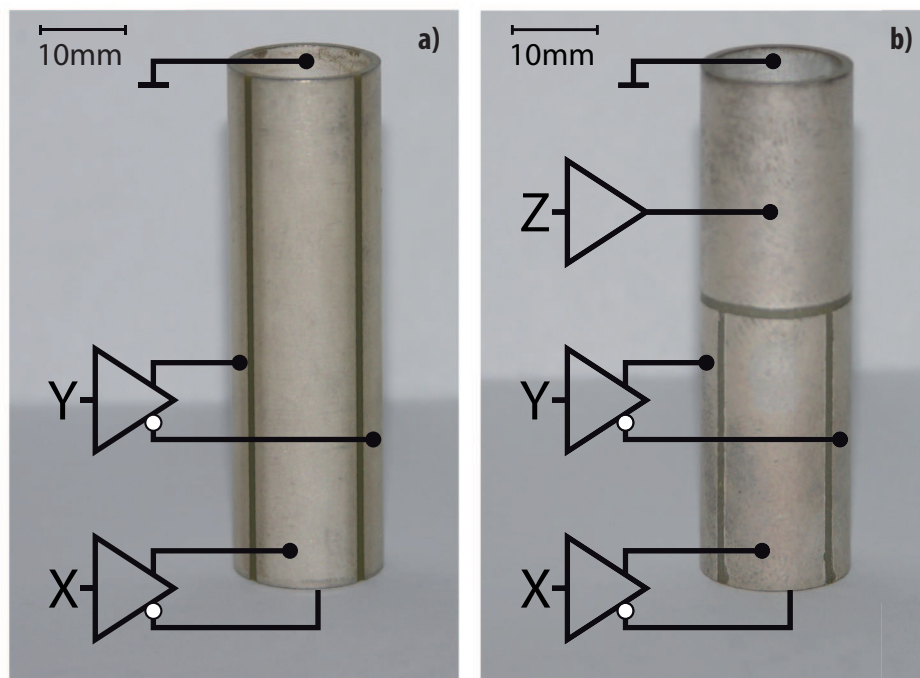


Figure 2.6: Piezoelectric tube scanner (a) for  $x$  and  $y$  scanning movement, and (b) with an additional  $z$ -Actuator.

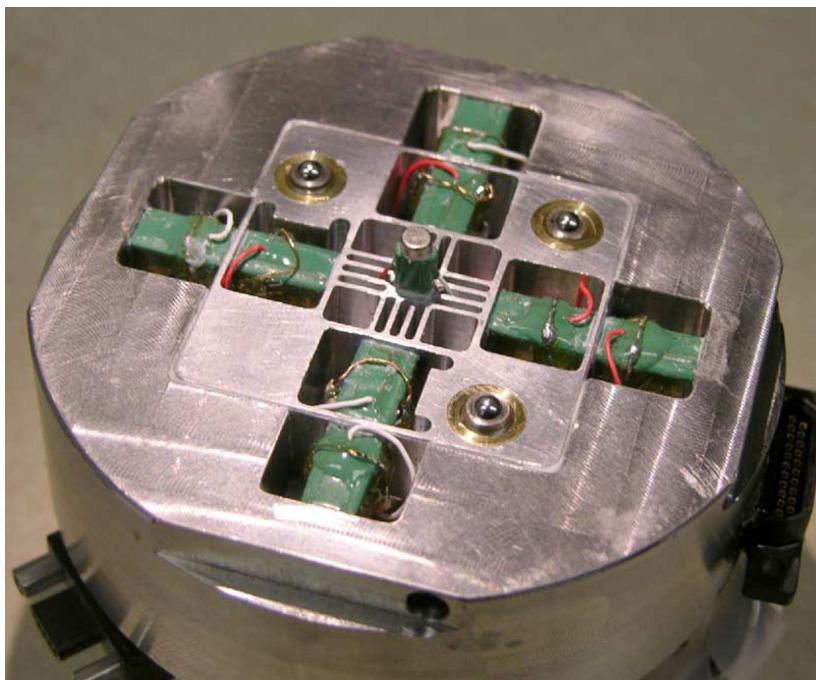


Figure 2.7: High speed scanner with a range of  $13\ \mu\text{m}$  and a first dominant resonance at 22 kHz [44]

design are the low moving mass, the compact design, and the possibility to scan in an arbitrary direction if both axis have the same mechanical bandwidth [50]. Anyway, in an AFM using a raster scan pattern there is a dedicated fast scan axis [50]. If image rotation is necessary a mechanism to rotate the scanner, the sample, or the scan head itself can be implemented although it is usually hard to change the center of rotation in such implementations.

In addition to the low mass but rigid mechanical design the control of the scanner is important for high speed scanning [48][55][56]. The fast control of the scanner can be done in open-loop (feedforward control) [51][52], in a closed-loop (feedback control) [57][58] or a combination of feedforward and feedback control called two-degrees of freedom control [59]. However, the applicability of feedback control depends on the design of the AFM system, i.e. whether position sensors are available to measure the X- and Y-position.

### 2.3.7 Data acquisition

As shown in Fig. 1.1, the data acquisition is done by recording signals like the output of the z-feedback controller (height information) and the deflection signal (remaining control error). Lines and frames are aligned by synchronizing them with the scan signal generators for the fast and slow scan axis. The minimum sampling rate is determined by the requested imaging resolution and line scan rate. Imaging with a resolution of  $n$  pixel per line at a line scan rate of  $f_{line}$  requests a sample rate of  $2 \cdot n \cdot f_{line}$  for recording trace and retrace. Using a  $N$ -bit analog to digital converter leads to a

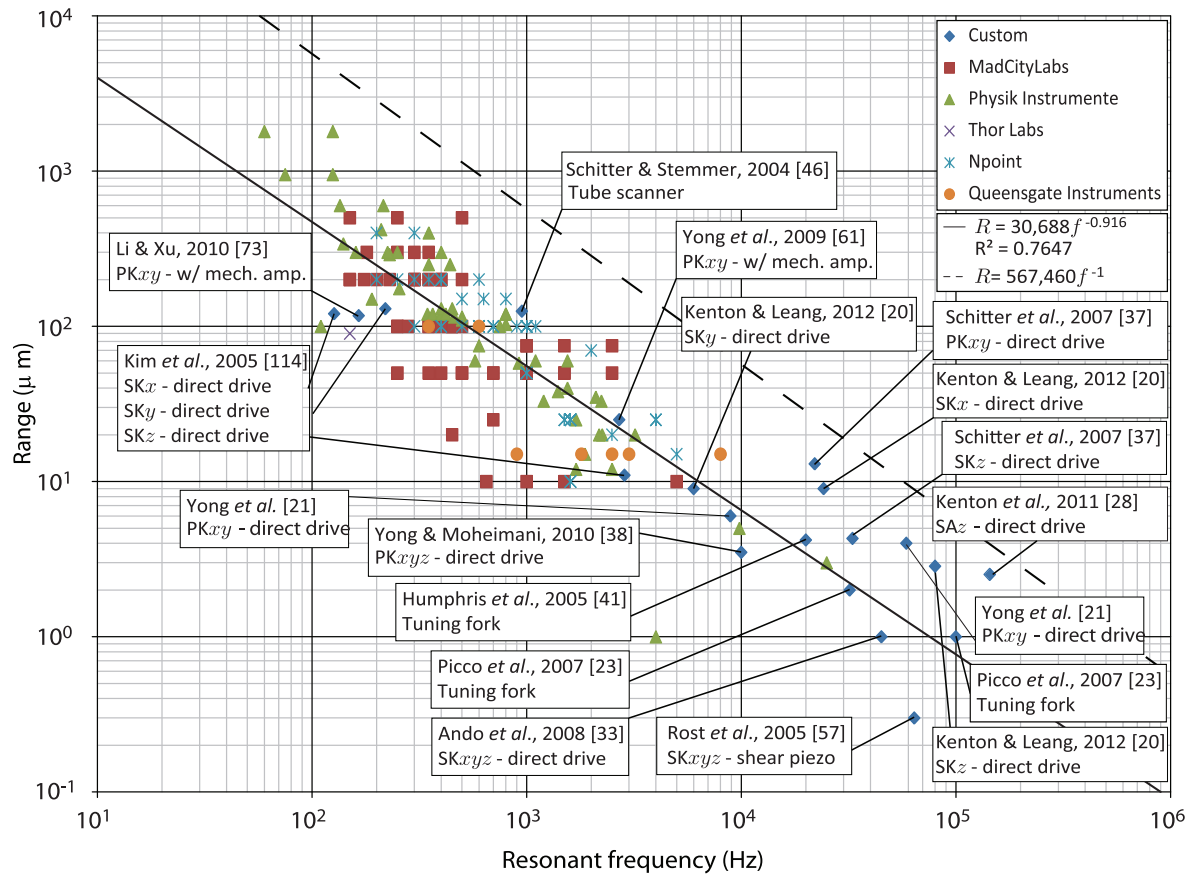


Figure 2.8: The comparison of high speed scanners developed for AFMs shows the trade off between the resonance frequency and the actuation range. SK denotes a serial kinematic design, PK a parallel kinematic design and SA denotes single axis actuators. Reprinted with permission from [11]. Copyright 2012, AIP Publishing LLC.

data rate of  $\frac{N}{4} \cdot n \cdot f_{line}$  Byte/s per channel. For example imaging with a resolution of  $1000 \times 1000$  pixel at a line scan rate of 1000 lines/s requests a sample rate of 2 MSa/s and leads to a data rate of 4 MB/s per channel.

### **2.3.8 User interface**

The user interface (UI) is used to operate and control the instrument by the user. On the one hand it allows setting parameters like the scan mode, scan size, scan range, and line scan rate as well as tuning the z-feedback controller and on the other hand it is used for visualizing the sampled data like trace and retrace as well as the acquired image. Modern UIs implement much more like data handling and image analysis.

## 2.4 Research questions

The research questions formulated in the former sections can be summarized as:

- What are the bandwidth and resolution limiting factors for the optical beam deflection method used in AFMs?  
(formulated in Sec. 2.3.3 and investigated in Chapter 3)
- Does the vertical displacement of the cantilever influence the deflection measurement and to which extent crosstalk has to be considered?  
(formulated in Sec. 2.3.4 and investigated in Chapter 4)
- Can the optical beam deflection method be applied to flexure-based (in plane movement) scanning lever AFMs without the need to move the laser source, the detector, and the alignment mechanisms?  
(formulated in Sec. 2.1.3 and investigated in Chapter 5)
- Can the flexure-based scanning lever AFM with the OBD be used for high speed scanning?  
(formulated in Sec. 2.1.3 and investigated in Chapter 6)

---

High bandwidth deflection readout <sup>1</sup>


---

To enable high speed high resolution imaging as well as higher mode and higher harmonics imaging, this chapter focuses on the bandwidth and resolution limiting factors of the optical beam deflection method used in AFMs. The sensitivity and noise of the deflection readout mechanism is a determining factor for the vertical imaging resolution. Therefore, in a first step the deflection readout circuit is analyzed in Sec. 3.1 with respect to bandwidth, gain, and noise, while in a second step the geometry and size of the QPD is analyzed with respect to the bandwidth, noise, and sensitivity. The third step combines the results of the former ones and shows the implementation of a high speed deflection readout in Sec. 3.3.

### 3.1 The deflection readout circuit

The QPD shown in Fig. 1.1, widely used as the position sensitive device for the optical beam deflection method in commercial AFMs [17], consists of four photodiodes with a sensitivity  $S_{QPD}$ , usually about 0.5 A/W, and converts the total radiant power  $\phi_{e,i}$  incident on the single photodiode  $i \in \{A, B, C, D\}$  to a small output current  $I_i$  in the order of 100  $\mu$ A [13]. The deflection readout circuit generates a position dependent signal using the photodiode output currents. The principle of a common deflection readout circuit design is shown in Fig. 3.1. It consists of four transimpedance amplifiers (TIA) [13], converting the small output currents  $I_i$  to voltage signals

$$U_i = R_f I_i = R_f S_{QPD} \phi_{e,i} \quad (3.1)$$

with the transimpedance  $R_f$ .

The vertical and horizontal position of the laser spot on the QPD, representing

---

<sup>1</sup>Parts of this chapter have been previously published in [60].

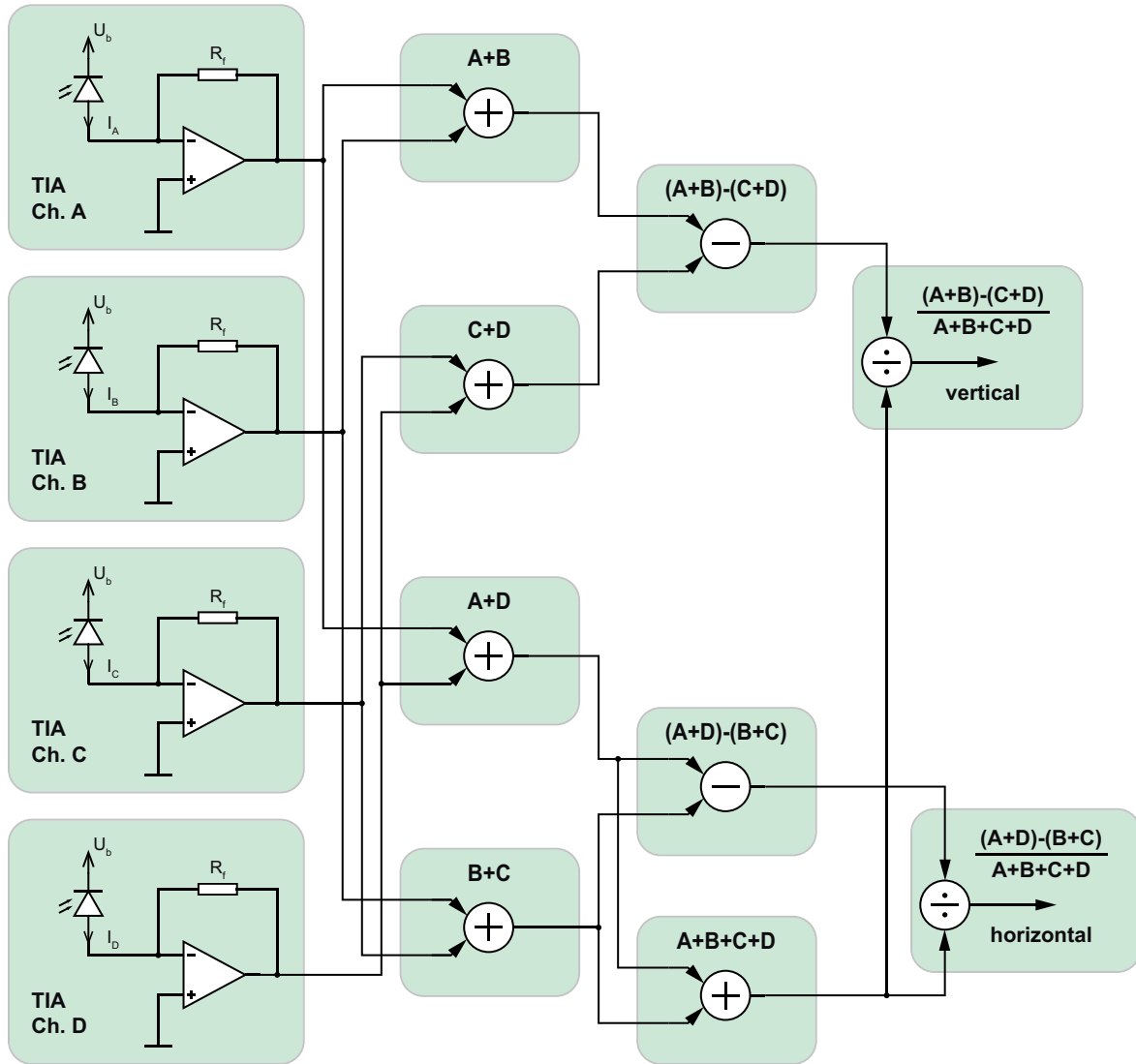


Figure 3.1: Schematic of a common deflection readout circuit design. The small currents of the photodiodes are converted to a voltage signal by the transimpedance amplifiers. The vertical and horizontal deflection signal according to Eq. 3.2 and 3.3 is generated by summing, differential, and divider stages.

deflection and friction, can be measured by [13]

$$U_{vert} = \frac{(U_A + U_B) - (U_C + U_D)}{U_A + U_B + U_C + U_D}, \quad (3.2)$$

and

$$U_{horiz} = \frac{(U_A + U_D) - (U_B + U_C)}{U_A + U_B + U_C + U_D}, \quad (3.3)$$

representing the vertical and horizontal deflection of the laser spot on the QPD. The voltage signals corresponding to the numerator of Eq. 3.2 and 3.3 can be generated by using different circuit design ideas. A common way is the utilization of summing and differential operational amplifier circuits [13] using six operational amplifiers [13]. Combining the summing and differential amplifiers for the vertical and horizontal branch in a differential amplifier with multiple inputs saves four operational amplifiers leading to a two amplifier design. The denominator of Eq. 3.2 and 3.3 normalizes the output signal with respect to the total irradiance on the detector. Fluctuations of the laser source as well as variations in the optical path can be compensated.

### 3.1.1 Differential amplifiers

To eliminate common mode noise that affects all photodiodes equally as fluctuations of the ambient light or intensity fluctuations from the laser centered on the QPD, a high common mode rejection ratio (CMRR) at the differential amplifier is essential [38]. Therefore the use of an instrumentation amplifier [13] with a high CMRR compared to discrete differential amplifiers has to be considered. It is important to notice that the high CMRR of the instrumentation amplifier mainly results from the first stage amplifying the differential signal while having unity gain for the common mode signal and therefore the CMRR depends on the instrumentation amplifier gain. Therefore the distribution of the total gain between the TIA and the instrumentation amplifier affects the CMRR.

To further investigate the expected common mode noise with respect to the differential noise, the following test setup shown in Fig. 3.2 is used. A laser source is comprised of a laser diode HL6312G (OpNext Japan, Inc., Yokohama City, Japan) with a collimator GS8020A (Roithner Lasertechnik GmbH, Vienna, Austria) mounted in a temperature controlled mount TCLDM9 (Thorlabs, Inc., Newton, US-NJ) and driven at 3.75 mW output power by a laser diode controller LDC501 (Stanford Research Systems, Inc., Sunnyvale, US-CA). The laser source is directed on a QPD S5981 (Hamamatsu, Shizuoka, Japan). The center of the laser spot is aligned at the gap separating two photodiodes leading to an equal distribution of the radiation. To reduce optical feedback noise due to back reflection of the laser light into the laser cavity [38], the normal axis of the QPD is slightly tilted with respect to the laser axis.

An average noise voltage density  $n_{TIA}$  of approximately  $200 \text{ nV}/\sqrt{\text{Hz}}$  is measured at the TIA outputs using the spectrum analyzer HP4395A (Agilent, Santa Clara, US-CA). It is assumed that the noise voltage density  $n_{TIA}$  is a combination of a correlated Gaussian part  $n_{cm}$ , equal from both TIAs, and an uncorrelated Gaussian part  $n_{diff}$ . By subtracting both output signals by an instrumentation amplifier AD8426 (Analog

### 3 High bandwidth deflection readout

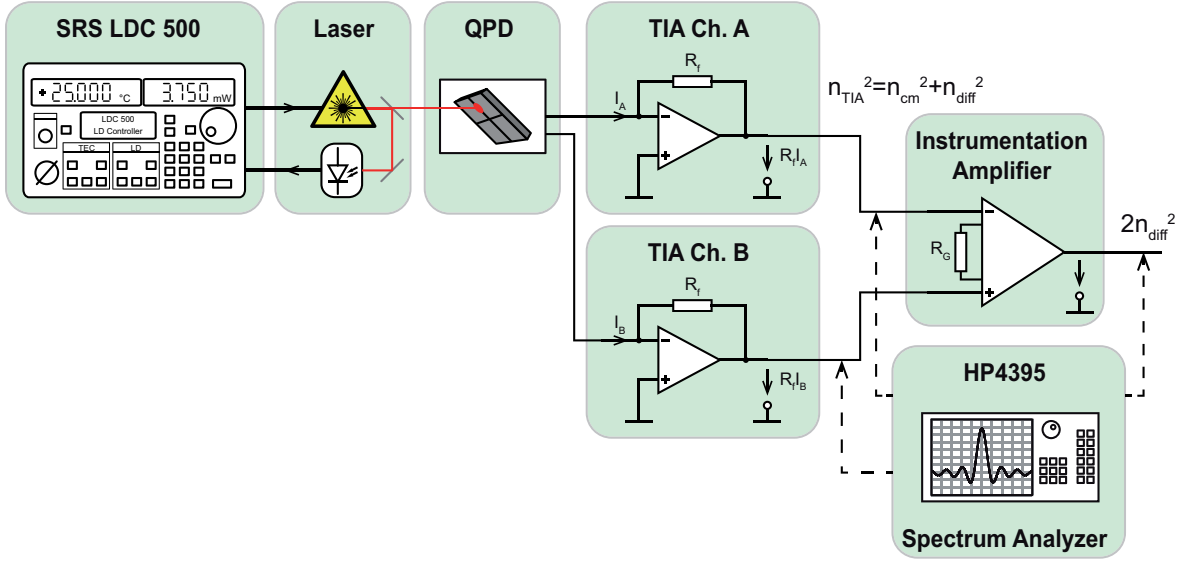


Figure 3.2: Setup to investigate the common mode Gaussian noise density  $n_{cm}$  with respect to the differential Gaussian noise density  $n_{diff}$ .

Devices, Norwood, US-MA) the common mode noise is suppressed by the high CMRR of more than 80 dB while the uncorrelated differential noise is superimposed leading to a measured noise voltage density of  $\sqrt{2n_{diff}^2} = 137 \text{ nV}/\sqrt{\text{Hz}}$  at the output. The common mode voltage noise density  $n_{cm}$  at the input of the instrumentation amplifier can be calculated by

$$n_{cm} = \sqrt{n_{TIA}^2 - n_{diff}^2}, \quad (3.4)$$

resulting in a common mode voltage noise density of  $n_{cm} = 175 \text{ nV}/\sqrt{\text{Hz}}$  and a differential voltage noise density  $n_{diff} = 97 \text{ nV}/\sqrt{\text{Hz}}$ . To suppress the common mode voltage noise at the output to less than 1% of the differential voltage noise density  $2n_{diff}$ , a differential amplifier with a CMRR of 40 dB is sufficient. Therefore the requirement of instrumentation amplifier can be revisited. Although fast integrated instrumentation amplifiers like the AD8429 (Analog Devices, Norwood, US-MA) can achieve a CMRR of 40 dB up to 1 MHz at unity gain, the bandwidth is limited to 15 MHz. Looking at other manufacturers the maximum bandwidth of instrumentation amplifiers is at 15 MHz for the LT1102 (Linear Technology Milpitas, US-CA), at 2 MHz for the INA331 (Texas Instruments, Dallas, US-TX), or at 2.5 MHz for the MAX4462 (Maxim Integrated Products, Sunnyval, US-CA).

The utilization of instrumentation amplifiers as differential amplifiers for the deflection readout circuit is a major bandwidth limitation. Additionally, the CMRR of standard high bandwidth differential amplifier can be sufficient to significantly reduce the common mode noise with respect to the differential noise. Therefore, while significantly suppressing common mode noise, a bandwidth limitation by instrumentation amplifiers is avoided by using standard differential amplifiers.

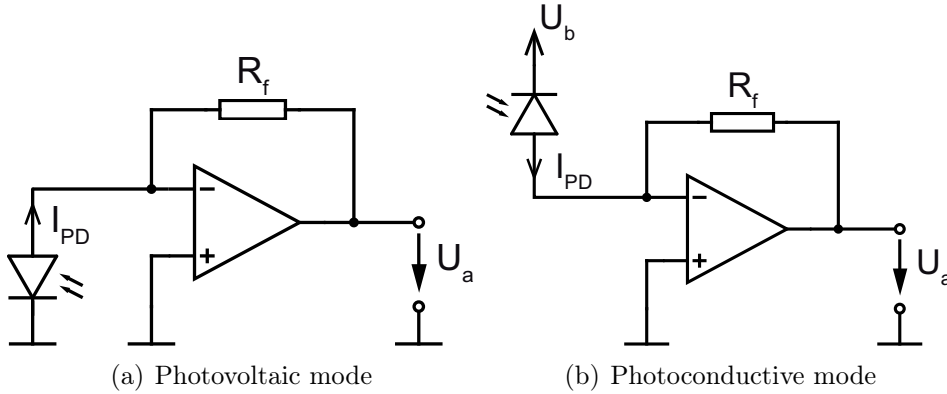


Figure 3.3: Transimpedance amplifier (TIA) configurations with the transimpedance  $R_f$ . The photodiode current  $I_{PD}$  is converted to the output voltage  $U_a = -R_f I_{PD}$ . In photovoltaic mode (a) the photodiode noise is reduced by virtually shorting the photodiode, while in photoconductive mode the bias voltage  $U_b$  reduces the response time of the photodiode.

### 3.1.2 Signal normalization

Dividing the resulting signal by the sum of all four quadrants leads to a deflection signal, independent of the actual total irradiation. Furthermore noise from laser fluctuations is canceled even if the laser is not centered on the QPD. As the laser output power in AFMs is usually monitored by a photodiode and stabilized by a feedback controller, noise arising from intensity fluctuations is rather small compared to other noise sources such as the photodiode shot noise [38]. Therefore the total deflection readout noise is not significantly reduced, although, the achievable bandwidth can be limited by the normalization.

The different reflection coefficients of the cantilevers as well as their size and shape leads to a wide variation of the total amount of light reflected to the QPD. Without signal normalization the amplitude of the deflection signal is proportional to the total irradiation on the QPD. Although the QPD is used as zero detector, a cantilever dependent variation of the reflected light affects the z-feedback loop. However the reflectivity can be assumed to be almost constant during the measurement. Therefore an initial correction of the deflection readout gain based on a single measurement of the total irradiation is sufficient. As the expected noise reduction can be neglected and the deflection readout gain can be adapted upfront, signal normalization should be avoided, at least if the bandwidth is limited by the normalization.

### 3.1.3 The transimpedance amplifier

Converting the small output current of a photodiode to a voltage signal, transimpedance amplifiers (TIA) in photovoltaic or photoconductive mode are used as shown in Fig. 3.3. In both modes the photodiode current  $I_{PD}$  is converted to the output voltage  $U_a = -R_f I_{PD}$  with the transimpedance  $R_f$ . In photovoltaic mode the photodiode noise is re-

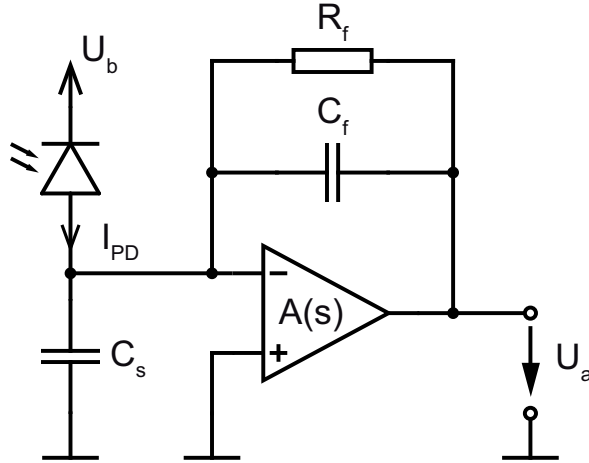


Figure 3.4: Transimpedance amplifier (TIA) with the source capacitance  $C_s$  as the input capacitance including the photodiode junction capacitance, the input capacitance of the operational amplifier, and the transmission line capacitance. The feedback capacitance  $C_f$  provides additional phase margin by compensating the phase lag due to the source capacitance  $C_s$ .  $A(s)$  denotes the open loop transfer function of the operational amplifier.

duced by virtually shorting the photodiode. In photoconductive mode the bias voltage  $U_b$  reduces the response time of the photodiode by reducing the junction capacitance. As the response time is increased, the leakage current increases too, while the photocurrent stays almost constant. For example the junction capacitance of the SPOT series QPDs (OSI Optoelectronics, Hawthorne, US-CA) drops from 14 pF/mm<sup>2</sup> at zero bias to 3 pF/mm<sup>2</sup> at a bias voltage of 10 V while the dark current increases from zero to 0.1 nA. For an exemplary TIA feedback resistance of 1 k $\Omega$ , the dark current of 0.1 nA results in a voltage noise of 100 nV, equivalent to the thermal noise of the feedback resistor when limited to 600 Hz. For a bandwidth of several MHz the voltage noise due to the dark current is neglectable in comparison to the thermal noise of the feedback resistor in the range of a few k $\Omega$ . Therefore the photoconductive mode is preferable for the high speed deflection readout with a bandwidth of several 10 MHz and a feedback resistance in the range of a few k $\Omega$ .

The stability and achievable bandwidth is analyzed by considering the circuit in Fig. 3.4. The source capacitance  $C_s$  shown in Fig. 3.4 is the input capacitance including the photodiode junction capacitance, the input capacitance of the operational amplifier, and the transmission line capacitance. The operational amplifiers transfer function  $A(s)$  can be represented by an integrator with a zero crossing frequency  $f_c$  as shown by the dotted line in Fig. 3.5. Concerning the feedback network the capacitance  $C_s$  forms a pole in the open loop transfer function

$$L(s) = - \underbrace{\frac{2\pi f_c}{s}}_{A(s)} \frac{1 + sR_f C_f}{1 + sR_f(C_f + C_s)}. \quad (3.5)$$

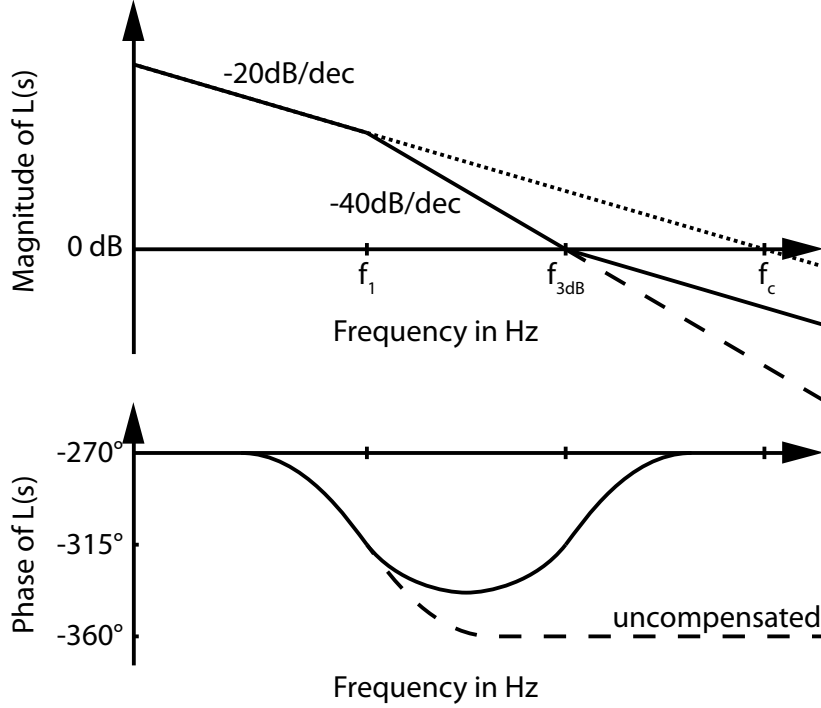


Figure 3.5: Open loop transfer function  $L(s)$  as expressed in Eq. 3.5 for the TIA shown in Fig. 3.4. The dotted line shows the operational amplifiers open loop gain  $A(s)$ . The dashed line shows the uncompensated case with  $C_f = 0$ .

The additional pole at

$$f_1 = \frac{1}{2\pi R_f (C_f + C_s)} \quad (3.6)$$

results in a phase lag as shown by the dashed line in Fig. 3.5. Stability with a minimum phase margin of  $45^\circ$  can be guaranteed by placing a compensating zero at [61]

$$f_{3dB} = \sqrt{f_1 f_c} = \sqrt{\frac{f_c}{2\pi R_f (C_f + C_s)}}. \quad (3.7)$$

As shown in Fig. 3.4 the zero can be realized by a capacitor [61]

$$C_f = \sqrt{\frac{C_s}{2\pi R_f f_c}} \quad \text{for } C_s \gg C_f \quad (3.8)$$

in parallel to the feedback resistor  $R_f$ .

Although stability is guaranteed and peaking of the closed loop transfer function is limited, the bandwidth of the TIA is limited to  $f_{3dB}$ . Considering Eq. 3.7, a high zero crossing frequency  $f_c$ , a low transimpedance  $R_f$ , and a small source capacitance  $C_s$  gives a high bandwidth of the TIA.

As the deflection readout noise is a determining factor of the achievable resolution, using higher bandwidth operational amplifier with a higher zero crossing frequency

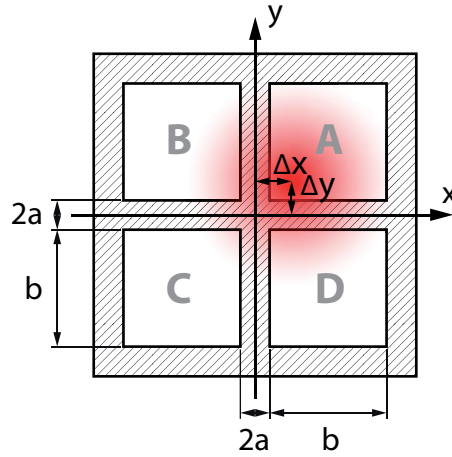


Figure 3.6: Geometry of a QPD with four quadratic photodiodes A, B, C, and D, separated by a small gap of width  $2a$ . The laser spot is deflected by  $(\Delta x, \Delta y)$  from the center of the QPD.

$f_c$  should be avoided as their noise density is usually higher than the noise density of low bandwidth ones. Using a lower transimpedance  $R_f$  leads to a lower deflection sensitivity and therefore degrades the achievable resolution. Without degrading the achievable resolution the bandwidth can be increased by the selection of a QPD with a small junction capacitance  $C_s$ . A reduction of the junction capacitance can be attained by sufficiently reverse biasing the QPD in photoconductive mode Fig. 3.3b and by the selection of a small QPD with a small active area.

## 3.2 The influence of the detector geometry<sup>2</sup>

The junction capacitance of the QPD is a determining factor for the bandwidth of the TIA (see Sec. 3.1.3). Therefore the selection of a QPD with a small active area is preferable. To further investigate the scaling effects the output signal and sensitivity of the QPD is analyzed with respect to the relation between the detector size, the width of the separation gap, and the laser spot size.

A common QPD as shown in Fig. 3.6 consists of four quadratic photodiodes with a side length of  $b$ . A small gap separates the single photodiodes by  $2a$ . Camera based measurements have shown that the intensity distribution of the laser spot on the QPD is close to the intensity distribution of a Gaussian beam (data not shown). Assuming the laser beam to be Gaussian the intensity distribution is given by [63]

$$I(x, y, s) = I_0 \left( \frac{w_0}{w(s)} \right)^2 e^{-\frac{2(x^2+y^2)}{w(s)^2}}, \quad (3.9)$$

with the radius  $w(s)$  at a distance  $s$  from the focal point and a maximum intensity  $I_0$  at the center of beam waist with a radius  $w_0$ .

<sup>2</sup>This section is part of [60] and [62].

### 3 High bandwidth deflection readout

The radiant power  $\phi_{e,i}$  incident on a single photodiode  $i \in \{A, B, C, D\}$  as part of the total radiant power  $\phi_e$  is calculated by the integration of  $I(x, y, s)$ . For the geometry shown in Fig. 3.6 the integral for each quadrant is given by

$$\phi_{e,A}(\Delta x, \Delta y) = \int_{a-\Delta y}^{a+b-\Delta y} \int_{a-\Delta x}^{a+b-\Delta x} I(x, y, s) dx dy, \quad (3.10)$$

$$\phi_{e,B}(\Delta x, \Delta y) = \int_{a-\Delta y}^{a+b-\Delta y} \int_{-a-b-\Delta x}^{-a-\Delta x} I(x, y, s) dx dy, \quad (3.11)$$

$$\phi_{e,C}(\Delta x, \Delta y) = \int_{-a-b-\Delta y}^{-a-\Delta y} \int_{-a-b-\Delta x}^{-a-\Delta x} I(x, y, s) dx dy, \quad (3.12)$$

and

$$\phi_{e,D}(\Delta x, \Delta y) = \int_{-a-b-\Delta y}^{-a-\Delta y} \int_{a-\Delta x}^{a+b-\Delta x} I(x, y, s) dx dy, \quad (3.13)$$

with the deflection  $(\Delta x, \Delta y)$  of the laser spot.

Combining Eq. 3.9 – 3.13, and 3.1 with Eq. 3.2 and 3.3 leads to the position dependent signals

$$U_{vert}(\Delta x, \Delta y) = \frac{R_f S_{QPD} \phi_e}{4} [g(\Delta x) + g(-\Delta x)][g(\Delta y) - g(-\Delta y)] \quad (3.14)$$

and

$$U_{horiz}(\Delta x, \Delta y) = \frac{R_f S_{QPD} \phi_e}{4} [g(\Delta x) - g(-\Delta x)][g(\Delta y) + g(-\Delta y)] \quad (3.15)$$

with

$$g(\delta) = \operatorname{erf}\left(\frac{\sqrt{2}(a+b-\delta)}{w(s)}\right) - \operatorname{erf}\left(\frac{\sqrt{2}(a-\delta)}{w(s)}\right) \quad (3.16)$$

where  $\operatorname{erf}(x)$  denotes the error function

$$\operatorname{erf}(x) = \frac{2}{\sqrt{\pi}} \int_0^x e^{-\tau^2} d\tau. \quad (3.17)$$

#### 3.2.1 Experimental verification

To evaluate Eq. 3.14 and 3.15 the setup shown in Fig. 3.7 is used. A QPD S5981 (Hamamatsu, Shizuoka, Japan) with  $5 \times 5 \text{ mm}^2$  photodiodes separated by gaps of  $30 \mu\text{m}$  is mounted on a motorized xy-stage (two PT1 with Z825B and TDC001, Thorlabs, Inc., Newton, US-NJ) in front of a laser source. The laser source consists of a laser diode HL6312G (OpNext Japan, Inc., Yokohama City, Japan) with a collimator GS8020A (Roithner Lasertechnik GmbH, Vienna, Austria) mounted in a temperature controlled mount TCLDM9 (Thorlabs, Inc., Newton, US-NJ) and driven by a laser diode controller LDC501 (Stanford Research Systems, Inc., Sunnyvale, US-CA). The beam is shaped by an aperture stop of 1.2 mm followed by a beam expander magnifying the

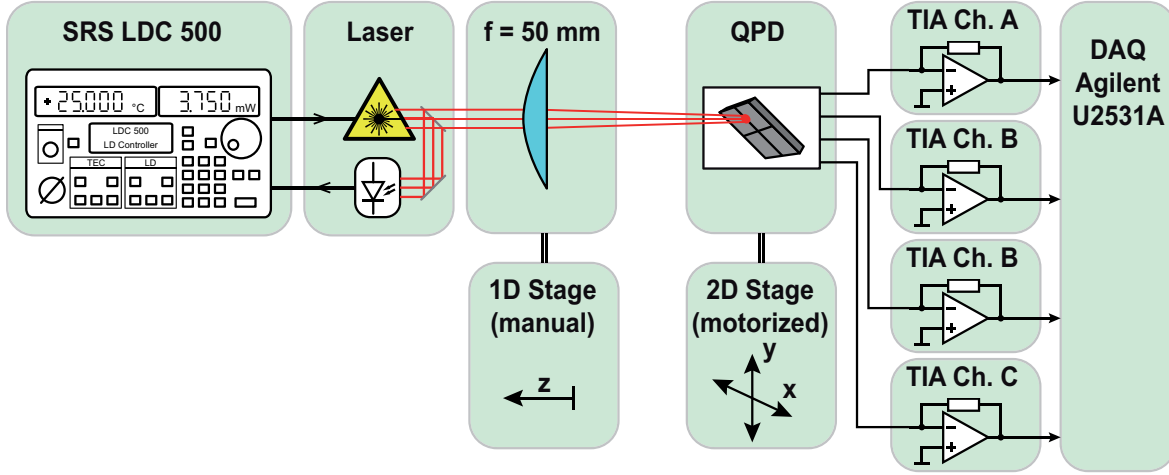


Figure 3.7: Setup to measure the output signal with respect to the spot size and position on the QPD. The spot size can be adjusted by the position of the focusing lens according to a camera based measurement of the beam profile.

beam 3 times to 3.6 mm. The beam expander is built of two plano convex lenses with a focal length of 75 mm and 25.4 mm (LA1608-A and LA1951-A, Thorlabs, Inc., Newton, US-NJ) with a  $25 \mu\text{m}$  pinhole at the focal plane.

The sensitivity of  $0.43 \text{ A/W}$  of the QPD is calculated for the laser wavelength of  $\lambda = 635 \text{ nm}$  from the measurement of the radiant power with an optical power meter (PM320E, Thorlabs, Inc., Newton, US-NJ) and the output voltage of the TIA with a transimpedance  $R_f = 1 \text{ k}\Omega$ . To set the spot diameter on the QPD the distance to a focusing lens with a focal length of  $f = 50 \text{ mm}$  (LA1131-A, Thorlabs, Inc., Newton, US-NJ) is adjusted according to a camera based measurement of the beam profile.

Using Eq. 3.14, Fig. 3.8 shows the expected output voltage  $U_{vert}$  with respect to the displacement of the laser spot with a spot diameter of 3 mm (100 times the gap width). Fig. 3.9 shows the measured values at 200 discrete points on the QPD. In comparison to the calculated values of Fig. 3.8 the maximum deviation is 5.554% as shown in Fig. 3.10.

The steep area around the horizontal axis ( $\Delta y = 0$ ) shows the almost linear range of the deflection measurement. If the spot moves out of the linear range the output of the QPD starts to saturate. A detection range can be defined for example by a certain deviation from a linear response [64]. At the border of the QPD the signal drops due to loss of radiation incident on the detector. A drop of the output voltage along the vertical separation gap is barely visible as the spot diameter is 100 times the gap width.

In contrast Fig. 3.11 shows the output voltage  $U_{vert}$  around the center of the QPD with a spot size equal to the gap width. In comparison to Fig. 3.8, the output voltage along the vertical gap drops by 95% of the maximum output voltage as most of the beam is shadowed by gap. Additionally a saddle point along the horizontal axis ( $\Delta y = 0$ ) can be seen and the steep parts are shifted towards the edges of the separation gap.

Fig. 3.12 shows the measured values at 200 discrete points on the QPD for a spot size of  $30 \mu\text{m}$  equal to the width of the separation gap. Fig. 3.13 shows a significant

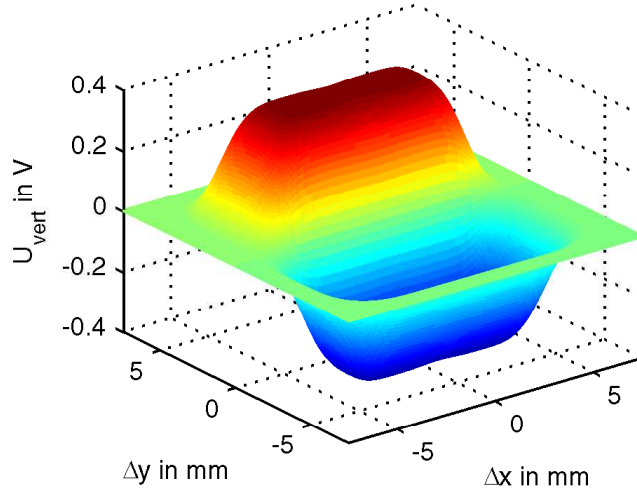


Figure 3.8: Simulated output voltage  $U_{vert}$  with respect to the displacement of the laser spot with a spot diameter of 3 mm on a QPD with  $5 \times 5 \text{ mm}^2$  photodiodes separated by a gap of  $30 \mu\text{m}$  ( $R_f = 1 \text{ k}\Omega$ ,  $S_{QPD} = 0.43 \text{ A/W}$ ,  $\phi_e = 850 \mu\text{W}$ ).

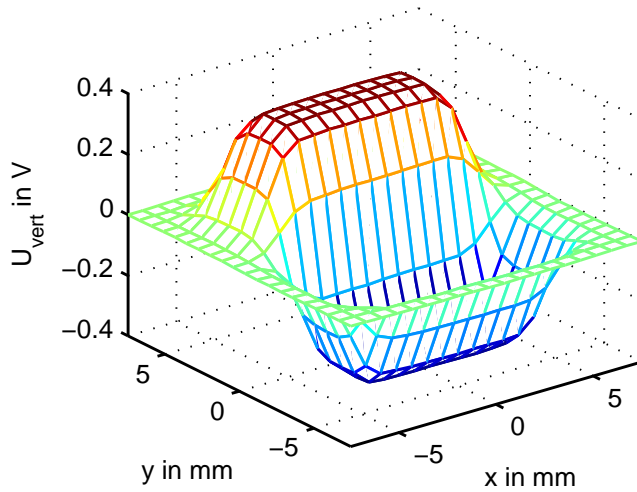


Figure 3.9: Measured output voltage  $U_{vert}$  with respect to the displacement of the laser spot with a spot diameter of 3 mm on the Hamamatsu S5981 QPD with  $5 \times 5 \text{ mm}^2$  photodiodes separated by a gap of  $30 \mu\text{m}$  ( $R_f = 1 \text{ k}\Omega$ ,  $S_{QPD} = 0.43 \text{ A/W}$ ,  $\phi_e = 850 \mu\text{W}$ ).

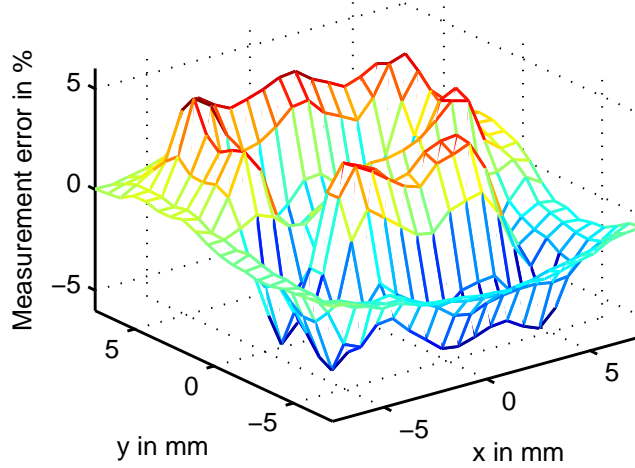


Figure 3.10: Deviation of the measured (Fig. 3.9) from the calculated (Fig. 3.8) output of the QPD with  $5 \times 5 \text{ mm}^2$  photodiodes separated by a gap of  $30 \mu\text{m}$ .

deviation of 75 % of the measured values from the calculated values. The signal drops by less than 30 %, although a drop in the output signal around 95 % is expected as  $4\sigma$  of the Gaussian beam are covered by the gap. The gap width of  $30 \mu\text{m}$  specified in the data sheet is verified by optical microscopy. Also measurements at the SPOT-4D (OSI Optoelectronics, Hawthorne, US-CA) QPD with a specified gap width of  $127 \mu\text{m}$ , significantly larger than the  $30 \mu\text{m}$  spot diameter, do not show the expected drop in the output signal (data not shown). A possible explanation may be that most of the light incident on the gap is not reflected, rather the energy is absorbed in the gap, creating electron-hole pairs leading to a photocurrent in the active areas. So, the actual influence of the gap is less than expected by the previous assumptions, although some change in intensity can be observed for the  $30 \mu\text{m}$  gap QPD.

### 3.2.2 Quadrant photodetector sensitivity

To find the maximum sensitivity the directional sensitivity to a displacement of the laser spot in the vertical or horizontal direction is calculated by the derivative of the position dependent output in the respective direction:

$$S_{vert} = \frac{dU_{vert}(\Delta x, \Delta y)}{d\Delta y} \quad (3.18)$$

$$S_{horiz} = \frac{dU_{horiz}(\Delta x, \Delta y)}{d\Delta x}. \quad (3.19)$$

Fig. 3.14 shows the simulated directional sensitivity  $S_{vert} = dU_{vert}(\Delta x, \Delta y)/d\Delta y$  for gap size 100 times the gap width. The vertical sensitivity is maximal if the spot is centered on the horizontal separation gap, although the sensitivity drops by less than 1.4 % at the center of the QPD due to the vertical separation gap. At the border of

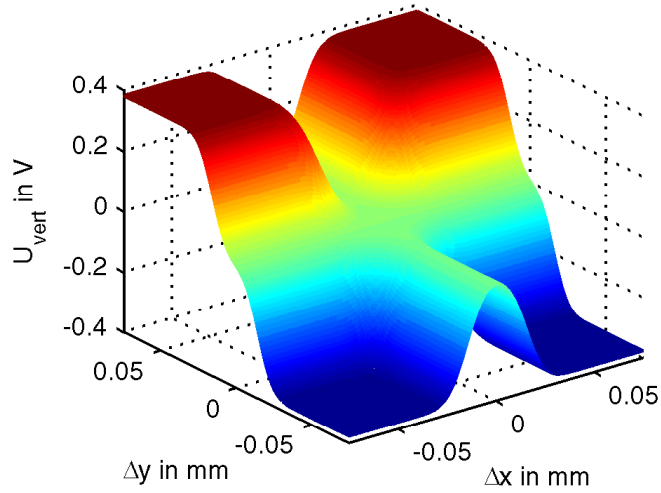


Figure 3.11: Simulated output voltage  $U_{vert}$  with respect to the displacement of the laser spot with a spot diameter of  $30\ \mu\text{m}$  on a QPD with  $5 \times 5\ \text{mm}^2$  photodiodes separated by a gap of  $30\ \mu\text{m}$  ( $R_f = 1\ \text{k}\Omega$ ,  $S_{QPD} = 0.43\ \text{A/W}$ ,  $\phi_e = 850\ \mu\text{W}$ ). A deflection of  $\pm 75\ \mu\text{m}$  from the center of the QPD is shown.

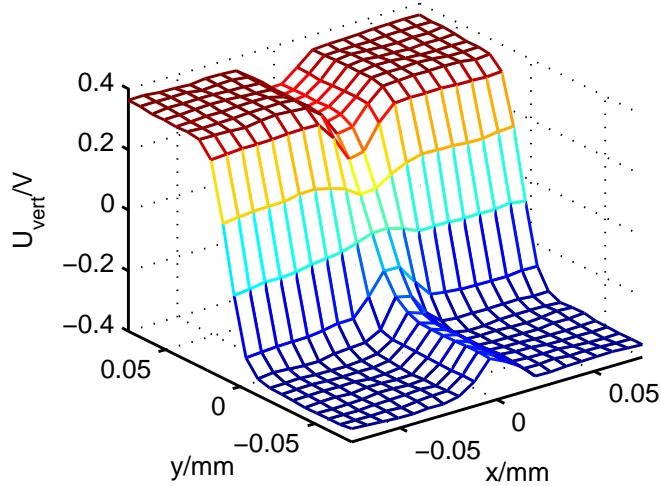


Figure 3.12: Measured output voltage  $U_{vert}$  with respect to the displacement of the laser spot with a spot diameter of  $30\ \mu\text{m}$  on the Hamamatsu S5981 QPD with  $5 \times 5\ \text{mm}^2$  photodiodes separated by a gap of  $30\ \mu\text{m}$  ( $R_f = 1\ \text{k}\Omega$ ,  $S_{QPD} = 0.43\ \text{A/W}$ ,  $\phi_e = 850\ \mu\text{W}$ ). A deflection of  $\pm 75\ \mu\text{m}$  from the center of the QPD is shown.

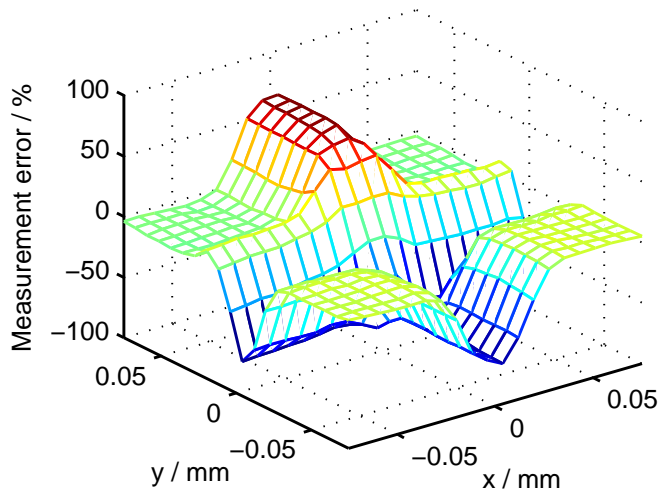


Figure 3.13: Deviation of the measured (Fig. 3.12) from the calculated (Fig. 3.11) output of the QPD with  $5 \times 5 \text{ mm}^2$  photodiodes separated by a gap of  $30 \mu\text{m}$ .

the QPD the sensitivity drops to on half of maximum sensitivity along the separation gap as only half of the total radiation power hits the detector.

In contrast to Fig. 3.14, Fig. 3.15 shows the simulated directional sensitivity  $S_{vert} = dU_{vert}(\Delta x, \Delta y)/d\Delta y$  around the center of the QPD with a spot size equal to the gap width. The vertical sensitivity is no more maximal if the spot is centered on the horizontal separation gap away from center of the QPD. The vertical sensitivity is maximal if the center of the spot is aligned at any of the two edges of the horizontal gap away from the vertical gap and the border of the QPD. Since in that case only one half of the spot appears at the active area of the QPD and the other half is almost covered by the gap the sensitivity drops by 49% compared to Fig. 3.14.

In general besides the vertical deflection representing the topography the horizontal deflection representing torsion due to friction is of interest. Fig. 3.16 shows an overlay of the vertical and horizontal directional sensitivity. On top of Fig. 3.16 the setpoint with equal high sensitivities is denoted by the isolines of the product of the vertical and horizontal directional sensitivity resulting in four distinct points with a maximum sensitivity for the vertical and horizontal deflection. The maximum sensitivity in one direction as well as the maximum equal sensitivity in both directions is plotted with respect to the normalized spot size  $w(s)/a$  in Fig. 3.17. The maximum sensitivity drops to 50% for a spot small compared to the gap size as one half of the spot is covered by the gap. The maximum equal sensitivity drops to around 80% at a spot size ten times the gap width. Therefore, to ensure a maximum drop of the maximum equal sensitivity of no more than 20%, a spot size greater or equal than ten times the gap width is necessary [62].

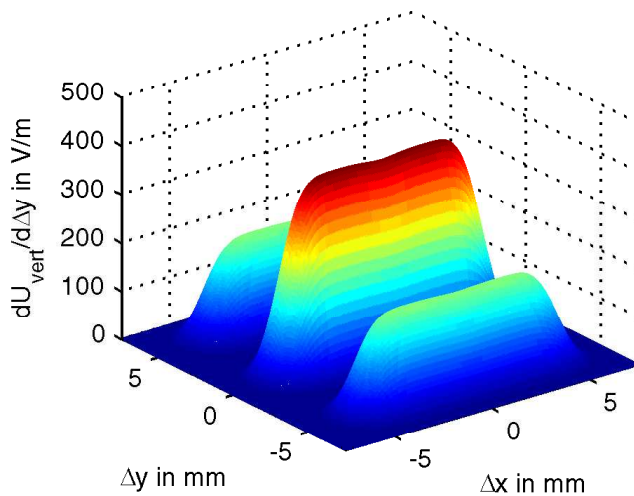


Figure 3.14: Simulated directional sensitivity to a vertical displacement of the laser spot with a spot diameter of 3 mm on a QPD with  $5 \times 5 \text{ mm}^2$  photodiodes separated by a gap of  $30 \mu\text{m}$ . The influence of the gap on the sensitivity can be neglected.

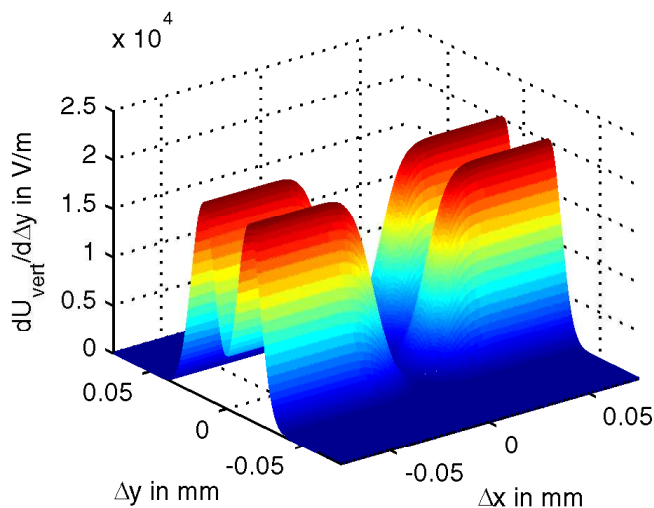


Figure 3.15: Simulated directional sensitivity to a vertical displacement of the laser spot with a spot diameter of  $30 \mu\text{m}$  on a QPD with  $5 \times 5 \text{ mm}^2$  photodiodes separated by a gap of  $30 \mu\text{m}$ . The sensitivity around  $\pm 75 \mu\text{m}$  off the center of the QPD is shown. The vertical sensitivity is maximal if the center of the spot is aligned at any of the two edges of the horizontal gap and away from the vertical gap.

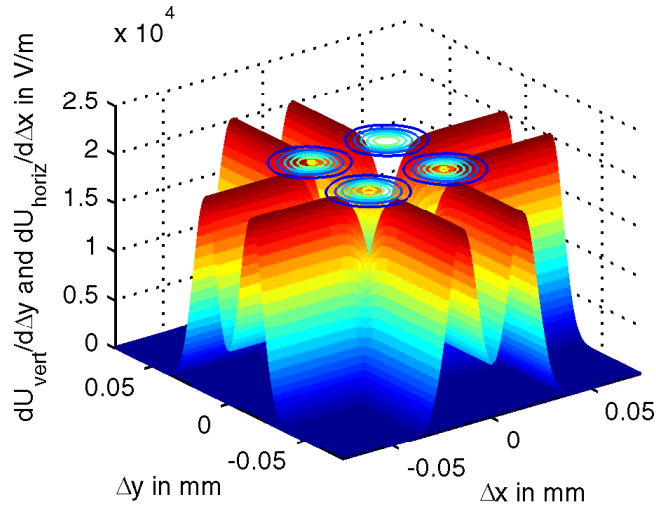


Figure 3.16: Overlay of vertical and horizontal sensitivity for a spot size of  $30\ \mu\text{m}$  on a QPD with  $5 \times 5\ \text{mm}^2$  photodiodes separated by a gap of  $30\ \mu\text{m}$ . On top, the isolines of the product of the vertical and horizontal sensitivity, indicating the optimal setpoints with a maximum value for equal sensitivities. The sensitivity around  $\pm 75\ \mu\text{m}$  off the center of the QPD is shown.

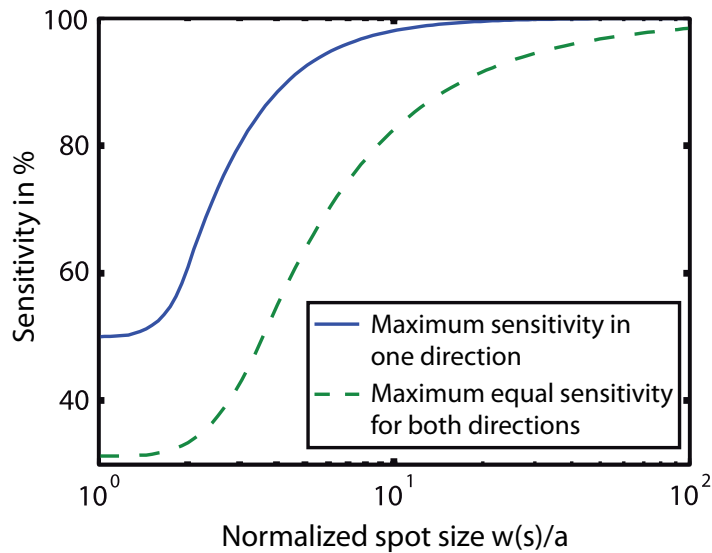


Figure 3.17: Maximum deflection sensitivity for a one dimensional measurement (solid) and maximum equal deflection sensitivity for a horizontal and vertical measurement (dashed) with respect to the normalized spot size.

### Analytical approach

When designing the deflection readout of an AFM, the relation between the actual deflection of the cantilever and output signal from the deflection readout circuit is of interest. For example by designing the deflection readout circuit for an AFM it is beneficial if the electronic noise can be related to an equivalent deflection noise. Although the electronic noise can be estimated, simulated, and measured, the equivalent deflection noise is determined by the entire deflection readout mechanism. For example noise budgeting during the design or the comparison of different electronic designs requires detailed knowledge of the entire system to relate the electronic noise to the equivalent deflection noise. Therefore an analytical expression that allows the estimation of the deflection readout sensitivity is derived from previous results.

It is assumed that the size of the QPD is large and the vertical deflection  $\Delta y$  is small compared to the half width  $w(s)$  of the laser spot on the QPD:

$$\Delta x = 0 \quad \text{and} \quad \Delta y \ll w(s) \ll b. \quad (3.20)$$

With these assumptions Eq. 3.14 and 3.16 are simplified to

$$U'_{vert}(\Delta x, \Delta y) = \frac{R_f S_{QPD} \phi_e}{2} [g'(\Delta y) - g'(-\Delta y)], \quad (3.21)$$

and

$$g'(\delta) = 1 - \operatorname{erf}\left(\frac{\sqrt{2}(a - \delta)}{w(s)}\right). \quad (3.22)$$

The sensitivity of the deflection signal with respect to the small deflection  $\Delta y \ll w(s)$  on the QPD is calculated by the derivative of Eq. 3.21 as

$$\frac{dU'_{vert}}{d\Delta y} = R_f S_{QPD} \phi_e \frac{2\sqrt{2}}{\sqrt{\pi}w(s)} \quad (3.23)$$

using

$$\frac{d}{dx} \operatorname{erf}(x) = \frac{2}{\sqrt{\pi}} e^{-x^2}. \quad (3.24)$$

With the assumptions from [5] the static deflection  $\Delta z_{defl}$  of the free end of the cantilever causes a deflection

$$\Delta y(\Delta z_{defl}) = 3 \frac{s}{l} \cdot \Delta z_{defl} \quad (3.25)$$

on the QPD, where  $l$  is the cantilever length and  $s$  is the distance between the cantilever and the QPD. If the Gaussian beam is focused on the cantilever the half width of the spot on the QPD is [63]

$$w(s) = \frac{\lambda}{\pi w_0} s. \quad (3.26)$$

Using Eq. 3.23, 3.25, and 3.26, the sensitivity of the deflection signal with respect to the static deflection  $\Delta z_{defl}$  of the free end of the cantilever is the deflection readout

### 3 High bandwidth deflection readout

sensitivity

$$\frac{dU'_{vert}}{d\Delta z_{defl}} = R_f S_{QPD} \phi_e 6\sqrt{2\pi} \frac{w_0}{l \cdot \lambda}. \quad (3.27)$$

This is an important result as it allows to relate the output voltage of the deflection readout circuit to an equivalent cantilever deflection, if the transimpedance  $R_f$ , the sensitivity  $S_{QPD}$  of the QPD, the incident laser power  $\phi_e$ , the laser wavelength  $\lambda$ , the diameter  $2w(s)$  of the laser spot on the cantilever, and the cantilever length are known. If the transimpedance  $R_f$ , the sensitivity  $S_{QPD}$ , or the incident laser power  $\phi_e$  are not known, the deflection readout sensitivity can be estimated by the knowledge of the maximum output voltage  $U_{max}$  measured by aligning the laser spot on single quadrant or calculating  $U_{max}$  as the sum of the single output signals. Therefore Eq. 3.27 simplifies to

$$\frac{dU'_{vert}}{d\Delta z_{defl}} = U_{max} 6\sqrt{2\pi} \frac{w_0}{l \cdot \lambda}. \quad (3.28)$$

## 3.3 Implementation and measurement results

This section shows the realization and validation of a high bandwidth deflection readout system based on the findings from the previous sections.

### 3.3.1 Selection of the QPD

As discussed in Sec. 3.1.3, the photodiode junction capacitance is a determining factor for the achievable bandwidth of the TIA. The junction capacitance can be reduced by selecting a QPD with a small active area. By reducing the active area it is important to consider the spot size on the QPD. It can be calculated using Eq. 3.9, that 91 % of the total radiant power is covered by the active area, if the spot is centered and the width of the active area is equal to spot diameter. Therefore a rule of thumb can be that the laser spot diameter on the QPD should not exceed the width of the active area to cover at least 91 % of the total radiant power. Additionally as discussed in Sec. 3.2.2, the laser spot size on the QPD should be at least 10 times the gap width to avoid a drop of more than 20 % of the maximum equal sensitivity for both, the vertical and horizontal deflection [62]. All three conditions are met by a laser spot size of 1.3 mm on the SPOT-4D (OSI Optoelectronics, Hawthorne, US-CA) with photodiodes of  $1.3 \times 1.3 \text{ mm}^2$  separated by a gap of  $127 \mu\text{m}$ . The junction capacitance of the the SPOT-4D QPD is as low as 5 pF at a reverse voltage of  $-10 \text{ V}$ . A rise time of 3 ns is specified in the datasheet for a reverse voltage of  $-10 \text{ V}$ , a load resistance of  $50 \Omega$ , and a wavelength of  $\lambda = 780 \text{ nm}$ . Assuming the rise time is specified from 10 % to 90 % the equivalent cutoff frequency for a first order low pass can be calculated by

$$f_c = \frac{\ln(9)}{2\pi t_r}, \quad (3.29)$$

leading to 115.57 MHz.

### 3.3.2 Laser power considerations

The shot noise current density  $n_{i,shot} = \sqrt{2eI_0}$  [5] of the photodiode is proportional to the square root of the DC current  $I_0$  times the elementary charge  $e$ . As the TIA output signal is proportional to the DC current  $I_0$  the SNR increases with the square root of the laser power. However, the cantilever is heated up by the laser what leads to additional Brownian noise when increasing the laser power. Furthermore considering laser safety, special laser safety precautions can be avoided using a Class 1 or 2 laser [65] as that is safe at least due to the blink reflex. Therefore a reasonable upper limit for the continuous output power is 1 mW for a wavelength between 400 nm and 700 nm. A maximum incident power of 1 mW leads to a current of 0.4 mA from the photodiode with a sensitivity of 0.4 A/W at  $\lambda = 635$  nm. For this configuration, the shot noise current density is 11.3 pA/ $\sqrt{\text{Hz}}$  at 0.4 mA.

### 3.3.3 Selection of the feedback resistor

To avoid electronic signal reflections on the transmission lines a matched design is desired. Due to the good availability of components and instruments, 50  $\Omega$  is used as matched impedance. To avoid the requirement of line drivers, the maximum output voltage should be limited. Using a transimpedance  $R_f$  of 1 k $\Omega$  results in a output voltage of 0.4 V at an input current of 0.4 mA (see Sec. 3.3.2). In a design matched to 50  $\Omega$  the output voltage of 0.4 V leads to an output current equal or less than 8 mA depending on the output resistance of the operational amplifier. A output current of 8 mA is in the linear output current range of most operational amplifiers. Therefore a transimpedance of 1 k $\Omega$  is a good choice for an incident laser power of 1 mW.

### 3.3.4 Selection of the operational amplifier

A photodiode current of 0.4 mA (see Sec. 3.3.2) leads to a shot noise current density of 11.3 pA/ $\sqrt{\text{Hz}}$ . With the transimpedance  $R_f = 1$  k $\Omega$  the shot noise current density of 11.3 pA/ $\sqrt{\text{Hz}}$  results in a voltage noise density  $n_{shot}$  of 11.3 nV/ $\sqrt{\text{Hz}}$ . The thermal noise density  $n_{therm} = \sqrt{4k_B T R}$  [5] of the feedback resistor  $R_f = 1$  k $\Omega$  is 4.04 nV/ $\sqrt{\text{Hz}}$ . The square root of the sum of the squared thermal and shot noise density gives a total output noise density of 12 nV/ $\sqrt{\text{Hz}}$ . Selecting the operational amplifier the square root of the sum of the squared input current noise density times  $R_f$  and the input voltage noise density should be significantly below the 12 nV/ $\sqrt{\text{Hz}}$ . Selecting the low noise operational amplifier ADA4895 (Analog Devices, Norwood, US-MA) leads to a total noise density of 12.15 nV/ $\sqrt{\text{Hz}}$  at 100 kHz. Due to the  $1/f$ -noise the total noise density increases to 18.55 nV/ $\sqrt{\text{Hz}}$  at 10 Hz.

### 3.3.5 Selection of the feedback capacitor

Neglecting the stray capacitance of the printed circuit board, the source capacitance  $C_s$  as sum of the photodiode junction capacitance and the input capacitance of the operational amplifier is 16 pF. An initial calculation of  $C_f$  using Eq. 3.8 leads to 1.6 pF. As  $C_f$  is in the order of  $C_s$  the selection of  $C_f$  according to Eq. 3.8 results in a phase

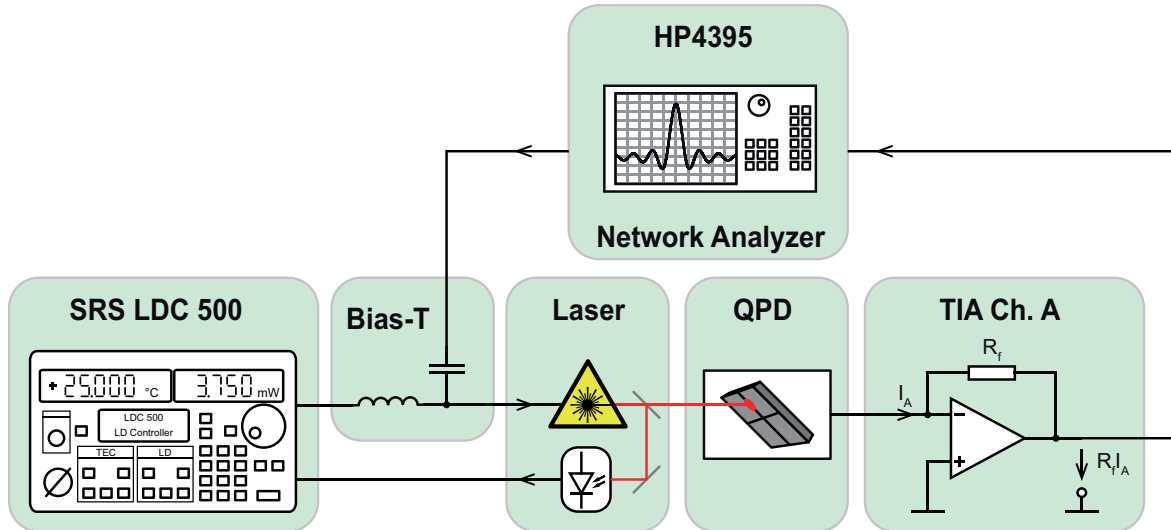


Figure 3.18: Setup to measure the transfer function from the laser source to the TIA output. The laser source is modulated by the output of the network analyzer and the output signal of the TIA corresponding to the quadrant with the laser spot aligned on it is used as the input to the network analyzer.

margin of more than  $45^\circ$ . Further reducing  $C_f$  to 1.2 pF reduces the phase margin to approximately  $45^\circ$ .

### 3.3.6 Bandwidth measurement setup

To determine the bandwidth of the deflection readout, the setup as shown in Fig. 3.18 is used. The laser source, previously used for the experimental verification in Sec. 3.2.1, is driven at an output power of 1 mW.

The deflection of a cantilever in the AFM leads to a change of the irradiance on the QPD. For a small deflection within the linear range of the QPD the output signal of the QPD is proportional to the cantilever deflection. That means that a sinusoidal motion of the cantilever leads to a sinusoidal change of the irradiance. To get rid of any cantilever or actuator dynamics, the changing irradiance on the QPD is emulated by modulating the laser source by the output of the network analyzer HP4395A (Agilent, Santa Clara, US-CA).

The output signal of the TIA corresponding to the quadrant with the laser spot aligned on it is used as the input to the network analyzer.

### 3.3.7 Bandwidth measurement results

Measuring the detection bandwidth using the setup presented in Sec. 3.3.6, gives the transfer function shown in Fig. 3.19. The transfer function is measured between 100 kHz and 500 MHz. The decay at low frequencies is due to the bias tee with a specified cutoff frequency of 100 kHz. It can be assumed that the three dips at 1.8 MHz, 4.4 MHz, and 12 MHz are frequency dependent variations in the output of the modulated laser source

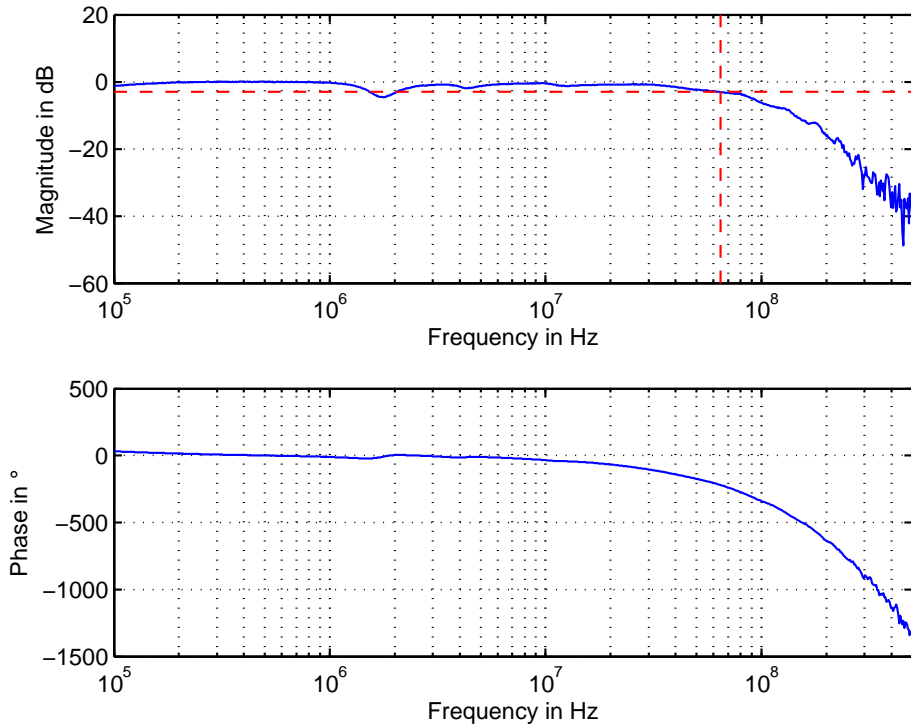


Figure 3.19: Frequency response of the photodiode and the transimpedance amplifier measured with the setup shown in Fig. 3.18.

as they can be seen in similar measurements with different QPDs and TIAs at the same frequencies (data not shown). The magnitude response is normalized by the average of 10 consecutive measurement points in the range from 477 kHz to 523 kHz. The achieved  $-3$  dB detection bandwidth is 64.5 MHz.

### 3.3.8 Deflection noise measurement

A high speed differential amplifier with a bandwidth of 74 MHz is used to measure the deflection i.e. the difference in the output signal of two consecutive quadrants. The voltage noise density shown in Fig. 3.20 is measured at the output of the transimpedance and the differential amplifier by a spectrum analyzer (HP4395A, Agilent, CA, USA). An average voltage noise density of  $12 \text{ nV}/\sqrt{\text{Hz}}$  (blue) is measured at the output of the TIA if the laser is switched off. The voltage noise density at the output of the differential amplifier is  $57 \text{ nV}/\sqrt{\text{Hz}}$  (red) without and  $69 \text{ nV}/\sqrt{\text{Hz}}$  (green) with a laser beam incident on the QPD. It is assumed that source the of the spikes visible in the noise spectrum of the differential amplifier with a laser beam incident on the QPD are emissions from the laser source as they are not visible if the laser is switched off. Using Eq. 3.27, a deflection noise density of  $62 \text{ fm}/\sqrt{\text{Hz}}$  is calculated for a cantilever length of  $l = 100 \mu\text{m}$ , a spot diameter of  $2w_0 = 30 \mu\text{m}$ , and a wavelength  $\lambda = 635 \text{ nm}$ . This leads to a deflection noise of 0.5 nm at a bandwidth of 64.5 MHz.

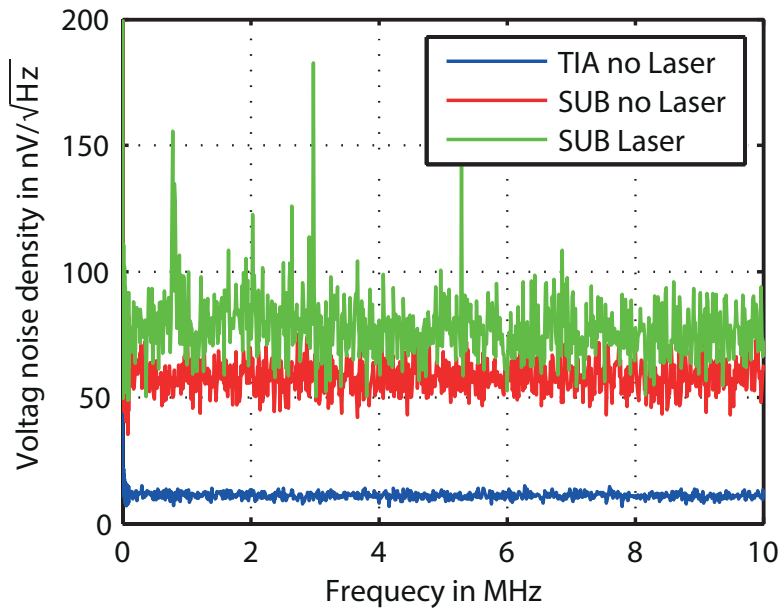


Figure 3.20: The voltage noise density measured at the output of the TIA with the laser source switched off (blue) and at the output of the differential amplifier with the laser source switched off (red) and on (green).

### 3.3.9 Conclusion

To enable high speed high resolution imaging as well as higher mode and higher harmonics imaging, this chapter investigates the bandwidth and resolution limiting factors of the optical beam deflection method used in AFMs. As result several conclusions can be drawn.

As shown in Sec. 3.1.1, a CMRR of 40 dB is sufficient to suppress the common mode noise to less than 1% of the differential noise of the presented system. Therefore, while significantly suppressing common mode noise, a bandwidth limitation by instrumentation amplifiers is avoided by using standard differential amplifiers.

As discussed in Sec. 3.1.2, the bandwidth limiting signal normalization should be avoided as the expected reduction of noise can be neglected. Additionally a change in the deflection readout gain can be adapted upfront. It is usually not necessary to normalize the signal at the same bandwidth as the deflection is measured as a major changes in the total irradiation are expected only at discrete events for example if the cantilever is changed.

For the TIA a small junction capacitance of the QPD is necessary to gain the maximum possible bandwidth. In general the selection of a QPD with a small active area leads to a small junction capacitance. However, to get at least 91% of the maximum possible sensitivity the width of active area of the QPD should be greater or equal to the spot diameter ( $2w_0 = 4\sigma$ ). Additionally biasing the QPD in the photoconductive mode further reduces the junction capacitance.

To avoid a drop of more than 20% of the maximum equal sensitivity for both, the

### *3 High bandwidth deflection readout*

vertical and horizontal sensitivity, simulation shows that the spot size on the detector should be at least 10 times the gap width [62]. Measurements in contrast have shown that the influence of the gap is less than expected from calculations. Further investigations will help to figure out why the gap leads to a significant output current.

It is shown in Sec. 3.3, that systematically selecting and matching the components of the deflection readout leads to a  $-3$  dB bandwidth of 64.5 MHz what is more than three times the fastest deflection readout bandwidth reported in literature so far [29].

---

## Crosstalk reduction by an optical design approach <sup>1</sup>

---

In most AFM applications the highly nonlinear tip-sample interaction force is held constant via feedback operation [8] in order to avoid damage to the tip and the sample and to obtain reliable measurement data. The output of the feedback controller corresponds to the displacement required to maintain a constant imaging force, thereby converting the force measurement into a displacement measurement with well known characteristics. The feedback controls the interaction by varying the vertical tip-sample distance by displacing the sample, the cantilever, or both (e.g. [8][47][48]). The benefit of displacing the cantilever instead of the sample is the almost constant system dynamic as the mass variation of different cantilevers is small compared to the effective mass of the actuator including the cantilever holder.

If the interacting force is held constant by displacing the cantilever, as done in moving-z and scanning lever AFMs, the relative position of the cantilever with respect to the QPD changes. This may lead to a false deflection signal resulting in undesired force variations. In Section 4.1 the influence of the crosstalk in the optical deflection measurement system is discussed in detail and a method to reduce the crosstalk is presented in Section 4.2. In Section 4.3 the proposed method is validated by measurements.

### 4.1 Crosstalk

Fig. 4.1 shows that a compensating movement of the cantilever involves a parallel shift of the laser lever, leading to a false deflection signal at the QPD. As the feedback compensates the misinterpreted part of the deflection signal too, the tip sample interaction force varies.

The displacement  $\Delta d$  due to the compensating cantilever movement  $\Delta z_{comp}$  is

---

<sup>1</sup>Parts of this chapter have been previously published in [60] and [66].

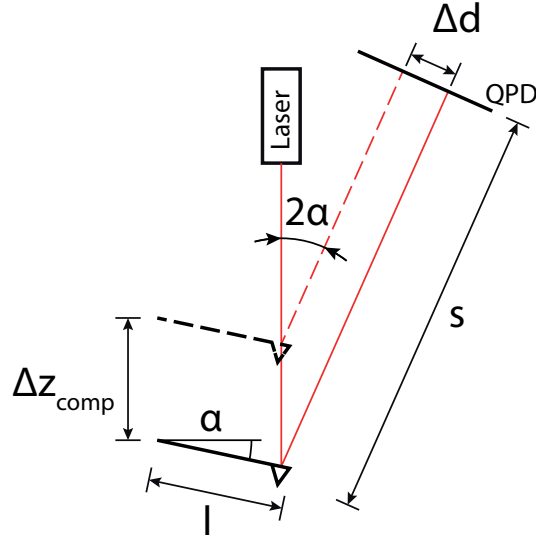


Figure 4.1: Crosstalk between the z-actuation and the deflection at the quadrant photo detector (QPD). As the cantilever moves by  $\Delta z_{comp}$ , it causes an unwanted deflection  $\Delta d$  on the QPD.

expressed by

$$\Delta d(\Delta z_{comp}) = \Delta z_{comp} \cdot \sin(2\alpha). \quad (4.1)$$

with the incident beam tilted by an angle  $\alpha$  to the normal axis of the cantilever. For a common AFM with an incidence angle  $\alpha$  of  $12^\circ$  the deflection  $\Delta d$  on the QPD is about 40 % of the compensating cantilever movement  $\Delta z_{comp}$ .

With the assumptions from [5] the static deflection  $\Delta z_{defl}$  of the free end of the cantilever causes a deflection

$$\Delta d(\Delta z_{defl}) = 3 \frac{s}{l} \cdot \Delta z_{defl} \quad (4.2)$$

on the QPD, where  $l$  is the cantilever length and  $s$  is the distance between the cantilever and the QPD. Combining Eq. 4.2 and 4.1 gives the equivalent cantilever deflection

$$\Delta z_{defl} = \frac{l \cdot \sin(2\alpha)}{3s} \Delta z_{comp} \quad (4.3)$$

as a function of the compensating cantilever movement  $\Delta z_{comp}$ . For a cantilever of length  $l = 200 \mu\text{m}$  and a distance  $s = 30 \text{ mm}$  between the cantilever and the QPD the crosstalk  $\Delta z_{defl}/\Delta z_{comp}$  following Eq. 4.3 is  $10^{-3}$ . Therefore a compensating movement of  $1 \mu\text{m}$  leads to a false deflection of  $1 \text{ nm}$  resulting in a force variation of  $10^{-9} \text{ N}$  for a cantilever with a stiffness of  $1 \text{ N/m}$ , what changes the pressure on a tip with a radius of  $1 \text{ nm}$  by approximately  $0.32 \text{ GPa}$ .

Compensating the crosstalk by extending the feedback controller is hardly feasible as the actual crosstalk varies with the size and shape of the cantilever and furthermore it depends on the position of the laser spot on the cantilever. To overcome these

limitations, a novel design to compensate the crosstalk by an additional focusing lens in the optical path is presented in Sec. 4.2. Next to the compensation of the crosstalk, the additional focusing lens gives the design freedom to adjust the laser spot size on the QPD, independent of the divergence of the beam and the distance  $s$  between the cantilever and the QPD. Without loss of other design freedoms the additional focusing lens allows the adjustment of the laser spot size with respect to the geometry of the QPD as discussed in Chapter 3.

## 4.2 Compensation of the crosstalk

As the origin of the crosstalk is a parallel shift of the laser lever, the basic property of an ideal lens, that it is focusing parallel rays to a single point in the focal plane, can be utilized to compensate for the crosstalk. Fig. 4.2a shows the additional convex lens in the optical path with the QPD in the focal plane. Furthermore Fig. 4.2b shows that a change in the tilt of the cantilever still leads to a deflection on the QPD while the parallel shift due to the compensation movement of the cantilever is no more visible on the QPD.

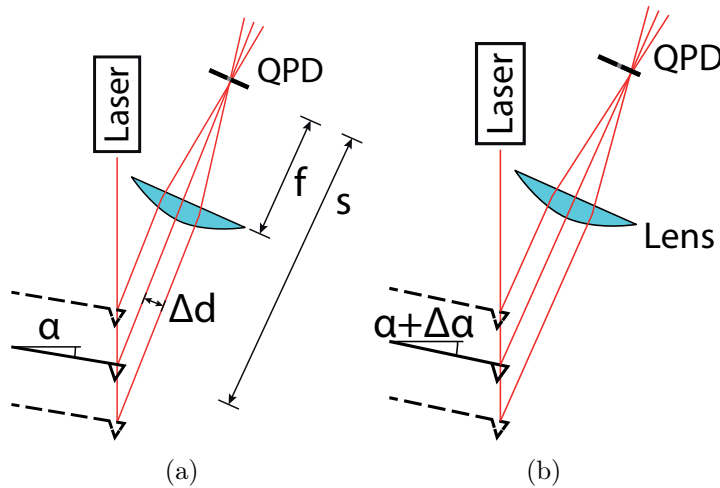


Figure 4.2: Additional lens in the optical path to reduce the crosstalk between the z-actuation and the deflection readout.

## 4.3 Measurements

To evaluate the crosstalk reduction capability of the additional lens in the optical path of an AFM, the test setup shown in Fig. 4.3 is used. The test setup consists of a laser source, mounted on a piezoelectrically actuated linear stage to perform a parallel shift of the laser beam, and a focusing lens mounted on a linear stage to adjust the focal plane onto the QPD. The laser source combines a laser diode S6305MG (Roithner Lasertechnik GmbH, Vienna, Austria) with a collimator GS8020A (Roithner Lasertechnik GmbH, Vienna, Austria) fixed in a temperature controlled mount TCLDM9 (Thor-

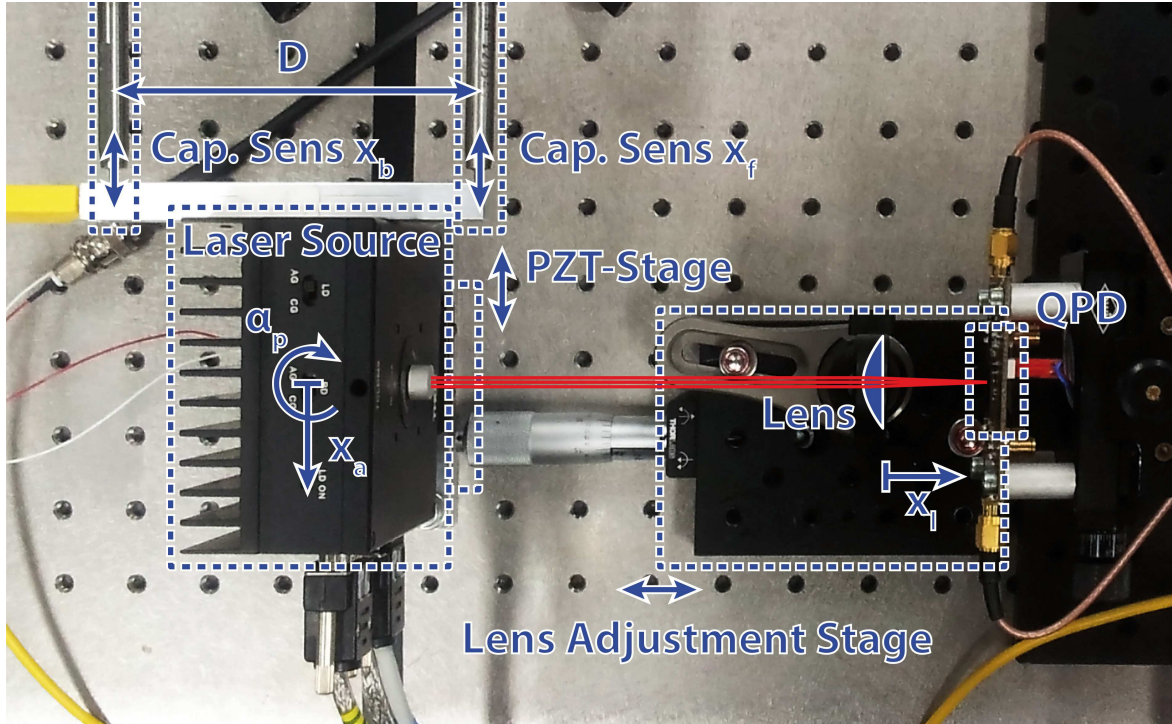


Figure 4.3: Test setup consists of a laser source mounted on a linear stage to measure the sensitivity of the QPD to a parallel shift of the laser beam going through a focusing lens.

labs, Inc., Newton, US-NJ) and a custom made aperture stop of 1.2 mm. The laser source is driven by the laser diode controller LDC501 (Stanford Research Systems, Inc., Sunnyvale, US-CA). As the mass and size of the focusing lens is not critical for the demonstration of the crosstalk reduction capability, a best form lens LBF254-040-A (Thorlabs, Inc., Newton, US-NJ) is used to focus the laser beam onto the QPD. The deflection signal is generated by subtracting the two output signals of transimpedance amplifiers connected to adjacent quadrants of the QPD and amplifying them by a low-noise preamplifier SR560 (Stanford Research Systems, Inc., Sunnyvale, US-CA).

To test the crosstalk reduction capability the laser source is moved by the linear stage with a 4 Hz sinusoidal motion with an amplitude of  $4 \mu\text{m}$  perpendicular to the laser axis, while recording the displacement signal of the QPD at 2 kSa/s with the oscilloscope DSOX4024A (Agilent, Santa Clara, US-CA).

The used linear stage is a manual stage with a stack piezo actuator clamped between the lead screw and the base. Due to an asymmetric design of the linear stage where the lead nut is mounted on one side instead of the center of the platform, the linear movement is superimposed by a parasitic tilt. To measure and incorporate the parasitic tilt two additional capacitive sensors MicroSense 6810 (MicroSense, LLC, Lowell, US-MA) are added at a distance  $D$  to measure the displacement  $x_f$  and  $x_b$  at the front and back end of the laser source. This allows the calculation of the parasitic tilt

$$\alpha_p = \arctan\left(\frac{x_f - x_b}{D}\right) \cdot \frac{180}{\pi} \quad (4.4)$$

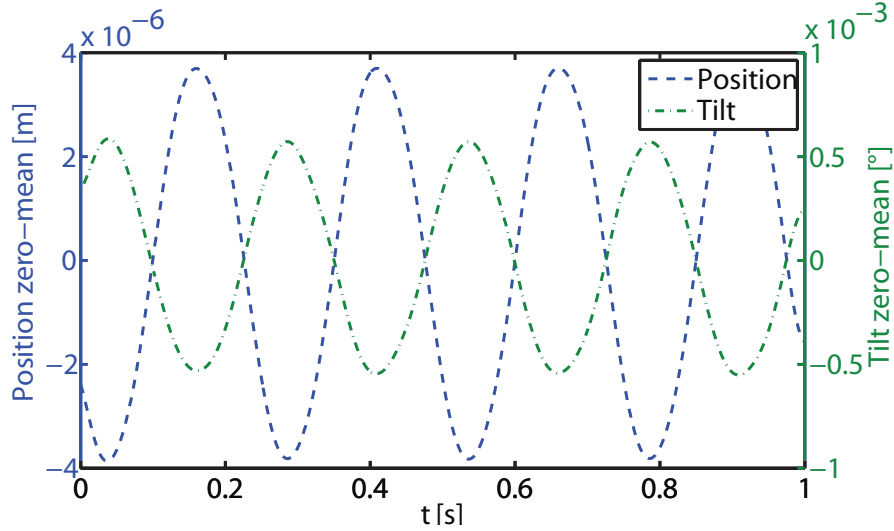


Figure 4.4: The average position (dashed) and tilt (dash dotted) of the laser source measured with the capacitive sensors and calculated with Eq. 4.4 and 4.5 while positioning the laser source perpendicular to the laser axis with 4 Hz.

in degree, and the average displacement

$$x_a = \frac{x_f + x_b}{2}. \quad (4.5)$$

Note that a slight translation along the laser axis can be neglected. Fig. 4.4 shows the average position (dashed) and tilt (dash dotted) calculated with Eq. 4.4 and 4.5 from the capacitive sensor values captured simultaneously to the deflection signal while actuating the laser source. It can be seen that the tilt is counteracting the parallel displacement of the laser source.

The measured deflection signal  $U_{defl}(t)$  can be modeled as a linear combination

$$U_{defl}(t) = \alpha_p(t)k_{tilt} + x_a(t)k_{shift} \quad (4.6)$$

with  $k_{tilt}$  and  $k_{shift}$  as the sensitivity to the tilt and the shift respectively. If  $\alpha_p(t) \neq cx_a(t) \forall c$  with  $c = \text{const.}$ ,  $k_{tilt}$  and  $k_{shift}$  can be found by fitting the model function  $U_{defl}(t)$  to the measurement data.

To measure the influence of the focusing lens position at the one hand and to find the correct focal distance to reduce the crosstalk on the other hand the focusing lens is spatially stepped along the laser axis with a step-size smaller than the Rayleigh length [63]

$$z_0 = \frac{4f^2\lambda}{\pi D_0^2}, \quad (4.7)$$

with the wavelength  $\lambda$ , the focal length  $f$  and the aperture diameter  $D_0$  as the Rayleigh length is a measure for the length of the beam waist of the Gaussian beam. With a wavelength  $\lambda = 630 \text{ nm}$ , a focal length  $f = 40 \text{ mm}$  and an aperture diameter  $D_0 = 2 \text{ mm}$

the Rayleigh length is calculated by Eq. 4.7 to  $320 \mu\text{m}$ . A step size of  $254 \mu\text{m}$  equal to the marks of the imperial scale of the micrometer screw on the manual linear translation stage is selected for the spatial sweep of the focusing lens.

Without a focusing lens between the laser source and the QPD the measurement and separation of the shift and tilt components leads to  $k_{shift} = 5.592 \cdot 10^4 \text{ V/m}$  and  $k_{tilt} = 2.042 \cdot 10^2 \text{ V/}^\circ$ , representing the sensitivity to a parallel shift and a tilt of the laser source respectively. As both parameters  $k_{shift}$  and  $k_{tilt}$  are of the same sign and the position and tilt values are of opposite sign (Fig. 4.4) the tilt is counteracting the parallel shift and therefore reducing the deflection signal at the QPD.

With the focusing lens at an exemplarily position Fig. 4.5 shows the signal of the QPD (solid line) as well as the shift (dashed) and tilt (dash dotted) components, separated by fitting the model in Eq. 4.6 to the measurement data resulting in  $k_{shift} = 3.163 \cdot 10^4 \text{ V/m}$  and  $k_{tilt} = 5.437 \cdot 10^4 \text{ V/}^\circ$ . As both parameters  $k_{shift}$  and  $k_{tilt}$  are of the same sign like without a focusing lens in the setup, the focusing lens must be closer to the QPD than the focal length. Otherwise the parallel movement would be inverted in the image plane by the focusing lens. The relative error of the model fit presented in Fig. 4.5 can be seen in Fig. 4.6.

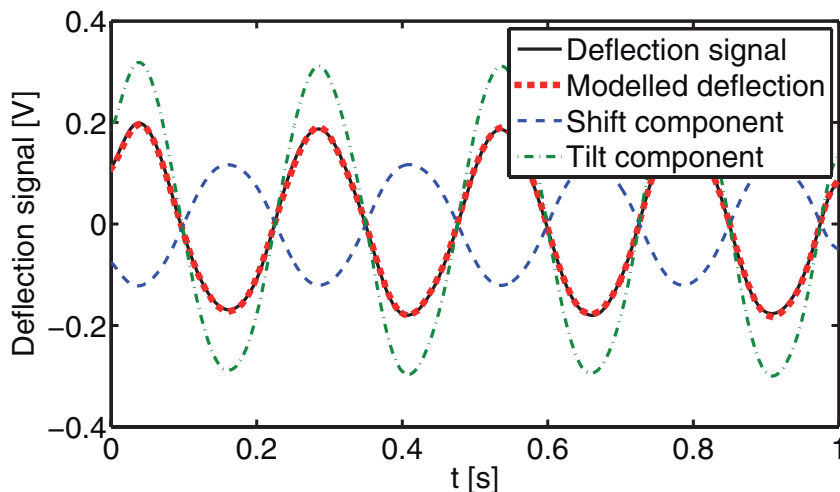


Figure 4.5: The deflection signal from the QPD (solid line) is shown at an exemplarily position of the focusing lens while actuating the laser source perpendicular to the laser axis. As result of the curve fitting process the deflection components caused by the shift and tilt of the laser source are shown dashed and dash dotted respectively as well as the sum of these signals (Eq. 4.6) with dots.

If the position of the focusing lens is adjusted so that the focal plane equals the plane of the QPD, the sensitivity is increased while the crosstalk between the parallel movement and the deflection on the QPD is minimized. Fig. 4.7 in comparison to Fig. 4.5 shows the deflection signal and its components with the focusing lens close to the optimum position. The deflection signal from the QPD (solid line) is increased by approximately 2.5 times and the crosstalk is reduced by 2 times compared to Fig. 4.5.

To get the influence of the position, the focusing lens is spatially stepped along

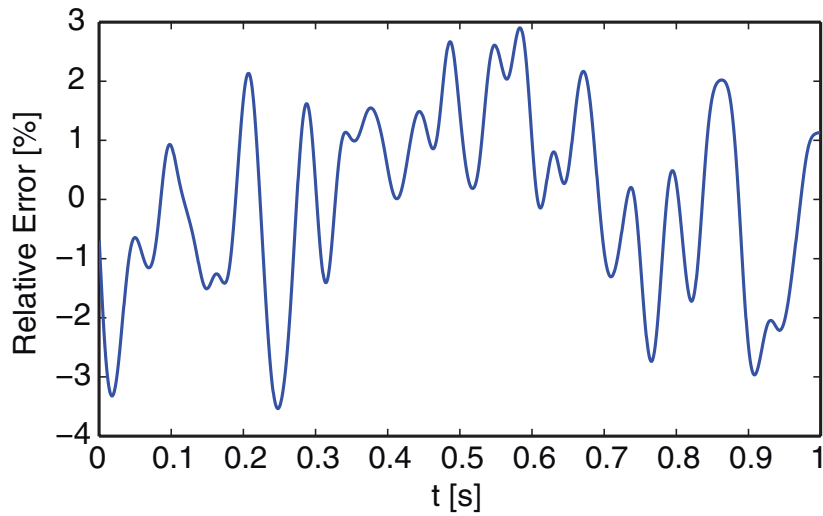


Figure 4.6: Relative error of the curve fitting result shown in Fig. 4.5.

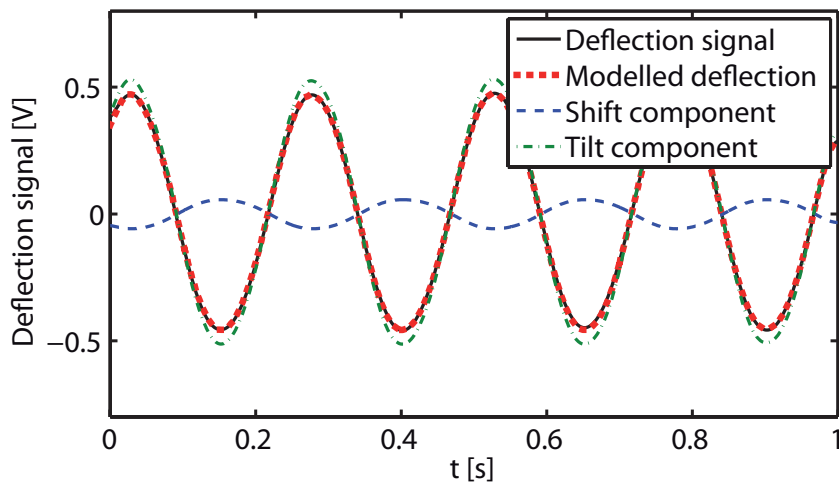


Figure 4.7: In comparison to Fig. 4.5 the focusing lens is adjusted to reduce the cross talk (shift component, dashed) and increase the sensitivity (tilt component, dash dotted). The deflection signal from the QPD (solid line) is increased by approximately 2.5 times and the crosstalk is reduced by 2 times as compared to Fig. 4.5

the laser axis with the step-size of  $254\ \mu\text{m}$ . In Fig. 4.8 the values of  $k_{shift}$  and  $k_{tilt}$  are plotted with respect to the position of the focusing lens. To show the repeatability and long term stability the five spatial sweeps of the focusing lens shown in Fig. 4.8 are performed on different days acquiring five times 64 records showing similar results.

Without a focusing lens the values of  $k_{shift} = 56\ \text{mV}/\mu\text{m}$  and  $k_{tilt} = 204\ \text{V}/^\circ$  are shown by the dashed lines. As mentioned before, if the focal plane gets in front of the QPD, a parallel movement is inverted by the lens and the sign of  $k_{shift}$  changes. For a lens displacement between  $-10\ \text{mm}$  and  $-5\ \text{mm}$ , the value of  $k_{tilt}$  drops below the value of  $204\ \text{V}/^\circ$  for the setup without the focusing lens as the beam diameter on the QPD exceeds the diameter of the almost parallel input beam. It can be seen that there is an optimal position for the focusing lens where the crosstalk is minimized by adding a focusing lens in the optical path of an AFM. Furthermore the sensitivity is enhanced by more than 5 times for the same position where the crosstalk is minimized. Critical issues are the selection of a suitable lens with low spherical aberration and the adjustment of the distance between the lens and the photo detector. It has to be mentioned that the sensitivity increases only for the special case of a collimated beam, as the sensitivity is diffraction limited for a diverging beam [67]. However, as shown in the following, the single lens is capable of compensating the crosstalk even for a diverging beam.

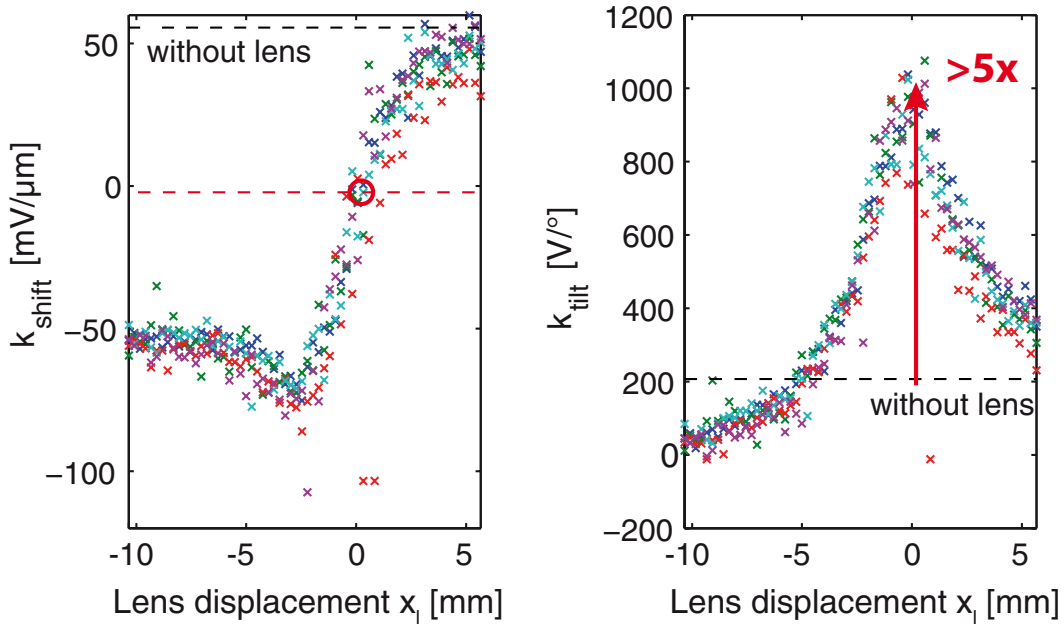


Figure 4.8: Measurement results for the crosstalk and the sensitivity with respect to the position of the focusing lens.

## 4.4 Diffraction limited sensitivity

Although the deflection of the laser spot is proportional to  $s$  (geometrical amplification) the measured deflection signal depends on the spot size of the laser beam on the QPD

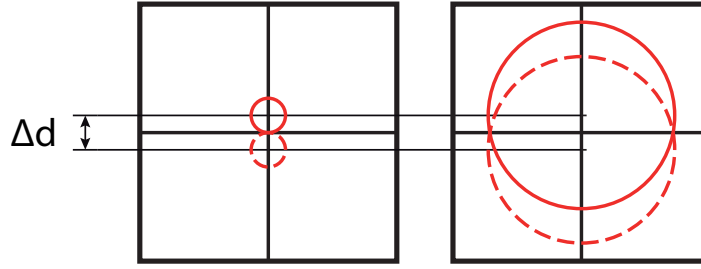


Figure 4.9: The same displacement  $\Delta d$  of a laser spot on the QPD leads to a different deflection signal depending on the spot size. The smaller spot on the left side causes a full scale step of the output signal while the same displacement of the bigger spot causes a much smaller variation in the output signal.

too. Fig. 4.9 shows that the same displacement  $\Delta d$  of a laser spot on the QPD leads to a different deflection signal depending on the spot size. The measured deflection signal increases as the laser spot diameter on the QPD decreases because the output signal of the QPD is proportional to the total irradiation and independent of the spatial distribution on the certain quadrant. Therefore the centroid on the quadrant does not affect the measured signal. The smaller spot on the left side of Fig. 4.9 causes a full scale step of the output signal, while the same displacement of the bigger spot causes a much smaller variation in the output signal, i.e. the spot size is inverse proportional to the sensitivity.

The demand for a small spot diameter on the cantilever in the order of the cantilever width ( $\lesssim 30 \mu\text{m}$ ) leads to a Rayleigh length much longer than the minimal possible optical path length in common designs [67]. Therefore the laser is focused on the back of the cantilever while the beam is diverging with an increasing distance to the cantilever. If the distance between the cantilever and the QPD increases, both the diameter and the deflection of the laser spot on the QPD increase. As the sensitivity is proportional to the distance and inverse proportional to the spot size, the sensitivity to the angular deflection stays constant, what is called the diffraction limited case [67]. Adding an additional lens between the cantilever and the QPD will not increase the deflection readout sensitivity for a beam focused on the cantilever as focusing again also reduces the deflection on the QPD.

## 4.5 The effect of an additional focusing lens on a diverging beam

For a collimated beam, Sec. 4.2 successfully shows the basic principle of compensating the crosstalk between the compensating cantilever movement and the deflection readout by an additional lens in the optical path. This section analyzes the crosstalk reduction capability for a diverging beam.

As discussed in Chapter 3 a small junction capacitance of the QPD is necessary to gain the maximum possible deflection readout bandwidth. The junction capacitance of the QPD can be reduced by selecting a QPD with a small active area. By using a QPD with a small active area care has been taken about the spot size on the QPD, as

the spot size should not exceed the size one active element to get at least 95 % of the maximum possible sensitivity.

The spot size on the QPD depends on the divergence of the beam and the distance between the cantilever and the QPD. To get a small spot size the QPD has to be arranged in close proximity to the cantilever. Although a short distance between the cantilever and the QPD keeps the amplification of noise due to structural rotational vibrations at a minimum, the interference noise increases due to the spatial coherence. Furthermore the size and arrangement of the single components of the deflection readout limits the minimum distance between the cantilever and the QPD.

The main idea to overcome these limitations is an additional lens as shown in Fig. 4.10 that gives the design freedom to change the spot size according to the geometry of the QPD, independent of the divergence  $\theta$  and the distance between the cantilever and the QPD. Furthermore, this novel approach compensates the crosstalk between the compensating movement  $\Delta z_{comp}$  and the deflection readout if the QPD is placed at the focal plane of the lens. As shown in Fig. 4.11 the deflection  $\Delta d$  on the QPD is preserved by the additional lens.

#### 4.5.1 The spot size on the QPD

With the object distance  $s_1$  between the cantilever and the lens, the beam diameter at the lens is calculated by

$$d_{lens} = 2s_1 \tan(\theta). \quad (4.8)$$

Using the thin lens approximation the object distance  $s_1$ , the image distance  $s_2$ , and the focal length  $f_c$  are related by the Gaussian lens formula [63]

$$\frac{1}{s_1} + \frac{1}{s_2} = \frac{1}{f_c}. \quad (4.9)$$

With the image distance  $s_2$ , the spot diameter at the QPD is calculated by

$$d_{QPD} = (s_2 - f_c) \frac{d_{lens}}{s_2}. \quad (4.10)$$

Combining Eq. 4.9 and Eq. 4.10 leads to the spot diameter at the QPD

$$d_{QPD} = 2f_c \tan(\theta), \quad (4.11)$$

that is independent of the distance between the cantilever and the focusing lens. For a given divergence  $\theta$ , the spot diameter on the QPD can be adjusted by the selection of a focusing lens with the appropriate focal length

$$f_c = \frac{d_{QPD}}{2 \tan(\theta)}. \quad (4.12)$$

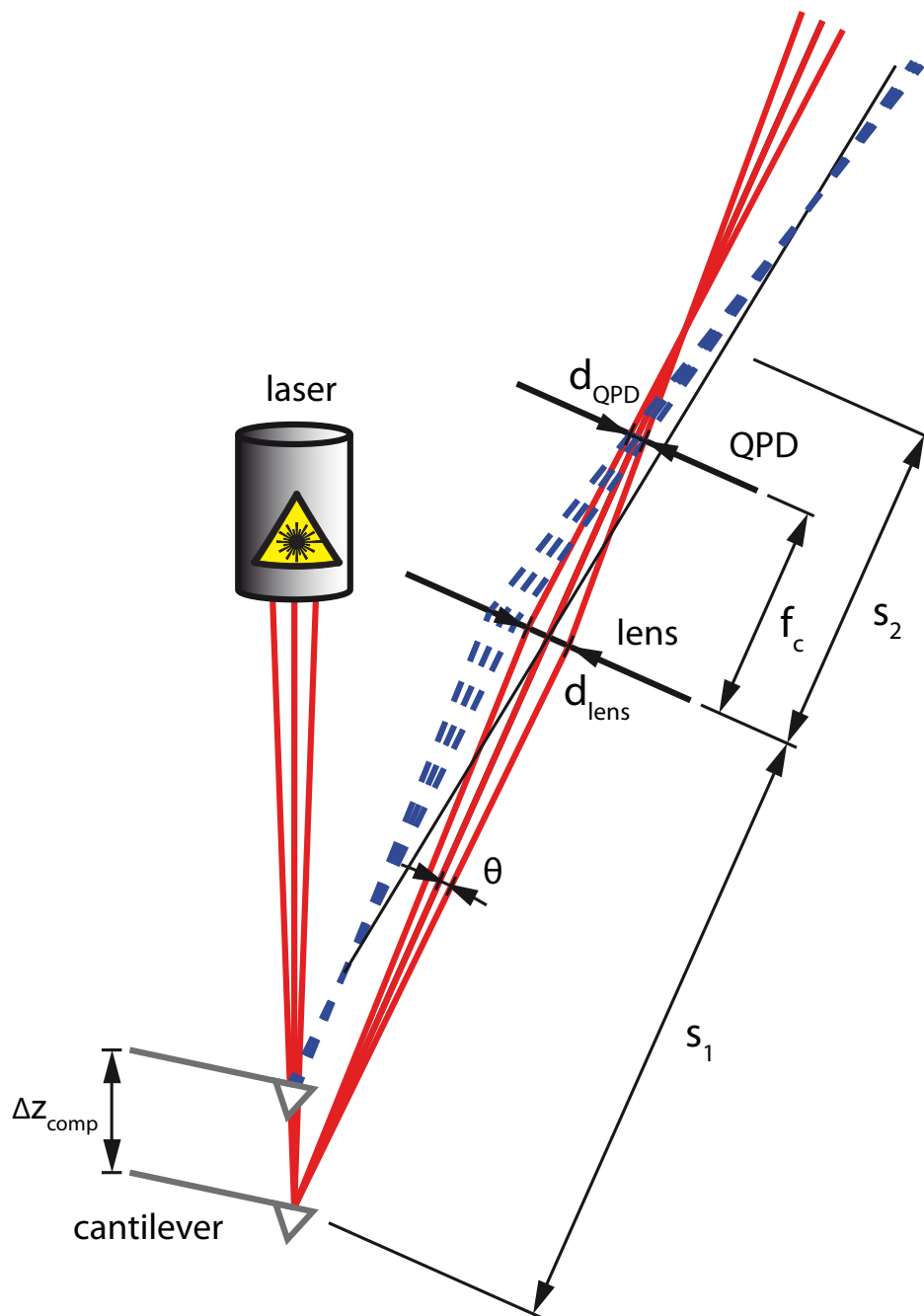


Figure 4.10: An additional lens with a focal length  $f_c$  focuses the reflected laser beam to the QPD that is placed at the focal plane of the lens. The laser beam is shown for the lower (solid red) and upper (dashed blue) position of the cantilever. The black line is used as a construction line passing through the optical center of the lens. The crosstalk between the compensating movement  $\Delta z_{\text{comp}}$  and the deflection readout is compensated by the lens. The spot size as well as the center position on the QPD is not affected by the compensating movement  $\Delta z_{\text{comp}}$ .



### 4.5.2 Compensation of the crosstalk

According to Fig. 4.11, a compensating movement  $\Delta z_{comp}$  changes the distance  $s_0$  between the laser source and the cantilever to

$$s'_0 = s_0 - \Delta z_{comp}, \quad (4.13)$$

and the distance between the cantilever and the focusing lens to

$$s'_1 = s_1 - \Delta z_{comp} \cos(2(\alpha + \Delta\alpha)), \quad (4.14)$$

where  $\Delta\alpha$  denotes the angular deflection of the cantilever. Additionally the compensating movement causes a shift of the rays perpendicular to the optical axis by

$$\delta_{\perp} = \Delta z_{comp} \sin(2(\alpha + \Delta\alpha)). \quad (4.15)$$

The initial beam starting at the laser source is defined by [63]

$$R_i = \begin{bmatrix} y_i \\ \theta_{y_i} \end{bmatrix} = \begin{bmatrix} s_0 \theta_m \\ \theta_m \end{bmatrix} \quad \text{with} \quad \theta_m \in (-\theta, \theta) \quad (4.16)$$

where rays at a distance  $y_i$  from the optical axis traveling with a an angle  $\theta_{y_i}$  with respect to the optical axis.

The ray at the cantilever is given by

$$R_c = M_{ci} R_i \quad (4.17)$$

with the transfer matrix [63]

$$M_{ci} = \begin{bmatrix} 1 & s'_0 \\ 0 & 1 \end{bmatrix}, \quad (4.18)$$

representing the path between the laser source and the cantilever. For simplification it is assumed that the beam deflection is uniform to all rays. Then the shifted and deflected beam can be represented by

$$R'_c = R_c + \begin{bmatrix} \delta_{\perp} \\ 2\Delta\alpha \end{bmatrix}. \quad (4.19)$$

The path between the cantilever and the detector is represented by the transfer matrix [63]

$$M_{dc} = \begin{bmatrix} 1 & f_c \\ 0 & 1 \end{bmatrix} \begin{bmatrix} 1 & 0 \\ -\frac{1}{f_c} & 1 \end{bmatrix} \begin{bmatrix} 1 & s'_1 \\ 0 & 1 \end{bmatrix} = \begin{bmatrix} 0 & f_c \\ -\frac{1}{f_c} & 1 - \frac{s'_1}{f_c} \end{bmatrix} \quad (4.20)$$

Finally the beam at the detector is obtained by

$$R_d = \begin{bmatrix} y_d \\ \theta_{y_d} \end{bmatrix} = M_{dc} M_{ci} R_i + M_{dc} \begin{bmatrix} \delta_{\perp} \\ 2\Delta\alpha \end{bmatrix}. \quad (4.21)$$

Using Eq. 4.21, the distance of the rays  $y_d$  from the optical axis at the plane of the

QPD are given as

$$y_d = \underbrace{\theta_m f_c}_{\approx \frac{d_{QPD}}{2}} + \underbrace{2\Delta\alpha f_c}_{\approx \Delta d}. \quad (4.22)$$

Eq. 4.22 shows that the laser spot on the QPD is only displaced by an angular deflection  $\Delta\alpha$  and not affected by the compensating movement  $\Delta z_{comp}$ . Therefore it is shown that the novel approach of adding an additional focusing lens to the optical path, compensates the crosstalk between the compensating movement  $\Delta z_{comp}$  and the deflection readout, if the QPD is placed at the focal plane of the lens.

## 4.6 Conclusion

This chapter describes an optical design approach to compensate for the crosstalk between the z-actuation and the deflection readout in moving-z and scanning lever AFMs. If the controller compensates the false deflection due to the crosstalk the force between the tip and the sample varies. An additional focusing lens between the cantilever and the QPD can compensate for the crosstalk and furthermore gives an additional design freedom for the spot size on the cantilever. Even for a laser beam focused on the cantilever, the additional focusing lens enables the utilization of a small QPD with a low junction capacitance for a high deflection readout bandwidth, independent of the required spot size on the cantilever and the minimum distance between the cantilever and the QPD.

---

## Scanning Lever AFM Design

---

As discussed in Sec. 2.1, there are different possibilities to scan the sample on the one hand (x/y-movement) and to compensate the deflection of the cantilever on the other hand (z-movement). To get rid of sample size and sample mass limitations the scanning lever system as shown in Fig. 2.1c actuates the cantilever in x-, y-, and z-direction. Although the sample is static, care has to be taken about the deflection readout. The laser spot has to track the moving cantilever as well as the crosstalk between the moving cantilever and the photodetector has to be considered. For the straight forward approach to scan all components including the alignment mechanism [14], the structural dynamics of the interconnected parts have to be considered when increasing the scan speed, as the fast scanning motion may excite resonances.

In order to avoid scanning of the laser source, the focusing optics, the detector, and the alignment mechanisms, an additional tracking mechanism as shown in Fig. 5.1 is necessary to keep the laser spot on the moving cantilever. Additionally a compensation mechanism is necessary to prevent crosstalk between the x/y/z-movement of the cantilever and the deflection measurement on the QPD.

### 5.1 The design of the optical path

With a fixed laser source and alignment mechanism, tracking of the cantilever has to be done by moving an additional optical assembly [15] to redirect the laser beam according to the cantilever movement. In general redirecting can be done by tilting or shifting the beam. If the beam is redirected by a tilt, the angles of incidence and reflection on the following mirrors are changed. This leads to a more complex design as the angular variations have to be compensated to avoid crosstalk between the tracking mechanism and the deflection measurement on the QPD. Shifting the beam in combination with plane mirrors results in a less complex design as there are no angular variations in the optical path.

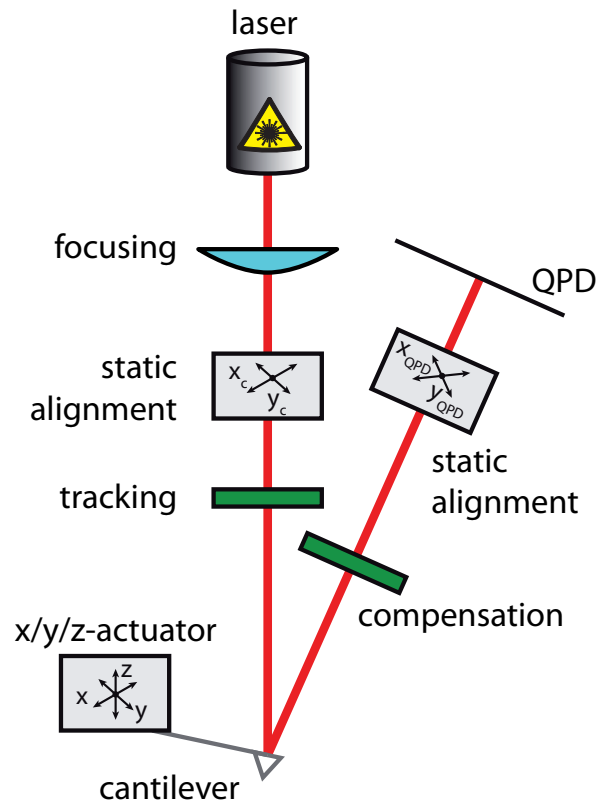


Figure 5.1: Optical beam deflection method for a scanning lever AFM. In order to avoid scanning of the laser source, the focusing optics, the detector, and the alignment mechanisms, an additional tracking mechanism is used to keep the laser spot on the moving cantilever. A compensation mechanism to prevent crosstalk between the cantilever movement and the deflection measurement on the QPD is necessary, too.

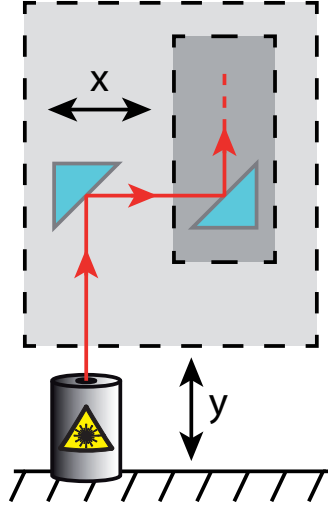


Figure 5.2: Idea of moving along the incident beam in a multidimensional design. The optical assembly to redirect the laser beam according to the cantilever movement is splitted similar to the actuators in serial design.

### 5.1.1 Folding the optical path

If the angles in the optical path are fixed, the main idea to avoid crosstalk between the scanning motion and the deflection readout is to move along the beam without changing the center of incidence. For a multidimensional design Fig.5.2 shows how to fold the beam that each stage moves along the incident beam. The optical assembly, used to redirect the laser beam according to the cantilever movement, is splitted similar to the actuators in the serial design. Each stage has to move along the incident beam as well as redirecting the beam to the desired actuation direction of the following nested stage. Therefore in a multidimensional design the optical path is folded according to the serial design of the actuator.

Moving along a diverging beam the beam diameter changes. Assuming a Gaussian beam, the half-width  $w(z)$  at a distance  $z$  from the beam waist of half-width  $w_0$  is [63]

$$w(z) = w_0 \cdot \sqrt{1 + \left(\frac{\lambda z}{\pi w_0^2}\right)^2} \quad (5.1)$$

for a wavelength  $\lambda$ . If the beam is focused on the cantilever a total variation of the path length equal to the Rayleigh length [63]

$$z_0 = \frac{\pi w_0^2}{\lambda} \quad (5.2)$$

doubles the cross-sectional area by increasing the beam diameter by a factor of  $\sqrt{2}$ . For example at a wavelength  $\lambda = 630 \text{ nm}$  a  $30 \mu\text{m}$  spot diameter at the focal plane leads to a Rayleigh length of  $1.122 \text{ mm}$ , much longer than the usual variation of the path length due to the scanning motion. An exemplary x/y-scan range of  $\pm 50 \mu\text{m}$  and a

z-actuation range of  $\pm 3 \mu\text{m}$  leads to maximum deviation of  $\pm 103 \mu\text{m}$  from the average path length. The displacement of  $\pm 103 \mu\text{m}$  from the focal plane increases the  $30 \mu\text{m}$  spot by 0.42 % to  $30.126 \mu\text{m}$  for  $\lambda = 630 \text{ nm}$ . Ususally the 0.42 % deviation of the spot size are neglectable.

### 5.1.2 Ray tracing

To design and analyze the optical path composed of several mirrors the following ray tracing algorithm is developed. A ray starts at its origin  $\vec{r}_0$  and points to the direction denoted by the unit vector  $\vec{u}_r$ . A plane mirror is represented by the unit normal vector  $\vec{u}_m$  and the normal distance  $d_m$  to the origin.

A ray intersecting at a distance  $l_r$  from its origin with a mirror satisfies the Hesse normal form

$$(\vec{r}_0 + l_r \vec{u}_r) \cdot \vec{u}_m - d_m = 0. \quad (5.3)$$

Therefore the incident beam represented by  $r_{0,i}$  and  $u_{r,i}$  is reflected at

$$r_{0,r} = r_{0,i} + u_{r,i} \underbrace{\frac{d_m - r_{0,i} \cdot \vec{u}_m}{u_{r,i} \cdot \vec{u}_m}}_{l_r} \quad (5.4)$$

Using the Householder matrix [68] the direction of the reflected beam

$$u_{r,r} = [I - 2u_m \cdot u_m^T] \cdot u_{r,i} \quad (5.5)$$

with the identity matrix  $I$ . The presented algorithm is implemented in MATLAB including functions to visualize the optical path, as well as analyze the crosstalk between the scanning motion and the deflection on the QPD.

### 5.1.3 Folding the path according to a serial actuation configuration

Applying the presented idea of folding the optical path to the requirements of a scanning lever AFM a possible realization is shown in Fig.5.3. For a better visibility all visualizations of the optical path are done upside down with the cantilever tip pointing upwards. The design shows the arrangement of the laser source, the cantilever, the QPD, and four mirrors guiding the laser beam to and from the cantilever. Based on the serial design the mirrors A and D are scanned in the y-direction dedicated as the slow scan axis, while the mirrors B and C are scanned in both, the y-direction and the x-direction dedicated as the fast scan axis. The actuation direction of the mirrors is denoted in parentheses.

The laser source and the QPD including their alignment mechanisms are fixed. As they are not actuated, there size an mass are not influencing the achievable scan speed. The laser source is aligned in parallel to the slow scan axis (y) directing the laser beam to the mirror A, which folds the optical path by reflecting the beam in parallel to the fast scan axis (x). In a similar way the beam is reflected in z-direction towards the cantilever by the mirror B. The cantilever is mounted at an angle of  $12^\circ$

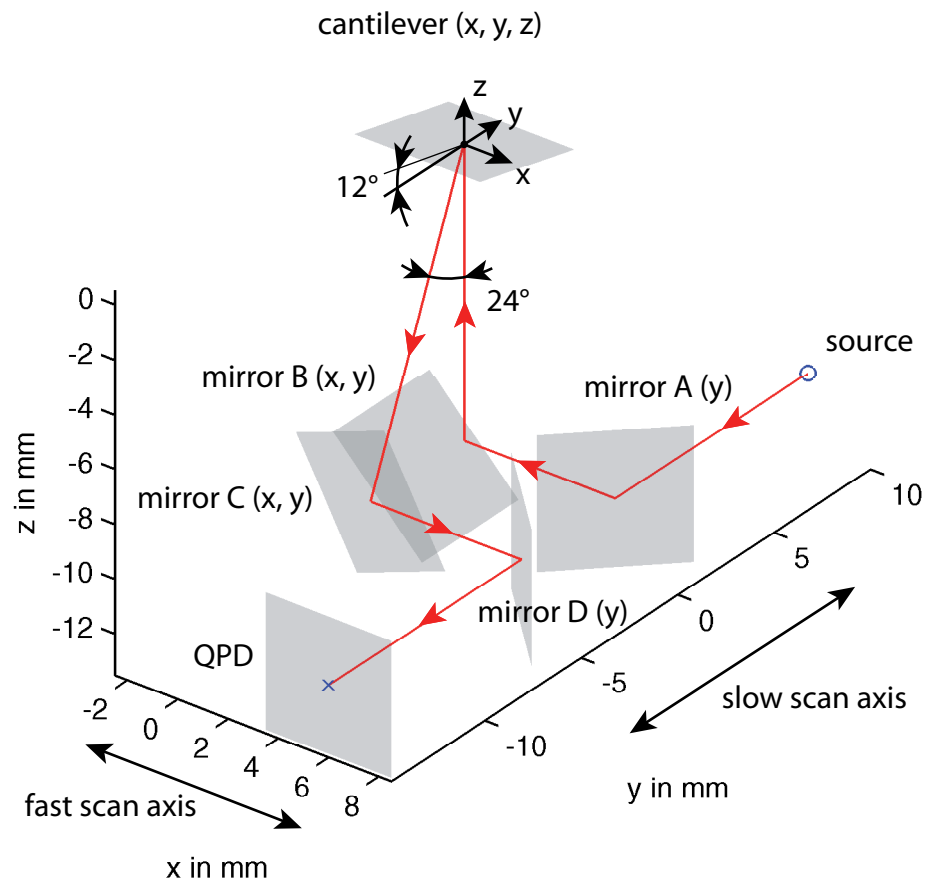


Figure 5.3: Folding the optical path according to a serial design of the scanning lever actuation. The actuation direction of the mirrors is denoted in parentheses.

with respect to the x/y-plane, reflecting the incident beam by  $24^\circ$  in parallel to the y/z-plane. With respect to mirror B, mirror C is rotated by  $24^\circ$  around the x-axis, reflecting the incident beam from the cantilever in parallel to the fast scan axis (x). Mirror D reflects the incident beam in parallel to the slow scan axis (y). Therefore the beams incident to and reflected from the individual stages are in parallel to the respective actuation direction.

### Deflection of the cantilever

The deflection of the cantilever is simulated by rotating the cantilever. The deflection of the beam due to a lateral and vertical deflection of the cantilever is shown in Fig. 5.4 by 20 steps between  $\pm 1^\circ$ . The resulting deflection of the laser spot on the QPD is shown in Fig. 5.5. Due to folding of the beam in the optical path the deflection direction on the optical path is rotated by  $66^\circ$  with respect to the orientation shown in Fig. 3.6. The rotation of the deflection direction is compensated by rotating the alignment stage of the QPD by the same  $66^\circ$ . The deflection of the laser spot on the QPD is equal to the case with without folding the optical path if the path length is the same.

### Crosstalk between the x/y-scanning motion and the deflection readout

The simulated actuation of the fast axis is shown in Fig. 5.6. For better visibility, a typical actuation range of  $\pm 50 \mu\text{m}$  is scaled by a factor of 10. Therefore the simulated actuation is  $10 \cdot \pm 50 \mu\text{m}$ . The mirrors B and C are actuated in fast scan direction, where mirror B keeps the beam on the cantilever and mirror C reflects the beam from the cantilever back in parallel to the fast scan direction. Therefore the actuation of the fast scan axis is not visible on the QPD, as long as the cantilever is not deflected.

The simulated actuation of the slow scan axis (y) is shown in Fig. 5.7. Again, as for the fast scan axis, the actuation is scaled by a factor of 10 for better visibility. Therefore the simulated actuation is  $10 \cdot \pm 50 \mu\text{m}$ . All the mirrors A, B, C, and D are actuated in the slow scan direction, with the mirror A moving along the incident beam from the static laser source and the mirror D moving along the beam reflected to the static QPD. Therefore the actuation of the slow scan axis is not visible on the QPD, as long as the cantilever is not deflected.

If the cantilever is deflected from its initial position, the optical path between the cantilever and the QPD is no more aligned to the respective actuation direction of the slow and fast scan axis. A cantilever deflection  $\alpha_{defl}$  leads to an angular misalignment of  $2 \cdot \alpha_{defl}$ . The path length from the cantilever to the QPD changes according to the actuation of the slow and fast scan axis. An actuation of  $\Delta x$  and  $\Delta y$  leads to a change in the path length from the cantilever to the QPD of  $\Delta d_{QPD,c} = \Delta x + \Delta y$ . For the realization shown in Fig. 5.3, with the QPD aligned normal to the incident beam, the crosstalk between the change in the path length  $\Delta d_{QPD,c}$  and the unwanted deflection  $\Delta d$  of the laser spot on the QPD is

$$\frac{\Delta d}{\Delta d_{QPD,c}} = \frac{\Delta d}{\Delta x + \Delta y} = \tan\left(2 \cdot \alpha_{defl} \cdot \frac{\pi}{180}\right) \quad (5.6)$$

with respect to the angular deflection  $\alpha_{defl}$  of the cantilever from its initial position. For

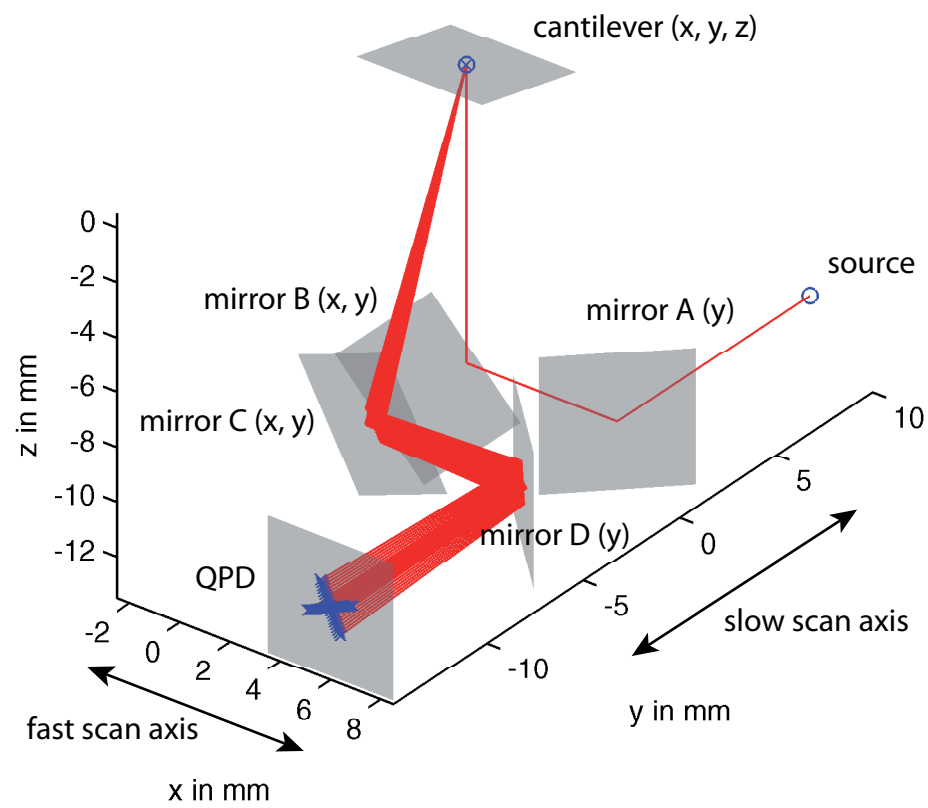


Figure 5.4: The arrangement of the mirrors for the scanning lever AFM with a simulated vertical and lateral cantilever deflection of  $\pm 1^\circ$ . The actuation direction of the mirrors is denoted in parentheses.

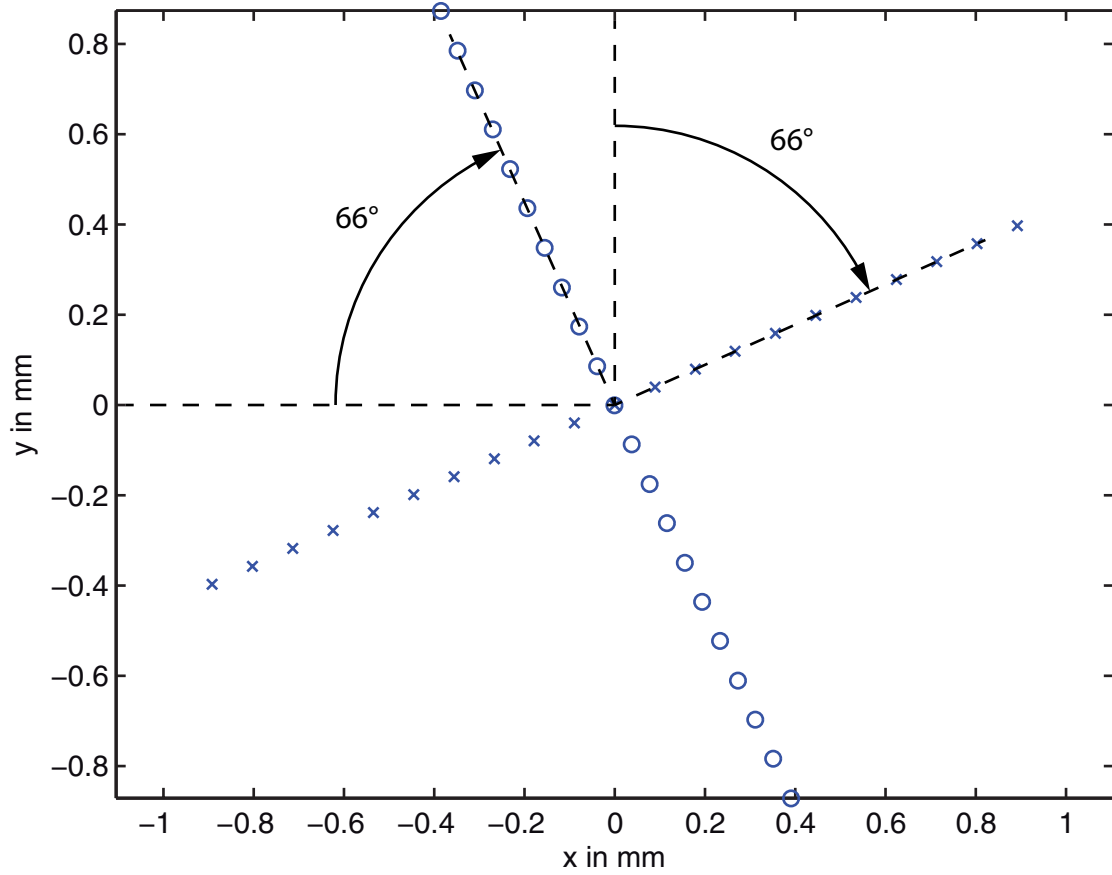


Figure 5.5: Deflection of the laser spot on the QPD shown in Fig. 5.4 for a simulated vertical ( $\times$ ) and lateral ( $\circ$ ) cantilever deflection of  $\pm 1^\circ$ .

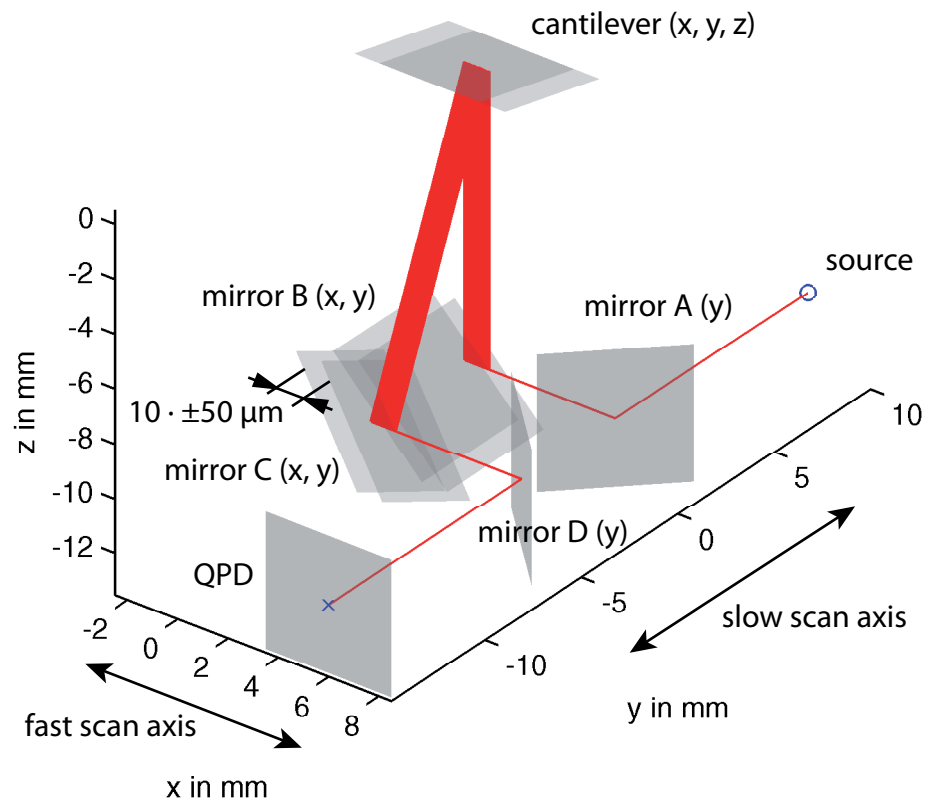


Figure 5.6: The arrangement of the mirrors for the scanning lever AFM with a simulated actuation of the fast axis. For better visibility, the actuation of  $\pm 50 \mu\text{m}$  is scaled to  $10 \cdot \pm 50 \mu\text{m}$ . The actuation direction of the mirrors is denoted in parentheses.

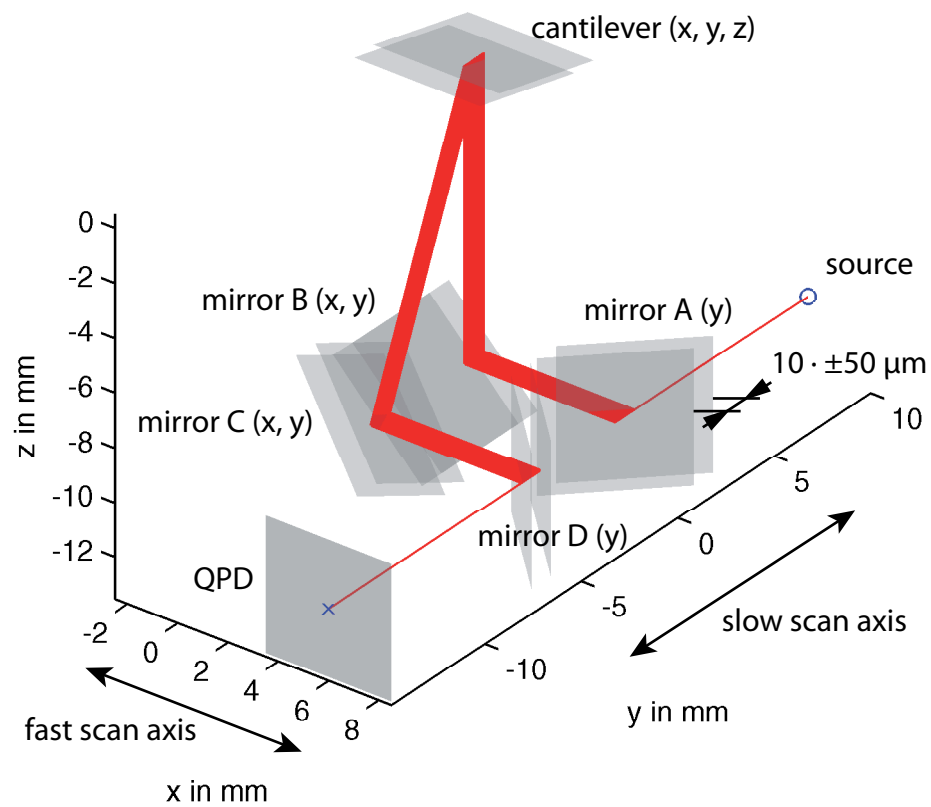


Figure 5.7: The arrangement of the mirrors for the scanning lever AFM with a simulated actuation of the slow scan axis. For better visibility, the actuation of  $\pm 50 \mu\text{m}$  is scaled to  $10 \cdot \pm 50 \mu\text{m}$ . The actuation direction of the mirrors is denoted in parentheses.

both, the actuation in the slow and fast scan direction, the direction of the unwanted deflection on the QPD is coincident with the deflection due to a vertical deflection of the cantilever. Therefore, if the cantilever is deflected of its initial position, the optical path is misaligned what leads to a crosstalk between the x/y-scanning motion and the vertical deflection signal.

If the cantilever is deflected by  $1^\circ$ , the resulting crosstalk between the  $10 \cdot \pm 50 \mu\text{m}$  actuation of the fast scan axis and the deflection of the laser spot on the QPD is shown in Fig. 5.8. The laser spot deviates by  $10 \cdot \pm 1.75 \mu\text{m}$  from its center point. Evaluating Eq. 5.6 with  $\alpha_{defl} = 1^\circ$ ,  $\Delta x = \pm 10 \cdot 50 \mu\text{m}$ , and  $\Delta y = 0$  gives the same result. Simulating the crosstalk between the slow scan axis and the deflection readout leads to the same result as shown for the fast scan axis (data not shown).

When imaging the crosstalk will lead to an image tilted along the diagonal axis. If the feedback compensates the misinterpreted part of the deflection signal, the tip sample interaction force varies. The crosstalk can be avoided by operating the cantilever at a setpoint with zero deflection, e.g. between the attractive and repulsive regime in Fig. 2.2. Another possibility would be the online correction of the deflection signal depending on the actual scanner position.

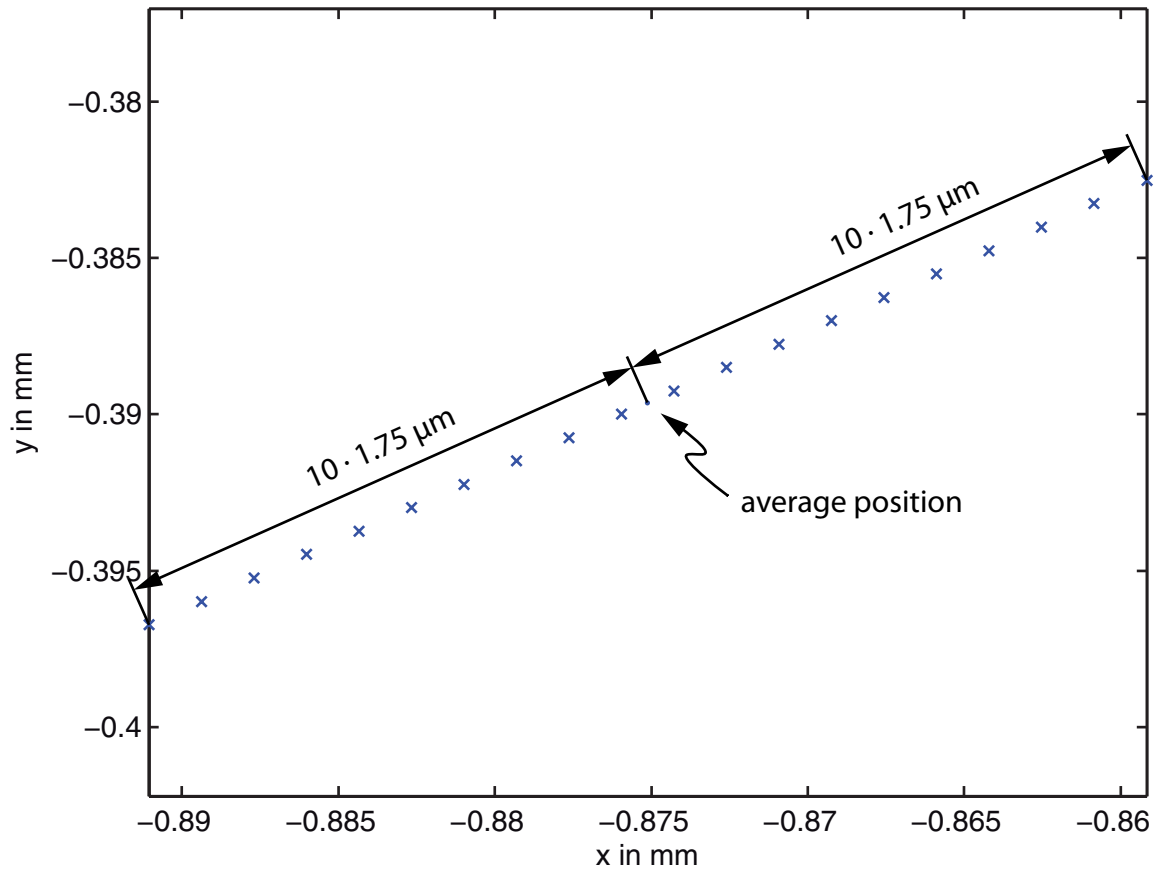


Figure 5.8: Crosstalk between the  $10 \cdot \pm 50 \mu\text{m}$  actuation of the fast scan axis and the unwanted deflection of the laser spot on the QPD due to a cantilever deflection of  $1^\circ$ . Simulating the crosstalk for the slow scan axis leads to the same amount and direction of the unwanted deflection on the QPD (data not shown).

## 5.2 Realization of the three dimensional scanner

The proposed method of folding the optical path according to the actuation directions requires a serial design, as the single actuators are not separated in a parallel design. The requirement of the positioning bandwidth differs for each actuation direction, with the highest required positioning bandwidth for the z-actuation and the lowest one for the slow scan axis [50]. Therefore a three dimensional nanopositioning stage consisting of three different actuators is designed. While this chapter mainly focuses on the mechanical design, the control and electronic components (e.g. the scan signal generation and the configuration of the high voltage amplifiers driving the stack piezos) are discussed in Chapter 5.

### 5.2.1 z-Scanner

The z-actuator requires the highest positioning bandwidth. To achieve a high positioning bandwidth a high first dominant mechanical resonance frequency is desired. Considering a single actuator with an intrinsic stiffness  $k$  and the moving mass  $m$  as a mass spring system the angular resonance frequency  $\omega_0 = \sqrt{k/m}$  [13]. Therefore a stiff design with a low moving mass is desired [50]. Next to the first dominant mechanical resonance frequency of the z-scanner itself, the total mass of the z-scanner has to be considered as it adds to the actuated mass of the x- and y-scanner. As the added mass of the z-scanner reduces the first mechanical resonance frequency of the x- and y-scanner, a low mass design with a minimum number of single components is desired. It has to be mentioned that the influence is much more significant on the x-scanner than on the y-scanner, as the mass of the z-scanner would be in the order of the moved mass of the x-scanner itself.

The essential components of the z-scanner are two mirrors guiding the beam to and from the cantilever (Sec. 5.1.3), the actuator itself, and a cantilever mount. As shown in Fig. 5.9, all components are mounted on a single aluminum base.

According to Sec. 5.1.3, deflecting the beam by  $90^\circ$  is done by right angle prism mirrors MRA05-P01 (Thorlabs, Inc., Newton, US-NJ). The prisms are made of NBK-7 with a silver coating protected by an  $\text{SiO}_2$  overcoat. Another possible way would be to mount plate mirrors on a sloped aluminum surface instead of using right angle prisms made of NBK-7. To compare the NBK-7 against aluminum in terms of structural dynamics, the Young's modulus  $E$  and the mass density  $\rho$  are of great importance [11]. Comparing these material properties, it is beneficial to use the right angle prism mirrors instead of plate mirrors on a sloped aluminum surface, as the mass density of the mirrors with  $2.51 \text{ g/cm}^3$  is lower than the mass density of aluminum with approximately  $2.7 \text{ g/cm}^3$  while the Young's modulus of 82 GPa is slightly higher than that of aluminum, which is around 70 GPa depending on the particular alloy.

As actuator a piezo ring stack actuator NAC2121-H08-A01 (Noliac, Kvistgaard, Denmark) with an outer diameter of 6 mm, an inner diameter of 2 mm and a length of 8 mm is used. The maximum stroke is  $9 \mu\text{m}$  at an operating voltage of 200 V. The capacitance is 280 nF.

For actuators that are long compared to their lateral dimension, the first mechanical resonance will be a bending mode, leading to in- and out-of-plane disturbances of

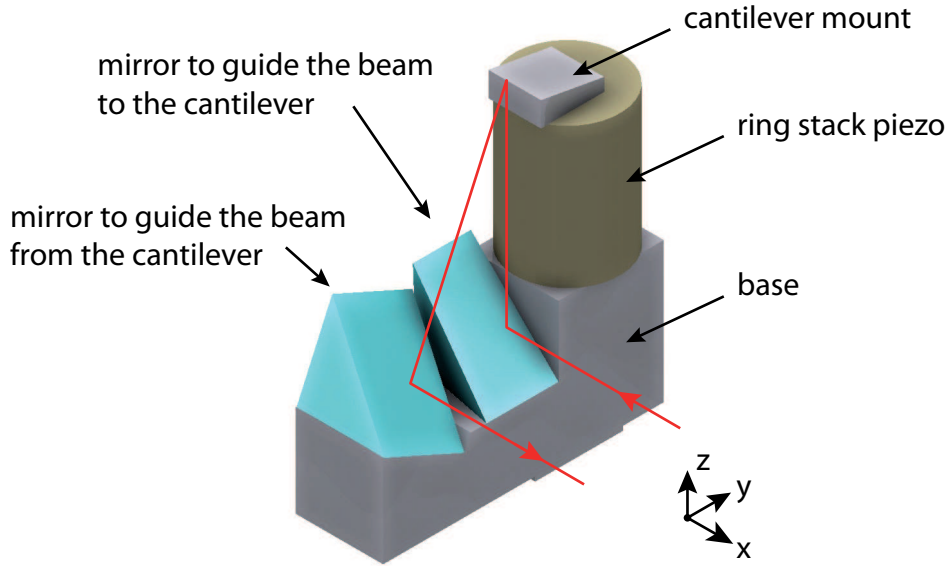


Figure 5.9: The z-scanner consisting of the aluminum base, the mirrors guiding the laser beam to and from the cantilever, and the cantilever mount on top of the ring stack piezo. The mirrors are arranged in a way that the incoming and outgoing laser beam is in parallel to the x-actuation of the aluminum base, independent of the z-actuation. This way cross talk between the x/z-actuation and the deflection readout is avoided.

the scanning motion [69]. Although the effects of the bending mode can be reduced by flexure guiding the actuator [69], the piezo is used without an additional guidance to reduce the overall mass of the z-scanner. Reducing the effect of the bending mode by increasing the lateral dimensions, will increase the mass and capacitance of the piezo stack actuator too. The idea to overcome these limitation is the utilization of a ring stack piezo instead of plate stack piezo.

Considering the actuator as a mass spring system the angular resonance frequency  $\omega_0 = \sqrt{k/m}$  [13] with the intrinsic stiffness  $k$  and the moving mass  $m$ . For a piezo fixed at one end the stiffness related to a bending force is [70]

$$k_{bend} = \frac{3EI}{l^3}, \quad (5.7)$$

with the Young's modulus  $E$ , the second moment of area  $I$ , and the length  $l$ . Therefore the ratio of the stiffness is equal to the ratio of the second moments of area. For the ring piezo the second moment of area is [70]

$$I_{ring} = \frac{\pi(D^4 - d^4)}{64}, \quad (5.8)$$

with the outer and inner diameter  $D$  and  $d$ , while for a square cross section with a side

length  $a$  the second moment of area is [70]

$$I_{square} = \frac{a^4}{12}. \quad (5.9)$$

For an equal second moment of area  $I_{square} = I_{ring}$ , the cross sectional area of the square piezo is

$$A_{square} = a^2 = \sqrt{\frac{12\pi(D^4 - d^4)}{64}}, \quad (5.10)$$

and the ratio of the cross sectional area  $A_{ring}$  for the ring piezo and  $A_{square}$  is

$$\frac{A_{ring}}{A_{square}} = \sqrt{\frac{\pi(D^2 - d^2)}{3(D^2 + d^2)}}. \quad (5.11)$$

Therefore using a ring piezo with an outer diameter of 6 mm and an inner diameter of 2 mm instead of a square piezo with the same resonance frequency, reduces the cross section, mass, and capacitance by 8.47%.

To tilt the normal axis of the cantilever by  $12^\circ$  with respect to the z-actuation direction, an aluminum wedge (identified as cantilever mount in Fig. 5.9) with an angle of  $12^\circ$  is mounted on top of the z-actuator. To keep the moved mass as low as possible, no clamping mechanism for the cantilever is integrated. Instead, the cantilever is mounted by fixing the cantilever chip with wax on the aluminum wedge.

The z-scanner with a total mass of 3.65 g is glued with cyanoacrylate adhesive via the extended surface on the bottom side of the aluminum base on the x-scanner.

### 5.2.2 x-Scanner

The x-direction is used as the dedicated fast scan axis. To allow high speed imaging a high speed scanner like the one shown in Fig. 2.7 [44] is favored. Although high speed scanning was successfully demonstrated [44], this scanner is not directly suitable for the intended design. As the optical path has to be folded according to each actuation direction a serial design and therefore a one dimensional actuator is needed. Additionally, as all nested actuators are moved by the outer ones the total mass of the nested actuators including the stators is critical. Therefore the high speed scanner from Fig. 2.7 has to be adapted to fit the intended design.

The one dimensional scanner shown in Fig. 5.10 is the modification of the three dimensional scanner shown in Fig. 2.7. The mounting holes of the y-actuating piezos are substituted by aluminum blocks stiffening the structure perpendicular to the x-actuation direction. The push pull design of the original actuator is changed to a push design to further reduce the total mass of the x-scanner, as that one is actuated by the y-scanner. Two piezo stack actuators NAC2013-H10-A01 (Noliac, Kvistgaard, Denmark) are mounted by clamping them with a preloading screw that pushes a steel plate against the end cap of the outer piezo.

The mass of the supporting structure made of steel is reduced from 706 g to 273 g by reducing the overall height as well as the height of the flex structure and by removing the material around the removed piezos (cf. Fig. 2.7 and Fig. 5.10). The total mass of

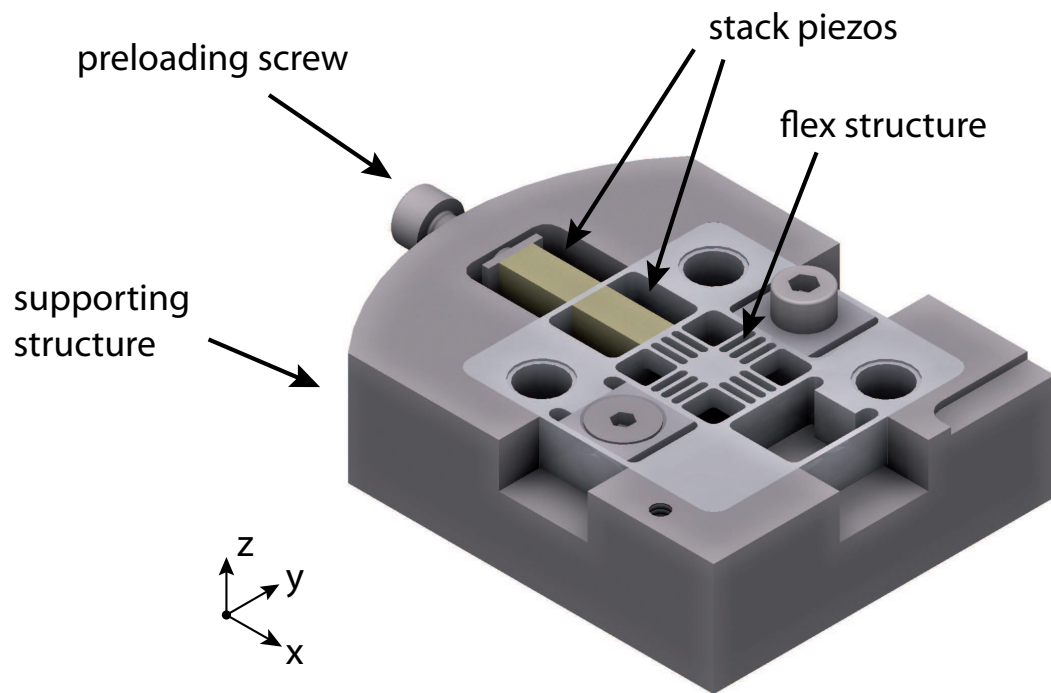


Figure 5.10: The x-scanner with an aluminum flex structure surrounded by the supporting frame made of steel. Two stack piezos are mounted by clamping them with a preloading screw that pushes a steel plate against the end cap of the outer piezo.

the x-scanner including the piezos is 298 g.

### 5.2.3 y-Scanner

The y-direction is used as the dedicated slow scan axis. The frequency of the triangular scan signal of the slow scan axis is equal to one half of the frame rate. For imaging frames with  $m$  lines at a line scan rate of  $f_{line}$  the actuation frequency of the slow scan axis  $f_{slow} = f_{line}/(2m)$  leading to a frame rate of  $f_{frame} = f_{line}/m$ . For example, requesting a line scan rate of 400 lines/s, the actuation frequency of the slow scan axis is 2 Hz when imaging with 100 lines/frame. As the first dominant mechanical resonance frequency should be 10 to 100 times the positioning bandwidth [11], a first dominant mechanical resonance frequency of 200 Hz is sufficient to actuate the slow scan axis at 2 Hz.

Although the bandwidth requirement of the y-actuation is low compared to the x- and z-actuation, the y-scanner is the outermost actuator of the nested design, moving the total mass of all inner actuators, which is approximately 385 g. The data sheet of the in house available NPXY100-100 (nPoint, Middleton, US-WI) nanopositioning stage specifies a resonance frequency of  $f_{res} = 700$  Hz and a stiffness  $k = 1.2$  N/ $\mu$ m. Considering the nanopositioning stage as a mass spring system with the effective moved mass  $m_0$ , the angular resonance frequency  $\omega_0 = \sqrt{k/m_0}$  [13]. Using the values from the data sheet, the effective moved mass of the unloaded nanopositioning stage is calculated as  $m_0 = k/\omega_0^2 = 62$  g. With the additional mass of all inner actuators the expected resonance frequency is calculated as  $f_{res,loaded} = (1/2\pi)\sqrt{k/(62\text{ g} + 385\text{ g})} = 260$  Hz. Therefore the available nanopositioning stage is an appropriate choice as the expected mechanical resonance frequency is higher than the requested resonance frequency of 200 Hz.

### 5.2.4 Laser alignment on the cantilever

The laser spot on the cantilever can be aligned by manipulating the beam incident on mirror A in Fig. 5.3. Tilting the beam leads to a misalignment between the actuation directions and the optical path resulting in crosstalk between the actuation and the deflection readout. Therefore aligning the laser has to be done by a parallel movement of the beam incident on mirror A. The parallel movement can be done by moving the laser source or an additional optical assembly. To be independent of the size, mass, and position of the laser source, the assembly shown in Fig. 5.12 is used to shift the laser in parallel by moving a lens perpendicular to the laser axis. By moving the lens the optical path length does not change.

To align the laser spot at the center of the QPD, the printed circuit board covering the QPD is mounted on a two dimensional translation stage. The  $66^\circ$  rotation of the deflection direction (see Sec. 5.1.3 and Fig. 5.5) is compensated by rotating the translation stage by the same  $66^\circ$ .

The benefit of the presented design is that both, the alignment mechanisms to align the laser on the cantilever and the alignment mechanisms to align the laser on the QPD are fixed and not scanned. Therefore, their size and mass are not influencing



Figure 5.11: Nanopositioning Stage NPXY100-100 (nPoint, Middleton, US-WI).

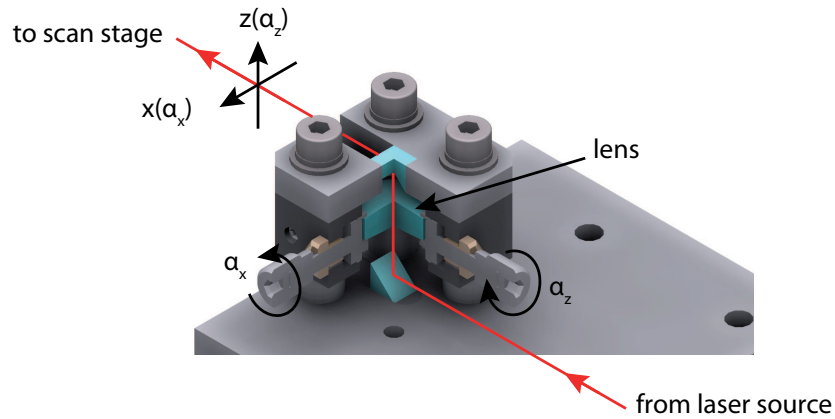


Figure 5.12: Alignment mechanism to shift the laser beam in parallel. A spring loaded focusing lens is shifted by two lead screws. The rotation  $\alpha_x$  is transformed to a parallel movement  $x(\alpha_x)$  and the rotation  $\alpha_y$  is transformed to a parallel movement  $y(\alpha_y)$  of the output beam, that is directed to the scan stage.

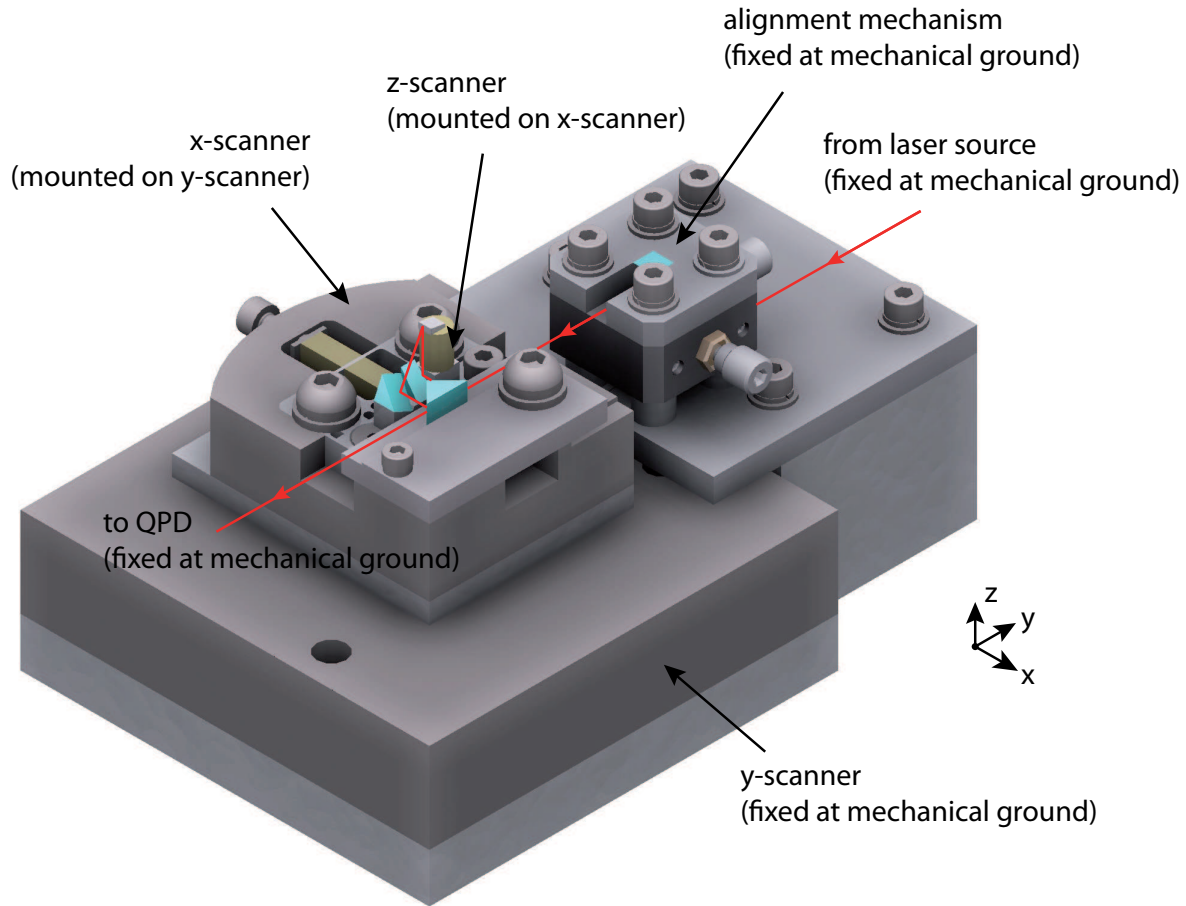


Figure 5.13: The overall serial design of the three dimensional scan stage including the optical path and the alignment mechanism.

the achievable scan speed. Furthermore the motorization or the replacement with motorized stages in future designs is much easier.

### 5.2.5 Assembly

The overall serial design of the three dimensional scan stage including the optical path and the alignment mechanism is shown in Fig. 5.13. The desired scan speed increases with each nested stage while the moved mass decreases.

The realization of the proposed scanning lever system is shown in Fig. 5.14. The laser source (a) consists of a laser diode HL6312G (OpNext Japan, Inc., Yokohama City, Japan) with a collimator GS8020A (Roithner Lasertechnik GmbH, Vienna, Austria) mounted in a temperature controlled mount TCLDM9 (Thorlabs, Inc., Newton, US-NJ) and is driven by a laser diode controller LDC501 (Stanford Research Systems, Inc., Sunnyvale, US-CA). The laser beam is shaped by an aperture stop of 1.2 mm followed by a beam expander (b) magnifying the beam 3 times to 3.6 mm diameter. The beam expander is built of two plano convex lenses with a focal length of 75 mm and 25.4 mm (LA1608-A and LA1951-A, Thorlabs, Inc., Newton, US-NJ) with a 25  $\mu\text{m}$  pinhole at

the focal plane for spatial filtering. The laser alignment mechanism (c) and the scan stage (d) are realized as shown in Fig. 5.13. A three dimensional translation stage with a custom made magnetic sample holder (e) is used for statically positioning the sample. To compensate for the crosstalk between the z-actuation and the deflection readout, an additional focusing lens (f) as proposed in Chapter 4 is used in front of the QPD. The QPD in combination with the TIAs is designed according to Sec. 3.3. To align the laser spot at the center of the QPD, the printed circuit board covering the QPD is mounted on a two dimensional translation stage (g). The  $66^\circ$  rotation of the deflection direction (see Sec. 5.1.3 and Fig. 5.5) is compensated by rotating the translation stage by the same  $66^\circ$ . For simplicity only two quadrants of the QPD are used as split detector using a high speed differential amplifier (h) with a bandwidth of 74 MHz.

### 5.3 Conclusion

The optical beam deflection method is integrated in a flexure-based (in plane movement) scanning lever AFMs. By folding the optical path according to the serial actuation principle, tracking the cantilever without moving the laser source, the detector, and the alignment mechanisms is possible. For the design and analysis of the optical path a suitable ray tracing algorithm is developed and implemented in MATLAB. The design of the serial scanner is discussed with a focus on high mechanical resonance frequencies to facilitate high speed scanning. Operating the presented scanning lever system is the aim of Chapter 6.

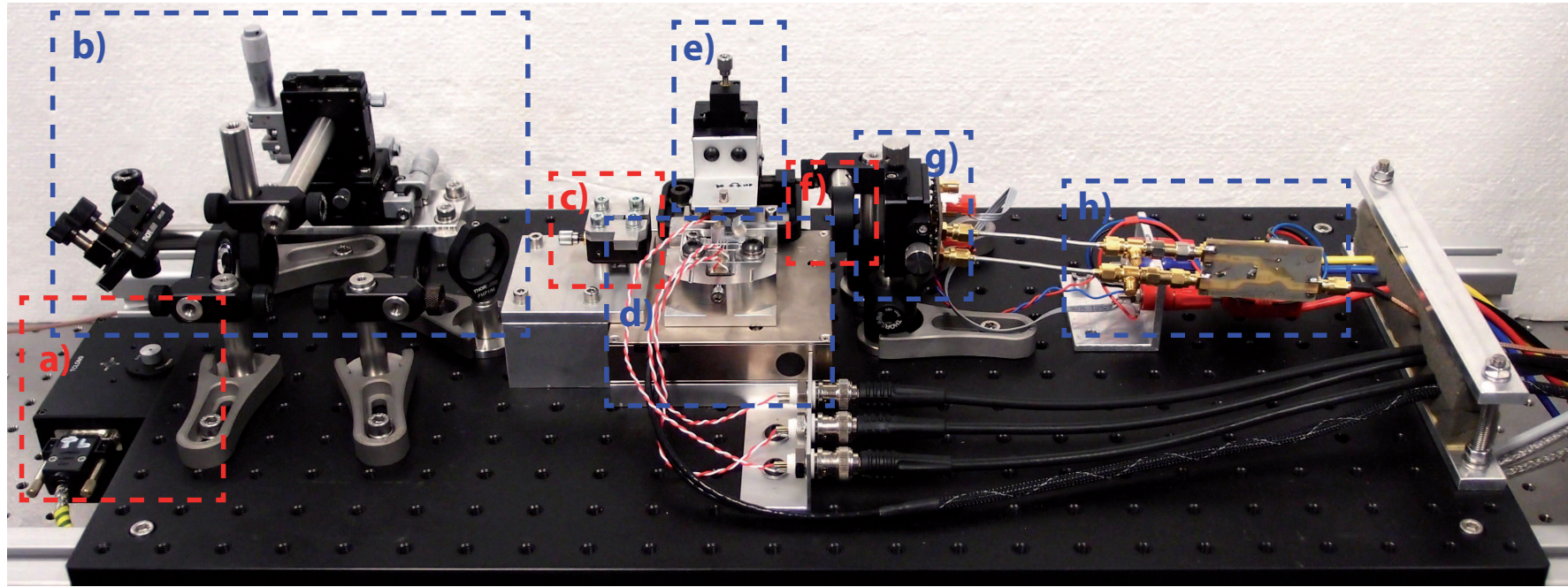


Figure 5.14: Scanning Lever AFM consisting of a) Laser source, b) Beam expander, c) Alignment mechanism, d) Scan stage, e) Sample holder including manual positioning f) Focusing lens in front of QPD, g) QPD including TIAs mounted on alignment stage, h) Differential amplifier

---

## Operation and validation of the presented scanning lever AFM

---

The aim of this chapter is to operate and validate the scanning lever AFM presented in Chapter 5. The first part of this chapter focuses on the implementation of the additional components required to operate the scanning lever AFM. In a second part the dynamics of the presented scanning lever AFM are analyzed in the time and frequency domain. The third part shows imaging with the scanning lever design presented in Chapter 5.

### 6.1 Realization and implementation of additional components used to operate the scanning lever system

In order to use the scanning lever AFM presented in Chapter 5 for imaging, additional components are necessary. The generation and amplification of the scan signal driving the stack piezos of the x- and y-scanner is needed for raster scanning. The cantilever deflection is measured by the system presented in Chapter 3 and fed back to the z-actuator via the z-feedback controller driving a high voltage amplifier connected to the stack piezo of the z-scanner. In parallel a data acquisition system (DAQ) has to record the deflection signal as well as the output signal of the z-feedback controller. To operate the AFM a graphical user interface (GUI) helps the user to control the single components.

#### 6.1.1 Trajectories for raster scanning

To get a constant relative tip sample velocity, a raster scan pattern compromised of triangular components in the x- and y-direction is desired. The triangular signal can be represented by the Fourier series [13]

$$g_{tri}(t) = \frac{8}{\pi^2} \left( \cos(\omega t) + \frac{1}{3^2} \cos(3\omega t) + \dots + \frac{1}{n^2} \cos(n\omega t) \right) \text{ with } n = 1, 3, 5, \dots \quad (6.1)$$

with the fundamental angular frequency  $\omega = 2\pi f$ . Therefore actuating the x/y-scanner with a triangular signal including high frequency components can excite mechanical resonances of the scanner. Exciting mechanical resonances is not limited to the driving actuator since mechanical resonances of other actuators or structures can be excited due to mechanical cross coupling as well [53]. Excited resonances can introduce image distortions by disturbing the scanning motion [51][52]. Although the amplitude of the harmonic components are decreasing by  $1/n^2$ , for high speed scanning the lower harmonics with a high amplitude may coincide with weakly damped mechanical resonances of the scanner.

### Model inversion

A common way to avoid the excitation of mechanical resonances is filtering the scan signal with the inverse dynamic of the plant model [13]. Therefore an accurate model of the system is necessary for model inversion. For a periodic signal it is sufficient to adapt the magnitude and phase of the harmonic components according to the measured frequency response, instead of identifying and inverting the whole system dynamics [71]. The drawback of these methods is their sensitivity to model uncertainties.

### Two-degrees of freedom control

To correct for residual errors when using model inversion, additional feedback control can be added, resulting in a two-degrees of freedom control [59]. However, the applicability of feedback control depends on the design of the AFM system, i.e. whether position sensors are available to measure the x- and y-position. Furthermore the feedback control induces additional sensor noise.

### Iterative learning control

To avoid the amplification of sensor noise, iterative learning control can be used to correct for model uncertainties by updating the trajectory based on the previous response to the trajectory [72][73]. However, besides the time necessary for converging, the applicability of iterative learning control depends on the availability of sensors too.

### Input-shaping

Another method called input-shaping, modifies the input signal according to the system dynamics [13]. As shown in Fig. 6.1, instead of changing the slope of the triangular signal at a single point, the turn around is separated into two points delayed by half the period of the systems resonance frequency. Assuming the system to be linear the mechanical resonance is excited at both positions where the slope changes. As they are delayed by half the period of the systems the resonance is excited two times with a phase difference of  $180^\circ$ , and therefore compensating each other [13].

For a first dominant mechanical resonance frequency  $f_{res}$ , the triangular signal

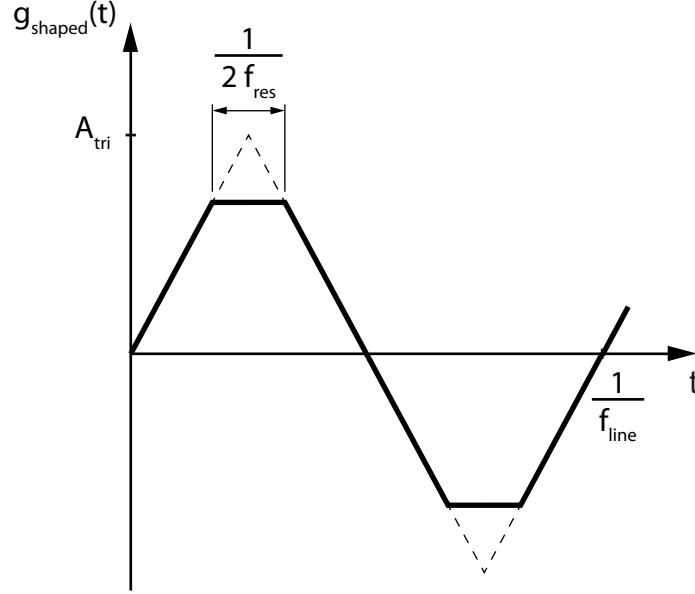


Figure 6.1: Input shaping of the triangular signal of frequency  $f_{line}$  for a scanner with a first dominant mechanical resonance frequency  $f_{res}$ .

$g_{tri}(t)$  with a frequency  $f_{line}$  and an amplitude  $A_{tri}$  is shaped to

$$g_{shaped}(t) := \begin{cases} g_{tri}(t) & \text{if } |g_{tri}(t)| \leq A_{tri} \left(1 - \frac{f_{line}}{f_{res}}\right) \\ \text{sgn}(g_{tri}(t)) A_{tri} \left(1 - \frac{f_{line}}{f_{res}}\right) & \text{if } |g_{tri}(t)| > A_{tri} \left(1 - \frac{f_{line}}{f_{res}}\right) \end{cases} \quad (6.2)$$

This method works best if there is only one dominant mechanical resonance [56]. Although this method is sensitive to model uncertainties too, only the actual value of the resonance frequency is of interest.

### Low-pass filtering

A method more robust against model uncertainties is low-pass filtering the triangular signal [56]. For periodic signals, the low-pass filtered signal can be synthesized by combining all harmonic components below the first dominant mechanical resonance. The biggest disadvantage of low-pass filtering is the ripple introduced to the linear scan region [56].

### Optimization based scan signal

Specifying a linear range an optimization based method can be used to calculate the reference trajectory for scanning [56]. The idea of the optimization based scan signal

generation presented in [56] is based on the vector

$$r = \begin{bmatrix} r_0 \\ r_1 \\ \vdots \\ r_{N-1} \end{bmatrix} \quad (6.3)$$

containing the  $N$  samples of the time discrete triangular reference signal and the selection matrix  $S$  containing the indices of samples in  $r$  fixed to the triangular signal while the others can be varied by the optimization algorithm. The scan trajectory  $y_{opt}$  is derived by minimizing the quadratic cost function  $x^T H x$  as solution to [56]

$$y_{opt} = \arg \min_x x^T H x \quad (6.4)$$

subject to  $x_k = r_k$  with  $k \in S$ .

Depending on the weighting function  $H$  the quadratic cost  $x^T H x$  can represent different frequency or time domain cost functions. As mechanical resonances of the scanner can be excited by higher harmonics of the triangular scan signal, the expression from Eq. 20 in [56] is used as weighting function  $H$  that represents the signal power above a certain harmonic  $K$ . For further information refer to [56]. As shown in [56], the minimization problem from Eq. 6.4 can be formulated as linearly constrained convex quadratic optimization problem [74]. The implementation of the presented algorithm is done in MATLAB.

### 6.1.2 Generating arbitrary scan trajectories

As dedicated AFM controllers usually do not offer the flexibility to use arbitrary scan signals, standard laboratory equipment is used to investigate the response to different scan trajectories. Using arbitrary signal generators allows to easily generate the desired scan trajectories. The signals are calculated offline using MATLAB and are transferred to the two channel arbitrary signal generator 33522B (Agilent, Santa Clara, US-CA) using the Virtual Instrument Software Architecture (VISA) over Ethernet.

#### Synchronizing arbitrary scan trajectories

To allow accurate and reliable imaging, the signal generation and data acquisition system must be synchronized to an external reference signal. Many standard laboratory instruments allow to lock there internal phase-locked loop (PLL) to an external 10 MHz reference signal. Furthermore lines and frames can be synchronized to trigger signals derived from the fast and slow scan signal generation.

In addition to locking the signal generators to an external reference or using internally locked multi-channel signal generators, the characteristic of the output filters has to be considered. A different phase delay is introduced to the slow and fast scan axis signal as the frequency difference is in the order of two to three magnitudes. Using the function generator 33522B (Agilent, Santa Clara, US-CA) there are three possible output filter settings.

When disabled, the output changes with a transition time of approximately 10 ns. To avoid a stepped output signal with high frequency components, possible combinations of the sampling rate and signal frequency are considered. Scaling the signals to use the whole DAC range from  $-2^{15}$  to  $2^{15}$  at a sampling rate as close as possible to the maximum sampling rate of 60 MSPS gives a smooth output signal. For signals below 60 Hz the maximum sampling rate is limited by the waveform memory of  $10^6$  points. For high speed scanning with line rates higher than 60 Hz the waveform memory limitation will mainly affect the slow scan axis. However, measurements show that using a sample rate high enough to guarantee a maximum step height of 1 LSB between two consecutive sampling points the quantization noise is covered by more dominant noise sources of the instrument (data not shown). Assuming a triangular scan signal, using the whole DAC range from  $-2^{15}$  to  $2^{15}$  requires  $2 \cdot 2^{16}$  points to guarantee a maximum step height of 1 LSB. A 60 Hz triangular scan signal with  $2 \cdot 2^{16}$  points leads to 7.86 MSPS. The function generator 33522B allows a maximum step height of 1 LSB for all triangular scan signals below 60 Hz while a maximum sampling rate of 60 MSPS is possible for scan signals up from 60 Hz. Therefore the function generator 33522B can be used to generate a smooth output signal without unwanted high frequency components with the output filters switched off.

### Minimizing jerks when starting/stopping the scan motion

Switching the output of the function generator on and off causes steps in the output signal when not aligned to the zero crossings of the scan signal. If the function generator is directly connected to the high voltage amplifier driving the actuator, the system is excited by the step signal. The resulting jerk can affect the alignment by displacing prealigned parts of the optical path or even worse damage the cantilever and other mechanical components.

As the function generator 33522B does not offer a way to smoothly fade the signal in and out, additional functionality between the output of the function generator and the actuator is necessary. Although some high voltage amplifiers offer a "soft start/stop" functionality, that is not true for all and therefore the assortment is limited. Even if the "soft start/stop" functionality is given, the user is responsible for switching off the high voltage amplifier before switching on and off the output or loading new waveforms to the function generator. This procedure is error-prone resulting in a high risk of damaging individual components of the AFM. Manipulating the low voltage signal at the output of the function generator is easier than manipulating the high voltage signal at the output of the high voltage amplifier. Therefore an additional electronic component is designed to smoothly fade in and out the signal driving the high voltage amplifier to minimize jerks.

For continuously changing the scan size the output of the function generator is multiplied by the analog scan size signal as shown in Fig. 6.2. The electronics used for multiplying is based on the analog multiplier AD633 (Analog Devices, Norwood, US-MA) with a bandwidth of 1 MHz. By using a signal with a smooth transition from zero to one and back, it is possible to start and stop the scanning motion without any steps in the actuation signal. To minimize jerks when fading in and out, the minimum

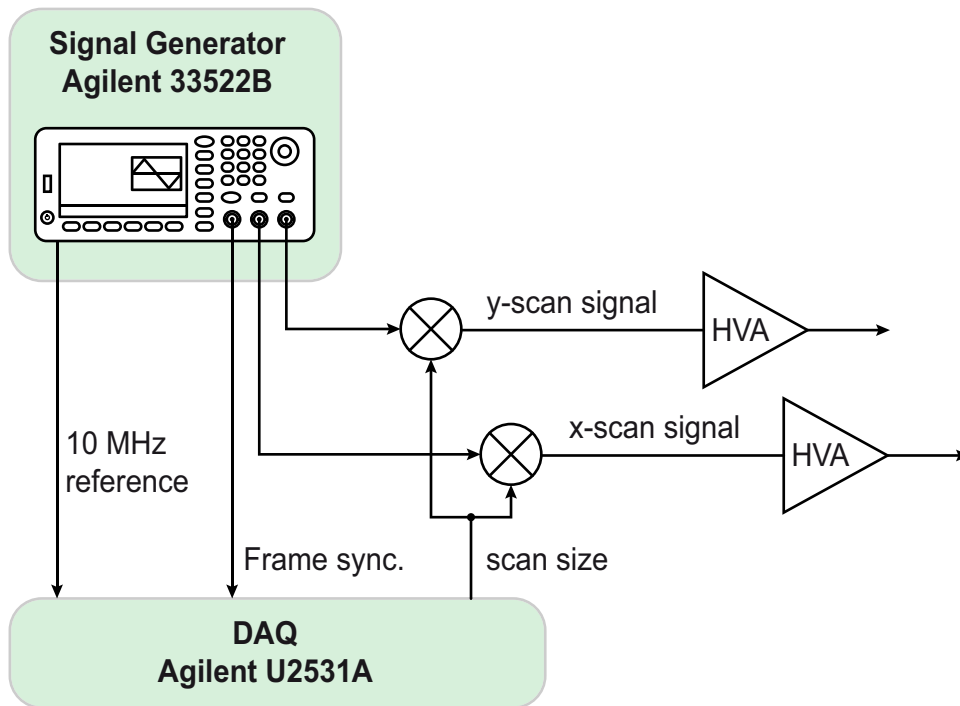


Figure 6.2: Continuously changing the scan size to minimize jerks. The output signal of the function generator is multiplied with the minimum jerk trajectory generated by the analog output of the data acquisition unit. The multiplied signals are connected to the inputs of the high voltage amplifiers (HVA).

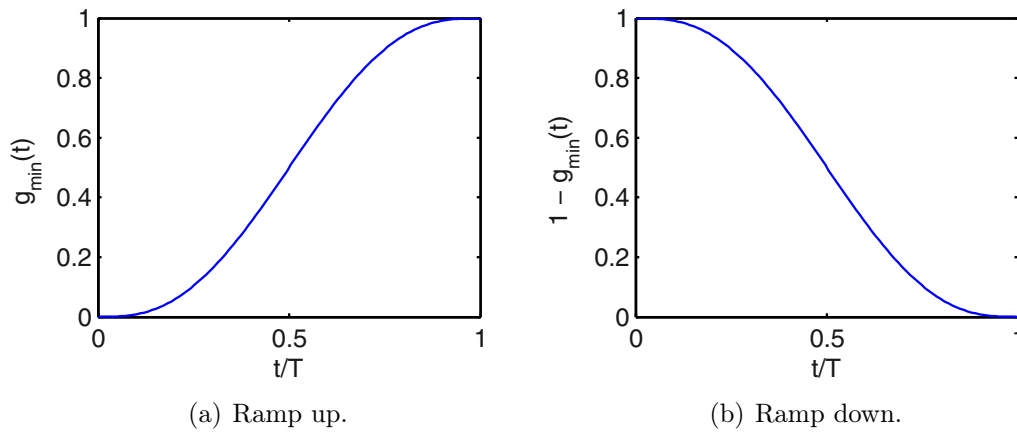


Figure 6.3: Minimum jerk trajectory used to continuously change the scan size. The output signal of the function generator is multiplied with the minimum jerk trajectory as shown in Fig. 6.2.

jerk trajectory [75]

$$g_{\min}(t) = 6 \left( \frac{t}{T} \right)^5 - 15 \left( \frac{t}{T} \right)^4 + 10 \left( \frac{t}{T} \right)^3 \quad (6.5)$$

is used to rescale the scan size. The transition of the minimum jerk trajectory from zero to one and back is shown in Fig. 6.3.

To generate the minimum jerk signal the analog output of the data acquisition unit U2531A (Agilent, Santa Clara, US-CA) is used. By using the Virtual Instrument Software Architecture (VISA) interface of both, the function generator and the data acquisition unit, the procedure of fading in and out before changing the output state of the function generator, is automatized. Therefore operating the system is easier and the risk of damaging the system by maloperation is minimized.

### 6.1.3 Driving the stack piezos

All stack piezos are driven by a single channel of a high voltage amplifier (Techproject Company, Vienna, Austria). To extend the range, the x-scanner is actuated by two piezo actuators mechanically connected in series [76]. The two piezo actuators can be driven by one high voltage amplifier when electrically connected in series or in parallel. Connecting them in parallel leads to twice the capacitance reducing the actuation bandwidth while connecting them in series requires twice the output voltage to fully extend both piezo actuators. To overcome these limitations each piezo actuator is connected to its own high voltage amplifier where the inputs of the high voltage amplifiers are connected in parallel.

### 6.1.4 z-Feedback controller

As z-feedback controller a proportional-integral (PI) controller is implemented on a rapid prototyping system (dSpace, Paderborn, Germany). The rapid prototyping system mainly consists of the DS1005 processor board and the DS5203 FPGA board mounted in a PX10 expansion box. For programming and data exchange the processor board is connected to the FPGA board via the internal PHS bus. The analog deflection signal is connected to the 14-bit analog to digital converter on the FPGA board. The signal is sampled with 10 MSPS and processed by the PI-controller implemented on the FPGA. The digital output of the PI-controller is converted to an analog signal by the 14-bit digital to analog converter at a sampling rate of 10 MSPS. The analog output signal is connected to the high voltage amplifier (Techproject Company, Vienna, Austria) driving the z-piezo.

The feedback controller is user tuned for imaging. That is done by first increasing the I-gain until ringing is visible and then reducing the gain around 10 %. By increasing the P-gain no improvement of the imaging quality is observed. Therefore tuning is done by adjusting the I-gain only.

### 6.1.5 Data acquisition

The output of the z-feedback controller (height information) and the deflection signal (remaining control error) is recorded with the data acquisition unit U2531A (Agilent, Santa Clara, US-CA). The data acquisition must be synchronized to the lateral scanning motion. This is done by synchronizing frames with the trigger signal generated by function generator 33522B, that is used for the scan signal generation. Additionally, the internal clock source of the DAQ is synchronized to the same external reference as the function generator.

The minimum sampling rate is determined by the requested imaging resolution and line scan rate. Imaging with a resolution of  $n$  pixel per line at a line scan rate of  $f_{line}$  requests a sample rate of  $2 \cdot n \cdot f_{line}$  for recording trace and retrace. The maximum sampling rate of the U2531A is 2 MSa/s per channel at a resolution of 14 bits. As a maximum line scan rate around 500 Hz is expected for the presented design, this is sufficient for high resolution imaging with up to 2000 pixel/line.

### 6.1.6 The graphical user interface

The imaging system is controlled by a GUI implemented in MATLAB. The main window of the GUI shown in Fig. 6.4 allows to set the scan resolution, scan rate, scan size, scan trajectory, and feedback gain.

By pressing the "Start" button, the scan trajectory is calculated based on the selected type, frequency, and optional and parameters. The calculated scan trajectory is downloaded to the arbitrary signal generator. The amplitude and sampling rate is set based on the scan size and frequency settings in the GUI. After finishing the download and configuration of the arbitrary signal generator, the GUI uses the analog output of the data acquisition unit to generate the minimum jerk signal that is multiplied with the scan signal to start scanning. Using the minimum jerk trajectory, the GUI automatically starts and stops the scan motion with minimum jerks to avoid displacing

## 6 Operation and validation of the presented scanning lever AFM

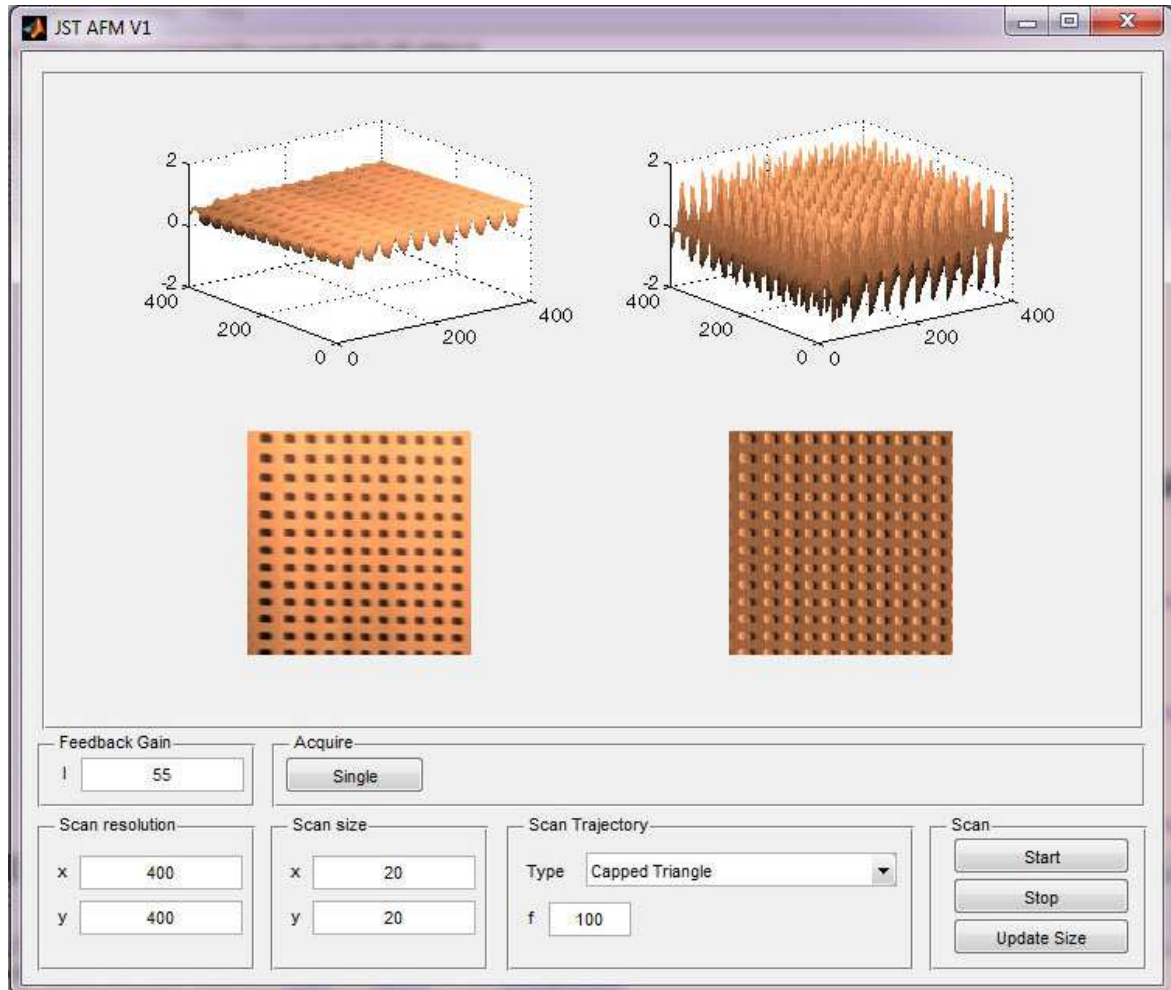


Figure 6.4: The GUI used for imaging allows to set the scan resolution, scan rate, scan size, scan trajectory, and feedback gain. The GUI automatically starts and stops the scan motion with minimum jerks. The GUI automatically stores all acquired images including additional information like date, time, scan rate, scan size, and feedback gain.

prealigned parts or damage of mechanical parts (see Sec. 6.1.2). The "Update Size" button changes the scan size by stopping the scan motion with the minimum jerk trajectory, changing the amplitude of the function generator, and starting again with the minimum jerk trajectory.

Pressing the "Single" button in the "Acquire" box triggers the acquisition of a single frame by the data acquisition unit. After the acquisition is done, the height (output of the z-feedback controller) and the deflection signal (remaining control error) is shown in the upper part of the GUI. Next to the acquisition, the GUI automatically stores all acquired images including additional information like date, time, scan rate, scan size, and feedback gain.

## 6.2 System dynamics

As mentioned, the scanner dynamics are one of the determining factors for the achievable imaging speed. Modifying the triangular scan signal to avoid the excitation of resonances requires the knowledge of the system dynamics. Therefore the frequency response of each scan axis of the scanning lever system presented in Chapter 5 is measured. In addition to the frequency response, the time domain response to the model based input-shaping and the optimization based scan trajectories is measured and analyzed for the fast scan axis.

### 6.2.1 Frequency domain

To measure the frequency response of the x-, y-, and z-scanner the dynamic signal analyzer HP3562A (Agilent, Santa Clara, US-CA) is used. The output of the dynamic signal analyzer is connected to the input of the respective high voltage amplifier driving the desired actuator of the scanner. The displacement of the scanner is measured using a single point laser Doppler vibrometer (Polytec GmbH, Waldbronn, Germany). The laser Doppler vibrometer consists of the OFV-534 compact sensor head connected to the OFV-5000 vibrometer controller with the DD-900 digital displacement decoder. The output signal of the digital displacement decoder is connected to the input of the dynamic signal analyzer. The frequency response is measured by sweeping the frequency of the sinusoidal output signal while measuring the displacement by the laser Doppler vibrometer.

#### x-Scanner Characterization

The frequency response of the x-scanner is measured from the input of the high voltage amplifier (Techproject Company, Vienna, Austria) to the output of the laser Doppler vibrometer pointing to the side wall of the aluminum wedge where the cantilever is fixed (see Fig. 5.9). The measured frequency response in the range from 100 Hz to 100 kHz is shown in Fig. 6.5 where the first dominant resonance can be seen at 5.7 kHz.

The measured dominant mechanical resonance of the x-scanner without the nested z-scanner is at 14.45 kHz (data not shown). Considering the system as a mass spring system with the intrinsic stiffness denoted by  $k$ , the moved mass of the x-scanner denoted by  $m_0$  and the additional mass of the z-scanner denoted by  $m_1$ , the angular

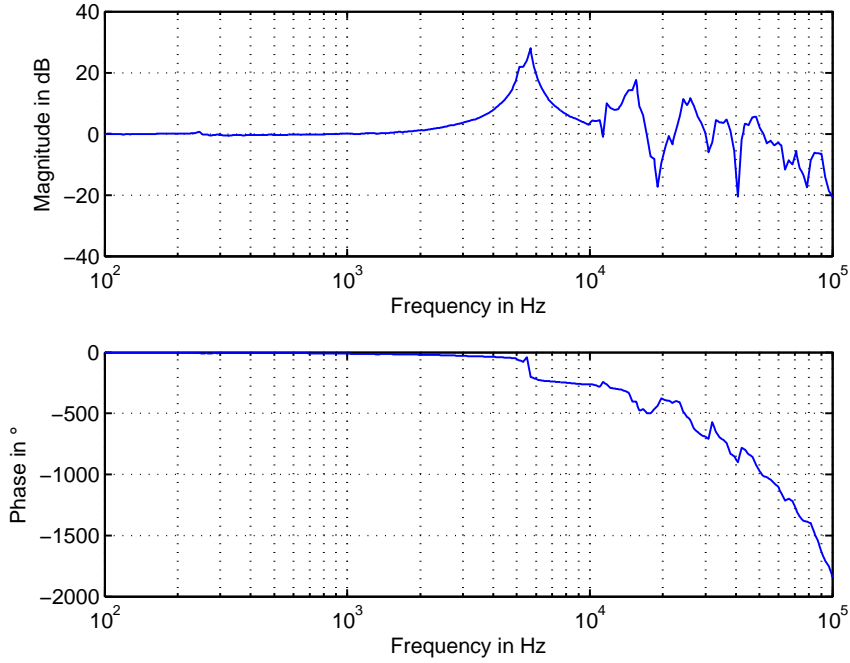


Figure 6.5: Frequency response of x-Scanner.

resonance frequency of the x-scanner without the the nested z-scanner is  $\omega_0 = \sqrt{k/m_0}$  and the angular resonance frequency including the z-scanner is  $\omega_{01} = \sqrt{k/(m_0 + m_1)}$  [13]. With the known mass of the z-scanner that is 3.65 g the moved mass  $m_0$  can be calculated as

$$m_0 = \frac{1}{\frac{\omega_0^2}{\omega_{01}^2} - 1} = 0.617 \text{ g} \quad (6.6)$$

by assuming an equal stiffness  $k$  for both configurations. The 0.617 g are equal to the mass of an aluminum cube with a mass density of  $2.7 \text{ g/cm}^3$  and a side length of 6.1 mm. As this is approximately the volume of the inner part of the x-scanners flex structure, it is assumed that this part with the mounted z-scanner resonates at the measured 5.7 kHz, decoupled from the driving piezos.

### y-Axis Characterization

The frequency response of the y-scanner is measured from the analog input to the LC.402 DSP controller (nPoint, Middleton, US-WI) to the output of the laser Doppler vibrometer pointing to the front wall of the aluminum wedge where the cantilever is fixed. The internal controller of the LC.402 is disabled to utilize the high voltage amplifier only. The measured frequency response in the range from 10 Hz to 10 kHz is shown in Fig. 6.6 with the following resonances and anti-resonances:

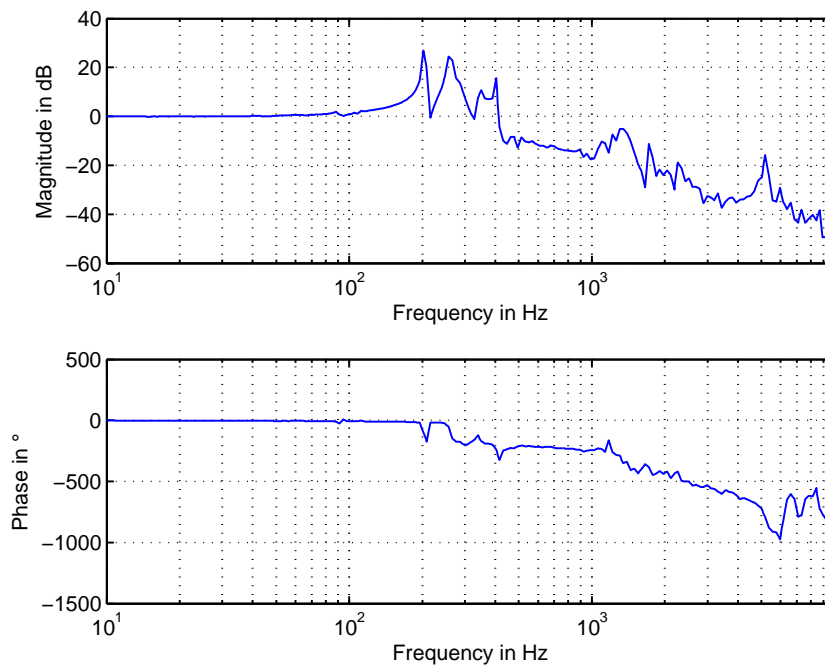


Figure 6.6: Frequency response of y-Scanner.

Resonance	Anti-resonance
202 Hz	218 Hz
257 Hz	327 Hz
347 Hz	
402 Hz	

### z-Axis Characterization

The frequency response of the z-scanner is measured from the input of the high voltage amplifier (Techproject Company, Vienna, Austria) to the output of the laser Doppler vibrometer pointing to the top of the aluminum wedge where the cantilever is fixed (see Fig. 5.9). The measured frequency response in the range from 100 Hz to 100 kHz is shown in Fig. 6.7 with the following resonances and anti-resonances:

Resonance	Anti-resonance
11 kHz	13.7 kHz
14.8 kHz	15.1 kHz
16.3 kHz	17.4 kHz
21.4 kHz	22.5 kHz

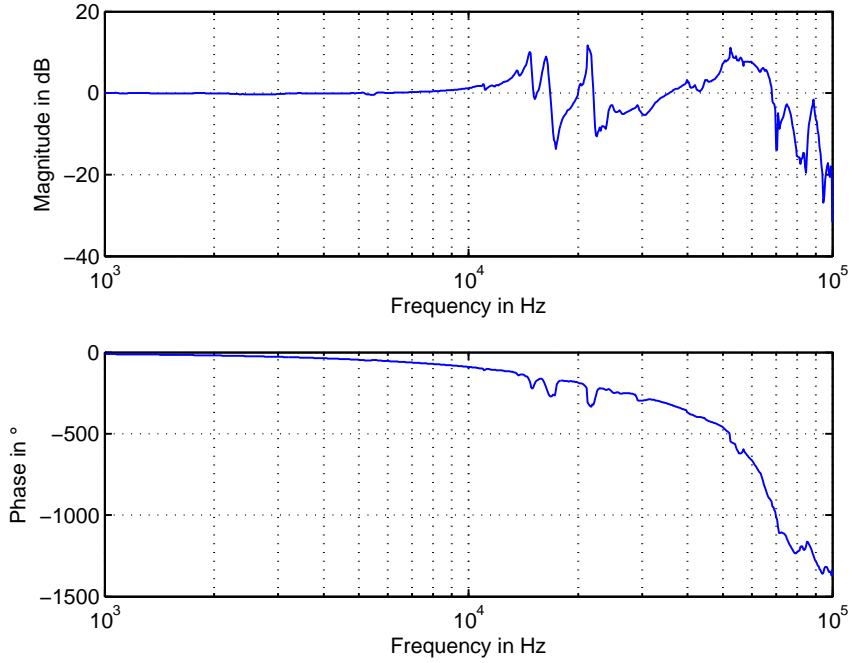


Figure 6.7: Frequency response of z-Scanner.

## 6.2.2 Time domain

The time domain analysis is done by testing the system response of the fast scan axis to the model based input-shaping and the optimization based scan trajectories. The signal is generated using the setup described in Sec. 6.1.2 and applied to both piezos of the fast scan axis via two channels of the high voltage amplifier (Techproject Company, Vienna, Austria) with their inputs connected in parallel. As for the frequency domain analysis, the displacement of the scanner is measured using the single point laser Doppler vibrometer, pointing to the top of the aluminum wedge where the cantilever is fixed. The output signal of the digital displacement decoder is recorded using the oscilloscope DSOX4024A (Agilent, Santa Clara, US-CA).

From the system response shown in Fig. 6.5, the first dominant mechanical resonance of the fast scan axis is at 5.7 kHz. The system response is measured up to about  $1/10^{th}$  of the first dominant mechanical resonance, at 100 Hz, 300 Hz, and 600 Hz.

### Response to input-shaping

From the system response shown in Fig. 6.5, the first dominant mechanical resonance of the fast scan axis is a 5.7 kHz. The triangular shaped scan trajectory  $g_{shaped}$  is calculated using  $f_{res} = 5.7$  kHz in Eq. 6.2.

For a line scan rate of 100 Hz, Fig. 6.8 shows the input signal that is connected to the high voltage amplifier (blue), the displacement measured at the aluminum wedge (green), and the error (cyan) with respect to a triangular reference (dashed red). The reference is the result of fitting the amplitude and phase of an ideal triangular signal to

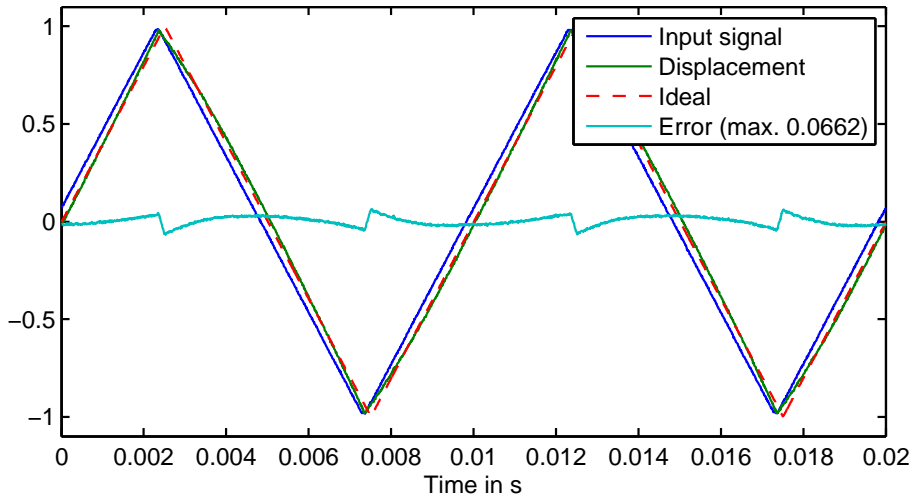


Figure 6.8: The 100 Hz scan trajectory based on input shaping (blue), the displacement measured at the aluminum wedge (green), and the error (cyan) with respect to a triangular reference (dashed red). The flat part of the scan trajectory is not visible as the temporal resolution is too low. No distortions from system dynamics are visible. The hysteresis of the piezo actuators is noticeable.

the measured displacement in a first step and then scaling the amplitude of all signals by the same value to get a normalized reference signal in a second step. Fitting the reference signal is valid as the amplitude and phase can be adjusted by calibration in a real system too.

Although distortions from system dynamics are not visible, the hysteresis of the piezo actuators is noticeable. The maximum error with respect to the reference trajectory is 0.0662. Without additional sensors, the nonlinear hysteresis effects can be corrected by calibration or sensorless techniques like charge control instead of controlling the actuation voltage [77].

Increasing the line scan rate to 300 Hz, in Fig. 6.9, besides the hysteresis the first distortions due to system dynamics are barely visible. The maximum error with respect to the reference trajectory is 0.0775. By further increasing the scan speed to 600 Hz as shown in Fig. 6.10, the distortions due to system dynamics are increasing. Although the maximum error of 0.0769 is similar as the error at a scan speed of 300 Hz, each turn around is followed by two clearly visible bumps. The time between these bumps is around  $65 \mu\text{s}$ , equivalent to a frequency of 15.4 kHz. From the x-scanner characterization result shown in Fig. 6.5, the excitation of the second dominant mechanical resonance at 15.5 kHz can be assumed as source of those bumps. As the suppression of mechanical resonances by exciting them two times with a phase difference of  $180^\circ$  works only for the intended resonance frequency and with limitations for odd multiples of it, other resonances are still excited by the turn around. For the worst case, if the frequency of the second mechanical resonance is twice the frequency of the first one, the second one is excited two times in phase, resulting in a constructive interference. As the second dominant mechanical resonance at 15.5 kHz does not coincide with an

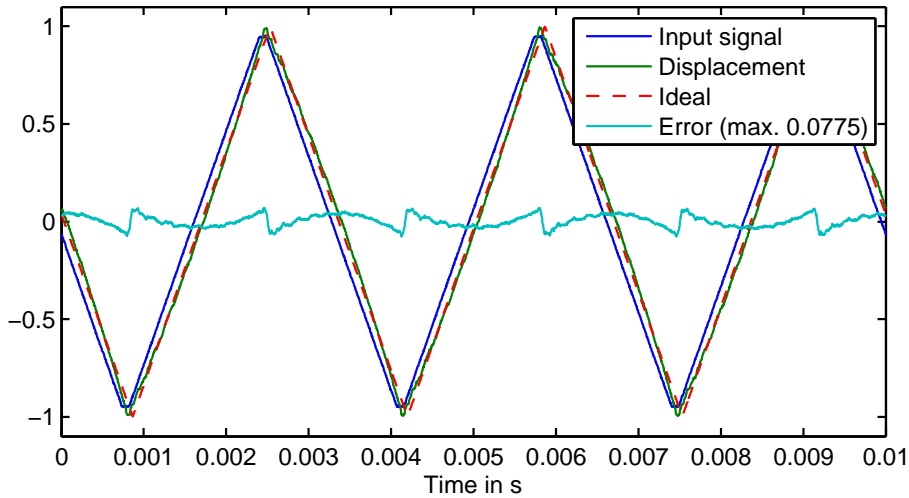


Figure 6.9: The 300 Hz scan trajectory based on input shaping (blue), the displacement measured at the aluminum wedge (green), and the error (cyan) with respect to a triangular reference (dashed red). Next to the hysteresis, distortions due to system dynamics are barely visible.

odd multiple of the first resonance frequency, the excitation by the turn around gets visible.

Additionally it can be seen that the flat part of the reference signal is not visible in the measured trajectory as the oscillation of the first resonance is triggered two times with opposite sign, resulting in an almost triangular scan signal [13]. It must be noted that this effect is limited to the first dominant resonance, as odd multiples will show additional periods of oscillation. As input shaping works best with mechanical systems of second order [56], the application for systems with higher order dynamics is only possible to a limited extend.

### Response to the optimization based scan signal

The algorithm presented in [56] is implemented in MATLAB. Using the algorithm there are two parameters, the linear range specified by  $\beta$  and the number of unrestricted harmonics denoted by  $K$ . All points within the linear range are fixed to an ideal triangular signal, not affected by the optimization algorithm. For example setting  $\beta = 0.6$  means that the centered 60% of the scan range are fixed to an ideal triangular signal. The signal power of frequency components above the  $K$ th harmonic are penalized equally by the cost function. The selection of  $K$  and  $\beta$  mainly depends on the application [56]. If there is a demand for a large linear scan range, that means a high value for  $\beta$ , the number of unrestricted harmonics  $K$  has to be increased. On the other hand, if high speed scanning is valued, the number of unrestricted harmonics  $K$  has to be reduced. If  $K$  is reduced, the linear range  $\beta$  has to be reduced too to get a smooth output signal.

Although the number of unrestricted harmonics  $K$  is usually selected with respect to the scan rate and the first dominant mechanical resonance of the scanner [56], this

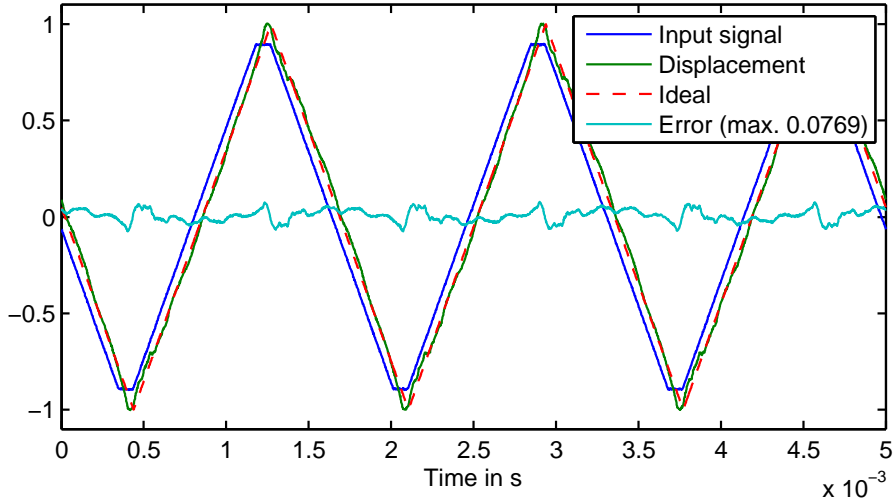


Figure 6.10: The 600 Hz scan trajectory based on input shaping (blue), the displacement measured at the aluminum wedge (green), and the error (cyan) with respect to a triangular reference (dashed red). Each turn around is followed by two clearly visible bumps. The excitation of the second dominant mechanical resonance at 15.5 kHz (cf. Fig. 6.5) can be assumed as source of those bumps.

section uses the same values of  $K$  to compare the response to the individual scan rates. Testing different combinations of  $K$  and  $\beta$  has shown that a value of  $K = 3$  is the smallest reasonable value. By reducing  $K$  to 3,  $\beta$  has to be reduced to 0.6 to get a smooth reference trajectory. Further reducing  $K$  to 2 would require a reduction of the linear range to  $\beta = 0.3$ .

For a line scan rate of 100 Hz, Fig. 6.11 shows the input signal that is connected to the high voltage amplifier (blue), the displacement measured at the aluminum wedge (green), and the error (cyan) with respect to a triangular reference (dashed red). Although there are no distortions within the 60% band around the center, minor distortions due to the system dynamics can be seen next to each turn around. The maximum error with respect to the reference trajectory is 0.0319 within the 60% band.

At a line scan rate of 300 Hz, shown in Fig. 6.12, the distortions at the turn around getting more dominant, while distortions in the 60% band are still low. The maximum error of 0.0775 within the 60% band is more than twice the error for a line scan rate of 100 Hz. The period of the distortions at the turn around is about  $175 \mu\text{s}$ , equivalent to a frequency of 5.7 kHz. From the x-scanner characterization result shown in Fig. 6.5, the excitation of the first dominant mechanical resonance at 5.7 kHz can be assumed as source of those distortions. In comparison to input shaping the first mechanical resonance is dominant over the second one, as the first mechanical resonance is not canceled by a destructive interference. A comparison of the input shaping and optimization based response at 600 Hz in Fig. 6.10 and Fig. 6.13 shows, that the distortions due to system dynamics are mainly limited to the first dominant mechanical resonance for the optimization based trajectory while higher resonances are visible too

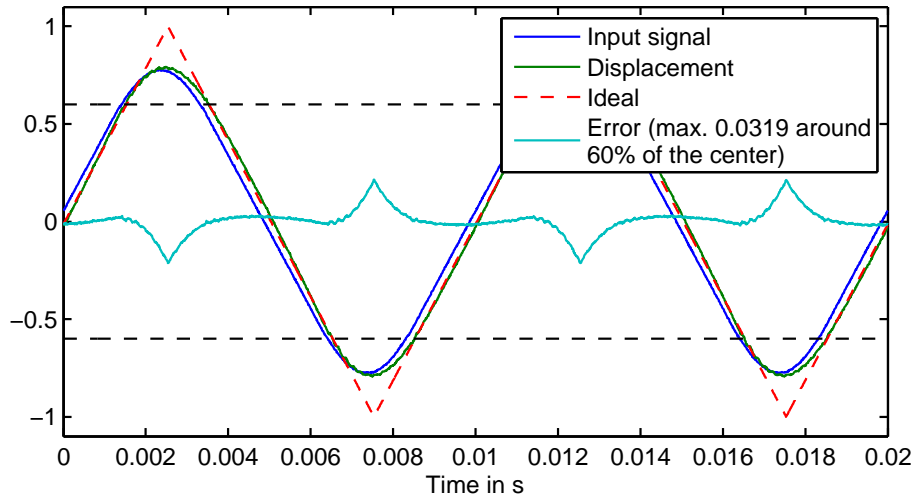


Figure 6.11: The 100 Hz optimization based scan trajectory (blue), the displacement measured at the aluminum wedge (green), and the error (cyan) with respect to a triangular reference (dashed red). The horizontal dashed lines show the band of 60% where the input signal is fixed to an ideal triangular scan signal. There are minor distortions next to each turn around.

for the same system excited by input shaping. Therefore, the optimization based scan trajectories are preferable over input shaping for systems with higher order dynamics.

### 6.3 Imaging

This section shows imaging with the scanning lever system presented in Chapter 5. To evaluate the imaging performance a calibration standard is used as sample. The calibration standard is a grid of 45 nm high pillars with a footprint of  $0.5 \times 0.5 \mu\text{m}^2$  equally spaced by  $1 \mu\text{m}$ .

Imaging is shown with both, the shaped and optimization based scan trajectory at line scan rates from 10 Hz to 625 Hz. It is not possible to use exactly the same scan rates as used in Sec. 6.2.2, as the sampling rate of the DAQ system is derived by dividing the external 10 MHz reference signal by an integer value. To allow a comparison with the one dimensional time domain responses, line scan rates similar to ones in Sec. 6.2.2 are used for imaging. A reference scan is done a slow scan rate of 10 Hz to avoid the excitation of mechanical resonances. Imaging at a line scan rate of 100 Hz is done at full range to show fast imaging performance. High speed imaging at a line scan rate of 625 Hz is done at a reduced lateral range to avoid a limitation by the tracking bandwidth of vertical feedback loop.

#### Imaging with the input shaped scan trajectory

Fig. 6.14 shows a full range scan at a line scan rate of 10 Hz. The left side shows the output of the z-feedback controller (height information) and the right side shows the

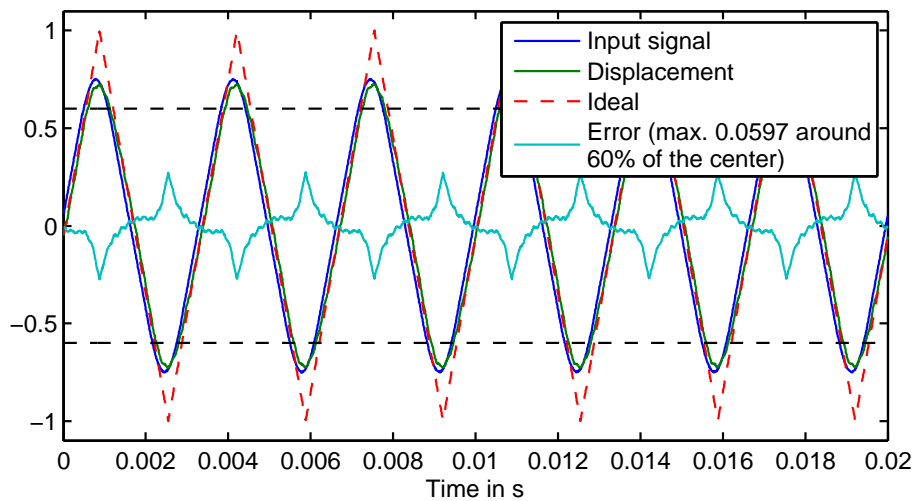


Figure 6.12: The 300 Hz optimization based scan trajectory (blue), the displacement measured at the aluminum wedge (green), and the error (cyan) with respect to a triangular reference (dashed red). The horizontal dashed lines show the band of 60% where the input signal is fixed to an ideal triangular scan signal. There are distortions next to the turn around, while distortions in the 60% band are low.

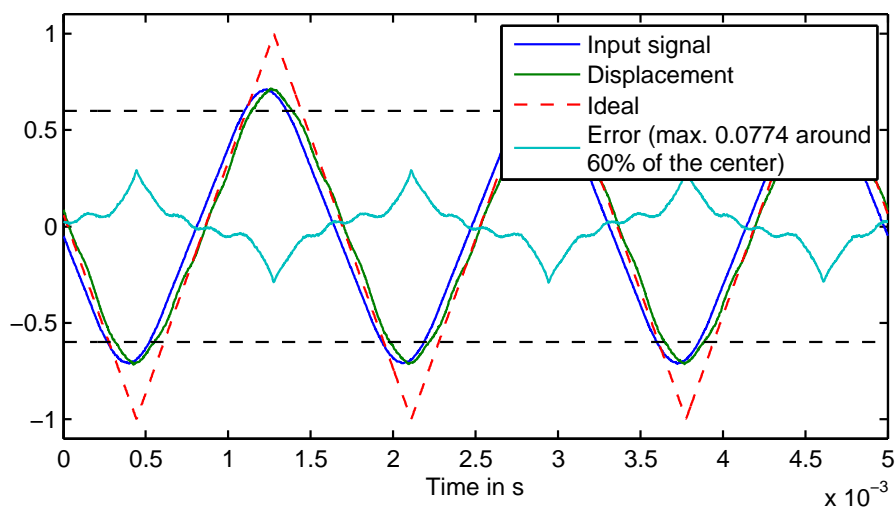


Figure 6.13: The 600 Hz optimization based scan trajectory (blue), the displacement measured at the aluminum wedge (green), and the error (cyan) with respect to a triangular reference (dashed red). The horizontal dashed lines show the band of 60% where the input signal is fixed to an ideal triangular scan signal. The distortions from first dominant mechanical resonance are clearly visible within the 60% band.

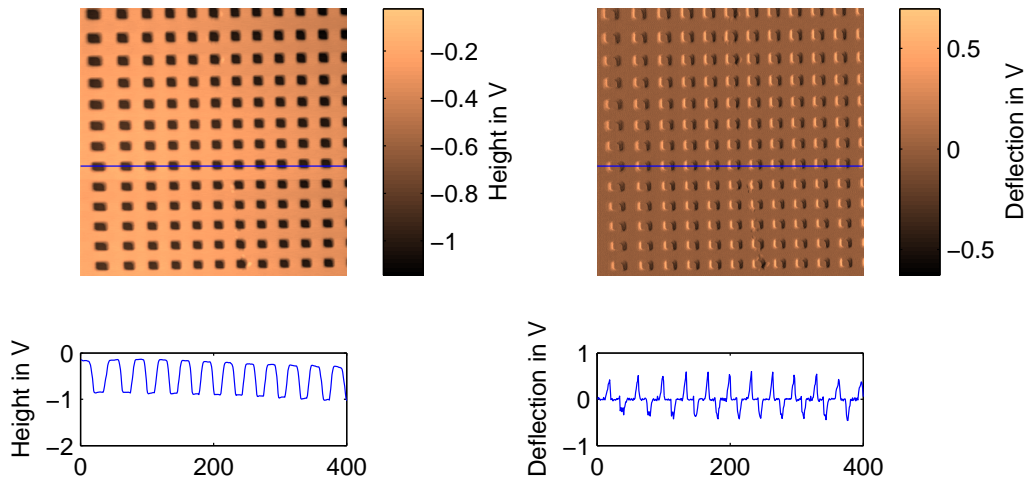


Figure 6.14: Image of a calibration standard with 45 nm high pillars equally spaced by  $1\ \mu\text{m}$ . The image is acquired at 10 Hz using a scan trajectory based on input shaping. The height and deflection image is shown on the top left and right. The bottom plots show the cross sections of the height and deflection image. The scan range can be estimated as  $11.5 \times 12.5\ \mu\text{m}^2$ .

deflection signal (remaining control error). The bottom plots show the cross sections of the height and deflection signal.

As mentioned in Sec. 6.1.4, the feedback controller is user tuned by first increasing the I-gain until ringing is visible and then reducing the gain around 10%. The image in Fig. 6.14 and all following AFM images show the raw data without post-processing steps like leveling, filtering, rotating, cropping, or scaling [17]. Although post-processing is common in AFM imaging [17], the aim of this section is to show the pure scanner characteristics.

From the calibration standard the scan range can be estimated as  $11.5 \times 12.5\ \mu\text{m}^2$ . As the scan range of the fast scan axis is limited to the  $11.5\ \mu\text{m}$ , a calibration to the maximal possible square scan range is only possible by adjusting the amplitude of the slow scan axis to get the same  $11.5\ \mu\text{m}$  scan range. Therefore the maximal achievable square scan range is  $11.5 \times 11.5\ \mu\text{m}^2$ .

The grating appears stretched in x-direction on the left side as the scan speed increases from left to right due to the hysteresis of the x-scanner (cf. Fig. 6.8). Hysteresis can be corrected by calibration or sensorless techniques like charge control instead of controlling the actuation voltage [77]. Additionally a slight tilt of the imaging plane is visible. This can be corrected by two-dimensional plane fitting [17]. As expected for the slow scan rate of 10 Hz, distortions due to the system dynamics of the x- and y-scanner are not visible and the tracking bandwidth of the the vertical feedback loop is sufficient to follow the topography.

By increasing the line scan rate to 100 Hz, the limitation of the tracking bandwidth

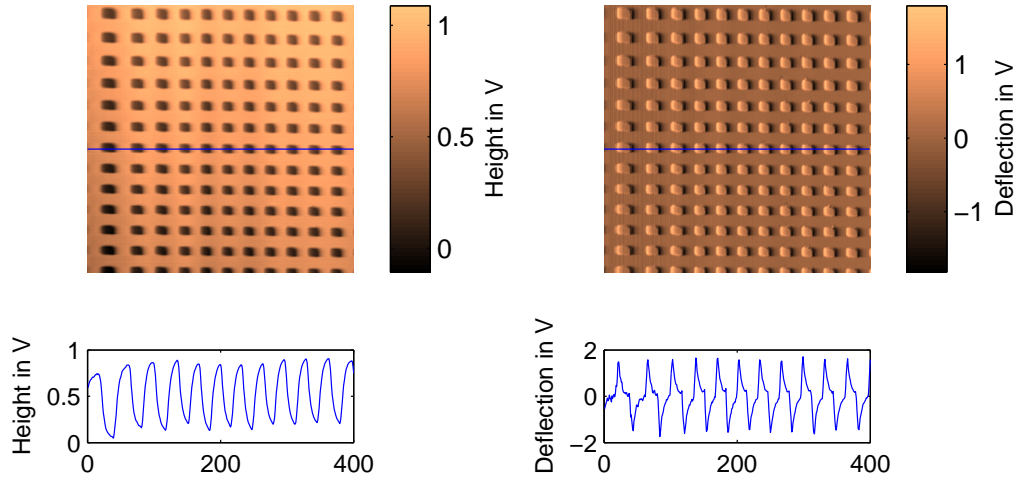


Figure 6.15: Image of a calibration standard with 45 nm high pillars equally spaced by  $1\ \mu\text{m}$ . The image is acquired at 100 Hz using a scan trajectory based on input shaping. The height and deflection image is shown on the top left and right. The bottom plots show the cross sections of the height and deflection image. There are no visible distortions due to the system dynamics. Vertical tracking is limited by the tracking bandwidth of the z-feedback loop.

of the z-feedback loop can be seen in Fig. 6.15. The frequency of steps occurring along the fast scan axis is 4.4 kHz. Further increasing the z-feedback gain leads to oscillations distorting the image. To avoid a limitation by the z-feedback loop, the scan range is reduced for higher lines scan rates. Although imaging is done with a line scan rate of 100 Hz, there are no visible distortions due to the system dynamics of the x- and y-scanner.

Scanning  $2.4 \times 2.4\ \mu\text{m}^2$  at line scan rate of 625 Hz is shown in Fig. 6.16. Distortions due to mechanical resonances excited by the scanning motion are mainly visible in the deflection image. Estimating the frequency of the vertical lines results in 15 kHz, which is close to the 2<sup>nd</sup> mechanical resonance of the x-scanner (cf. Fig. 6.5). As discussed in Sec. 6.2.2, the distortion due to the 2<sup>nd</sup> mechanical resonance occurs as the proposed input shaping method mainly suppresses the excitation of the first dominant mechanical resonance. Therefore the comparison of the images acquired at 100 Hz and 625 Hz shows that input shaping works well at a line scan rate of about 2% of the first dominant mechanical resonance, but is limited by the higher system dynamics when scanning at line scan rates around 10% of the first dominant mechanical resonance.

### Imaging with the optimization based scan trajectory

Fig. 6.17 shows a full range scan at a line scan rate of 100 Hz using the optimization based scan trajectory. As in Sec. 6.2.2, the optimization based scan trajectory is

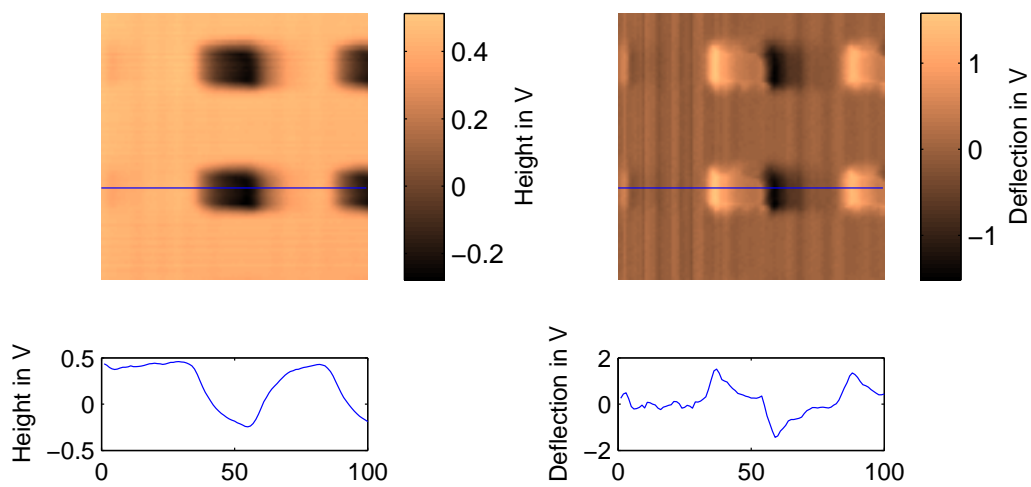


Figure 6.16: Image of a calibration standard with 45 nm high pillars equally spaced by  $1 \mu\text{m}$ . The image is acquired at 625 Hz using a scan trajectory based on input shaping. The height and deflection image is shown on the top left and right. The bottom plots show the cross sections of the height and deflection image. Distortions due to mechanical resonances excited by the scanning motion are clearly visible.

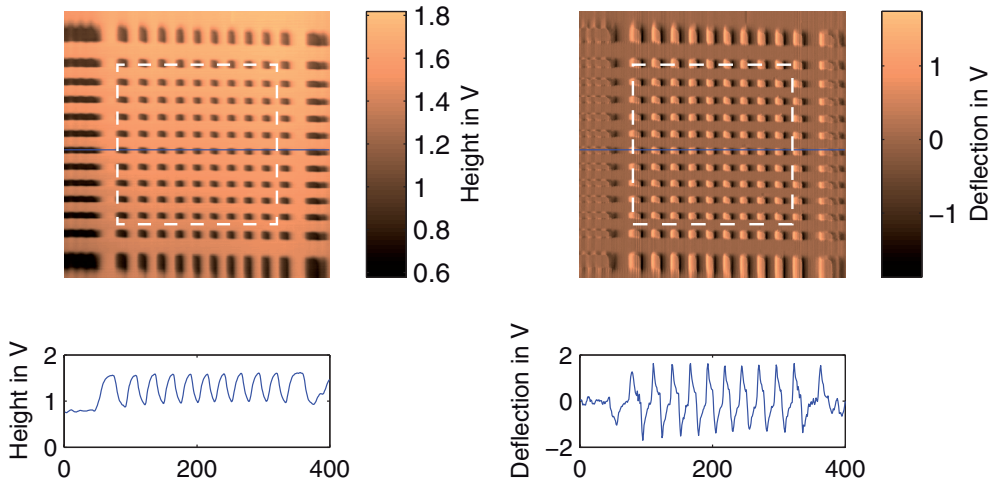


Figure 6.17: Image of a calibration standard with 45 nm high pillars equally spaced by  $1\ \mu\text{m}$ . The image is acquired at 100 Hz using the optimization based scan trajectory. The height and deflection image is shown on the top left and right. The bottom plots show the cross sections of the height and deflection image. The centered 60% are surrounded by the dashed square. The borders are distorted by the smooth turn around.

generated with the centered 60% of the scan range fixed to an ideal triangular signal and a cost accounting for harmonics above the 3<sup>rd</sup> one. The centered 60% of the image are surrounded by the dashed square.

In comparison to Fig. 6.15, the most obvious difference is the distortion near the image borders. As the scan trajectory is fixed to an ideal triangular signal within 60% of the scan range for each scan direction, the optimization algorithm smooths the turn around.

The biggest advantage of the optimization based scan trajectories can be seen by the comparison of Fig.6.16 and Fig.6.18, acquired at a line scan rate of 625 Hz. The image in Fig.6.18, acquired with the optimization based scan trajectory, does not show the distortions clearly visible in the image in Fig.6.16, acquired with the scan trajectory based on input shaping. Although it must be noted that one grating period is not sufficient to judge the lateral dynamics, it allows the comparison between the optimization based scan trajectory and input shaping. The comparison for this system with higher order dynamics shows that the optimization based approach is more suitable when scanning at line scan rates around 10% of the first dominant mechanical resonance.

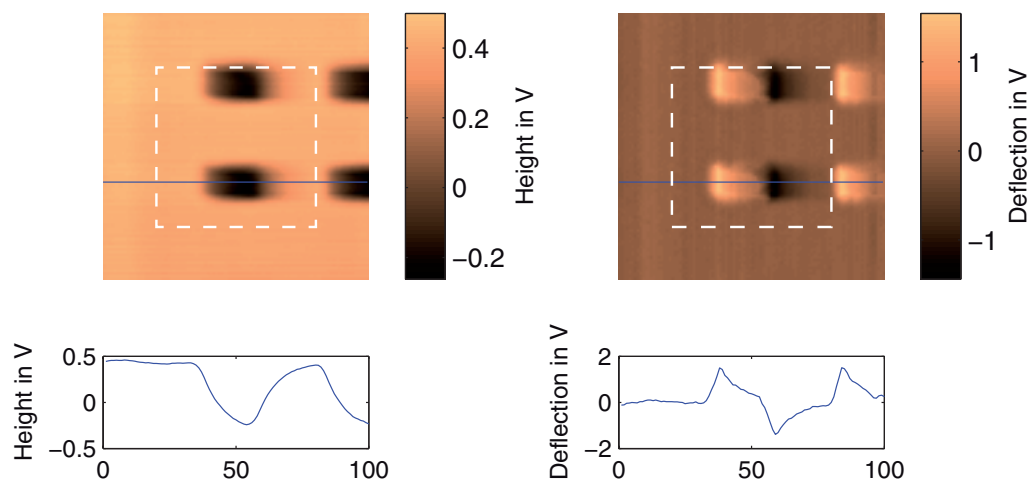


Figure 6.18: Image of a calibration standard with 45 nm high pillars equally spaced by  $1 \mu\text{m}$ . The image is acquired at 625 Hz using the optimization based scan trajectory. The height and deflection image is shown on the top left and right. The bottom plots show the cross sections of the height and deflection image. The centered 60% are surrounded by the dashed square. Compared to Fig. 6.16, distortions due to mechanical resonances are not visible.

## 6.4 Conclusion

In this Chapter, operating and validating the flexure-based scanning lever AFM designed in Chapter 5, is done. The overall setup with all additional components required to operate the scanning lever AFM is presented. System identification shows that all three scan axis have higher order dynamics.

The time domain response to two different scan trajectories which are already presented in literature [56][13] is measured. Using these two trajectories, slow, fast, and high speed scanning at 10, 100, and 625 Hz is shown. The first method called input shaping works well at a line scan rate of 100 Hz, what is about 2% of the first dominant mechanical resonance, but is limited by the higher order system dynamics when scanning at line scan rate of 625 Hz, what is around 10% of the first dominant mechanical resonance. The optimization based scan trajectories are more suitable for the system with higher order dynamics when scanning at high line scan rates around 10% of the first dominant mechanical resonance. As the main limitation of the presented system for high speed scanning is the tracking bandwidth of the vertical feedback loop, high speed scanning with a line scan rate of 625 Hz is successfully shown at a reduced scan range of  $2.4 \times 2.4 \mu\text{m}^2$ .

As the scanning lever design allows imaging of large samples in industry or imaging biological samples in petri dishes and high speed AFM imaging keeps the high throughput in industrial processes, enabling real time observation at the nanometer scale, this theses focuses on the design of a high speed scanning lever AFM. The missing knowledge for the design and integrating of the optical path into a high speed scanning lever AFM is addressed in four research questions:

- What are the bandwidth and resolution limiting factors for the optical beam deflection method used in AFMs?

The optical beam deflection method is commonly used in AFMs to measure the deflection of the cantilever. The possible bandwidth limiting components commonly used in the optical beam deflection measurement are the quadrant photodetector (QPD), the transimpedance amplifier, the summing and differential amplifiers, and the signal normalization.

Beside the special type of the QPD the response time is mainly determined by the reverse voltage and the size of the active area (see Sec. 3.1.3). In general the selection of a QPD with a small active area leads to a small junction capacitance. Additionally the junction capacitance is minimized by increasing the reverse voltage to the maximum rated value. Beside a reduction of the response time of the QPD itself, a small junction capacitance of the QPD is desired to gain the maximum possible bandwidth of the transimpedance amplifier (see Sec. 3.1.3). Even though operational amplifiers with a large gain bandwidth product can be utilized, the amplifier noise has to be considered (see Sec. 3.3.4).

If a high common-mode rejection ratio is not beneficial, the utilization of an instrumentation amplifier should be avoided since it usually has a small bandwidth with not more than 15 MHz (see Sec. 3.1.1). Additionally the bandwidth limiting signal normalization should be avoided as the expected reduction of noise can be neglected (see Sec. 3.1.2). It is usually unnecessary to normalize the signal

## 7 Conclusions

at the same bandwidth as the deflection is measured, as major changes in the total irradiation are expected only at discrete events for example if the cantilever is changed (see Sec. 3.1.2). The adaption of the feedback gain according to the total irradiance on the QPD can be done upfront to the measurement.

It is shown that systematically selecting and matching the components of the deflection readout leads to a  $-3$  dB bandwidth of 64.5 MHz (see Sec. 3.3.7) at an estimated deflection noise density of  $62 \text{ fm}/\sqrt{\text{Hz}}$  (see Sec. 3.3.8), what is more than three times the fastest deflection readout bandwidth reported in literature so far [29].

- Does the vertical displacement of the cantilever influence the deflection measurement and to which extent crosstalk has to be considered?

If the deflection is compensated by a vertical displacement of the cantilever, the distance between the laser source and the cantilever as well as the distance between the cantilever and the QPD changes. In addition the beam reflected from the back of the cantilever is shifted in parallel, resulting in a displacement on the QPD. This displacement is measured as a false deflection on the QPD, resulting in crosstalk from the compensating movement of the cantilever to the deflection readout.

For a cantilever of length  $l = 200 \mu\text{m}$  and a distance  $s = 30 \text{ mm}$  between the cantilever and the QPD the crosstalk between the compensating movement and the deflection readout is  $10^{-3}$  (see Sec. 4.1). If the controller compensates the false deflection, the force between the tip and the sample varies. A compensating movement of  $1 \mu\text{m}$  leads to a false deflection of  $1 \text{ nm}$  what results in a force variation of  $10^{-9} \text{ N}$  for a cantilever with a stiffness of  $1 \text{ N/m}$ , what changes the pressure on a tip with a radius of  $1 \text{ nm}$  by approximately  $0.32 \text{ GPa}$  (see Sec. 4.1).

Chapter 4 shows that an additional focusing lens between the cantilever and the QPD can compensate for the crosstalk and furthermore gives an additional design freedom for the spot size on the cantilever. Even for a laser beam focused on the cantilever, the additional focusing lens enables the utilization of a small QPD with a low junction capacitance for a high deflection readout bandwidth, independent of the required spot size on the cantilever and the minimum distance between the cantilever and the QPD.

- Can the optical beam deflection method be applied to flexure-based (in plane movement) scanning lever AFMs without the need to move the laser source, the detector, and the alignment mechanisms?

Using the optical beam deflection method in a scanning lever AFM, the laser spot has to track the x-, y-, and z-movement of the cantilever. The obvious approach of scanning the whole AFM head including the laser source, the focusing optics, the detector, and the alignment mechanisms, is not suitable for high speed scanning as the total moved mass increases and therefore the first dominant mechanical resonance occurs at lower frequencies. With a fixed laser source and alignment mechanism, an additional tracking mechanism is necessary to keep the laser spot on the moving cantilever.

## 7 Conclusions

In Chapter 5 it is shown that tracking the cantilever can be done by folding the optical path according to the serial scanner configuration. The proposed method requires a serial design, as the single actuators are not separated in a parallel design and therefore folding the optical path according to the actuation directions is not possible. It is shown that the optical beam deflection method can be applied to flexure-based scanning lever AFMs without moving the laser source, the detector, and the alignment mechanisms.

- Can the flexure-based scanning lever AFM with the optical beam deflection method be used for high speed scanning?

In Chapter 6, two different types of scan trajectories, which are already presented in literature [56][13], used for slow, fast, and high speed scanning at 10, 100, and 625 Hz.

The first method called input shaping works well at a line scan rate of 100 Hz, what is about 2% of the first dominant mechanical resonance, but is limited by the higher order system dynamics when scanning at line scan rate of 625 Hz, what is around 10% of the first dominant mechanical resonance. The second method uses optimization based scan trajectories which are more suitable for the system with higher order dynamics when scanning at line scan rate around 10% of the first dominant mechanical resonance. High speed scanning with a line scan rate of 625 Hz is successfully shown at a scan range of  $2.4 \times 2.4 \mu\text{m}^2$  in Sec. 6.3.

An improved tracking accuracy is expected by adding additional feedback control to the x- and y-scan stage. As position sensors must be available to enable feedback control, the integrated position sensors of the nanopositioning stage NPXY100-100 (nPoint, Middleton, US-WI) can be utilized for the y-scan direction while an additional sensor is necessary for the x-scan direction.

The additional feedback controller can be used to extend the implemented feedforward approach to a two-degrees of freedom control. Although the tracking accuracy can be increased, feedback noise as well as noise from the position sensors has to be considered. As the scanning motion is repetitive, another method combining feed-forward control with the sensor signal is iterative learning control [72][73]. By using iterative learning control, the feedforward trajectory is optimized based on the sensor signal of previous trails.

In the actual design of the z-scanner a higher feedback bandwidth can be achieved by using model based feedback control instead of the conventional PI controller [78][79][44][55]. Another possibility to increase the feedback bandwidth is actively damping the scanner resonances [55]. Based on the similarities of consecutive scan lines the tracking error can be reduced by combining feedforward and feedback control [80].

Realizing a fully integrated serial scanner design based on the actual prototype will result in a more compact and stiff design. By reducing the mass while stiffening the structure the mechanical resonances are shifted towards higher frequencies. This will result in high speed scanning lever AFM that enables imaging of a wide variety of samples independent of the sample size and sample mass.

---

## Bibliography

---

- [1] E. Abbe, “Beiträge zur theorie des mikroskops und der mikroskopischen wahrnehmung,” *Archiv für mikroskopische Anatomie*, vol. 9, no. 1, pp. 413–418, 1873.
- [2] G. Binnig, H. Rohrer, C. Gerber, and E. Weibel, “Surface studies by scanning tunneling microscopy,” *Physical review letters*, vol. 49, no. 1, p. 57, 1982.
- [3] “Press release: The 1986 nobel prize in physics.”
- [4] G. Binnig, C. F. Quate, and C. Gerber, “Atomic force microscope,” *Physical review letters*, vol. 56, no. 9, pp. 930–933, 1986.
- [5] D. Sarid, *Scanning Force Microscopy*. New York: Oxford University Press, 1994.
- [6] G. Meyer and N. M. Amer, “Novel optical approach to atomic force microscopy,” *Applied Physics Letters*, vol. 53, no. 12, p. 1045, 1988.
- [7] S. Alexander, L. Hellemans, O. Marti, J. Schneir, V. Elings, P. K. Hansma, M. Longmire, and J. Gurley, “An atomic-resolution atomic-force microscope implemented using an optical lever,” *Journal of Applied Physics*, vol. 65, no. 1, p. 164, 1989.
- [8] G. Binnig and D. Smith, “Single-tube three-dimensional scanner for scanning tunneling microscopy,” *Review of Scientific Instruments*, vol. 57, no. 8, pp. 1688–1689, 1986.
- [9] B. Drake, C. Prater, A. Weisenhorn, S. Gould, T. Albrecht, C. Quate, D. Cannell, H. Hansma, and P. Hansma, “Imaging crystals, polymers, and processes in water with the atomic force microscope,” *Science*, vol. 243, no. 4898, pp. 1586–1589, 1989.
- [10] Y. Xu, S. Smith, and P. Atherton, “A metrological scanning force microscope,” *Precision Engineering*, vol. 19, no. 1, pp. 46 – 55, 1996.

## Bibliography

- [11] Y. K. Yong, S. O. R. Moheimani, B. J. Kenton, and K. K. Leang, “Invited review article: High-speed flexure-guided nanopositioning: Mechanical design and control issues,” *Review of Scientific Instruments*, vol. 83, no. 12, p. 121101, 2012.
- [12] P. K. Hansma, G. Schitter, G. E. Fantner, and C. Prater, “High-speed atomic force microscopy,” *Science*, vol. 314, no. 5799, pp. 601–602, 2006.
- [13] R. Munnig Schmidt, G. Schitter, and J. v. Eijk, *The Design of High Performance Mechatronics*. Amsterdam, The Netherlands: Delft University Press, 2011.
- [14] N. Phan, C. Cusworth, and C. Prater, “Fast-scanning spm scanner and method of operating same,” US Patent 8,166,567 B2, 2012.
- [15] C. Prater, J. Massie, D. Grigg, V. Elings, P. Hansma, and B. Drake, “Scanning stylus atomic force microscope with cantilever tracking and optical access,” US Patent 5,463,897, 1995.
- [16] A. D. L. Humphris, M. J. Miles, and J. K. Hobbs, “A mechanical microscope: High-speed atomic force microscopy,” *Applied Physics Letters*, vol. 86, no. 3, p. 034106, 2005.
- [17] P. Eaton and P. West, *Atomic force microscopy*. New York: Oxford Univ. Press, 2010.
- [18] G. Schitter, J. Steininger, F. C. Heuck, and U. Staufer, “Towards fast afm-based nanometrology and nanomanufacturing,” *International Journal of Nanomanufacturing*, vol. 8, no. 5, pp. 392–418, 2012.
- [19] Q. Zhong, D. Inniss, K. Kjoller, and V. Elings, “Fractured polymer/silica fiber surface studied by tapping mode atomic force microscopy,” *Surface Science Letters*, vol. 290, no. 1-2, pp. L688 – L692, 1993.
- [20] T. Albrecht, P. Grütter, D. Horne, and D. Rugar, “Frequency modulation detection using high-q cantilevers for enhanced force microscope sensitivity,” *Journal of Applied Physics*, vol. 69, no. 2, pp. 668–673, 1991.
- [21] N. Burnham, O. Behrend, F. Oulevey, G. Gremaud, P. Gallo, D. Gourdon, E. Dupas, A. Kulik, H. Pollock, and G. Briggs, “How does a tip tap?” *Nanotechnology*, vol. 8, no. 2, p. 67, 1997.
- [22] L. Nony, R. Boisgard, and J. P. Aimé, “Nonlinear dynamical properties of an oscillating tip–cantilever system in the tapping mode,” *The Journal of Chemical Physics*, vol. 111, no. 4, pp. 1615–1627, 1999.
- [23] R. W. Stark and W. M. Heckl, “Higher harmonics imaging in tapping-mode atomic-force microscopy,” *Review of Scientific Instruments*, vol. 74, no. 12, pp. 5111–5114, 2003.

## Bibliography

- [24] R. W. Stark, T. Drobek, and W. M. Heckl, “Tapping-mode atomic force microscopy and phase-imaging in higher eigenmodes,” *Applied Physics Letters*, vol. 74, no. 22, pp. 3296–3298, 1999.
- [25] A. Ulcinas and V. Snitka, “Intermittent contact afm using the higher modes of weak cantilever,” *Ultramicroscopy*, vol. 86, no. 1-2, pp. 217 – 222, 2001.
- [26] M. Nonnenmacher, M. o’Boyle, and H. Wickramasinghe, “Kelvin probe force microscopy,” *Applied Physics Letters*, vol. 58, no. 25, pp. 2921–2923, 1991.
- [27] J. Saenz, N. Garcia, P. Grütter, E. Meyer, H. Heinzelmann, R. Wiesendanger, L. Rosenthaler, H. Hidber, and H.-J. Güntherodt, “Observation of magnetic forces by the atomic force microscope,” *Journal of Applied Physics*, vol. 62, no. 10, pp. 4293–4295, 1987.
- [28] H.-J. Butt and M. Jaschke, “Calculation of thermal noise in atomic force microscopy,” *Nanotechnology*, vol. 6, no. 1, p. 1, 1995.
- [29] R. Enning, D. Ziegler, A. Nievergelt, R. Friedlos, K. Venkataramani, and A. Stemmer, “A high frequency sensor for optical beam deflection atomic force microscopy,” *Review of Scientific Instruments*, vol. 82, no. 4, p. 043705, 2011.
- [30] G. Binnig, C. Gerber, E. Stoll, T. R. Albrecht, and C. F. Quate, “Atomic resolution with atomic force microscope,” *EPL (Europhysics Letters)*, vol. 3, no. 12, p. 1281, 1987.
- [31] T. Göddenhenrich, H. Lemke, U. Hartmann, and C. Heiden, “Force microscope with capacitive displacement detection,” *Journal of Vacuum Science & Technology A*, vol. 8, no. 1, pp. 383–387, 1990.
- [32] C. M. Mate, G. M. McClelland, R. Erlandsson, and S. Chiang, “Atomic-scale friction of a tungsten tip on a graphite surface,” *Physical review letters*, vol. 59, no. 17, pp. 1942–1945, 1987.
- [33] Y. Martin, C. C. Williams, and H. K. Wickramasinghe, “Atomic force microscope–force mapping and profiling on a sub 100-Å scale,” *Journal of Applied Physics*, vol. 61, no. 10, pp. 4723–4729, 1987.
- [34] D. Rugar, H. J. Mamin, R. Erlandsson, J. E. Stern, and B. D. Terris, “Force microscope using a fiber-optic displacement sensor,” *Review of Scientific Instruments*, vol. 59, no. 11, pp. 2337–2340, 1988.
- [35] D. Iannuzzi, S. Deladi, V. J. Gadgil, R. G. P. Sanders, H. Schreuders, and M. C. Elwenspoek, “Monolithic fiber-top sensor for critical environments and standard applications,” *Applied Physics Letters*, vol. 88, no. 5, p. 053501, 2006.
- [36] G. Gruca, S. de Man, M. Slaman, J. H. Rector, and D. Iannuzzi, “Ferrule-top micromachined devices: design, fabrication, performance,” *Measurement Science and Technology*, vol. 21, no. 9, p. 094033, 2010.

## Bibliography

- [37] P. I. Chang, D. Chavan, R. Paris, D. Iannuzzi, and G. Schitter, "Towards high speed ferrule-top atomic force microscopy," in *6th IFAC Symposium on Mechatronic Systems*, Hangzhou, China, 2013, pp. 131–137.
- [38] T. Fukuma, M. Kimura, K. Kobayashi, K. Matsushige, and H. Yamada, "Development of low noise cantilever deflection sensor for multienvironment frequency-modulation atomic force microscopy," *Review of Scientific Instruments*, vol. 76, no. 5, p. 053704, 2005.
- [39] M. Ojima, A. Arimoto, N. Chinone, T. Gotoh, and K. Aiki, "Diode laser noise at video frequencies in optical videodisc players," *Applied optics*, vol. 25, no. 9, pp. 1404–1410, 1986.
- [40] A. Arimoto, M. Ojima, N. Chinone, A. Oishi, T. Gotoh, and N. Ohnuki, "Optimum conditions for the high frequency noise reduction method in optical videodisc players," *Applied optics*, vol. 25, no. 9, pp. 1398–1403, 1986.
- [41] G. Schitter, F. Allgöwer, and A. Stemmer, "A new control strategy for high-speed atomic force microscopy," *Nanotechnology*, vol. 15, no. 1, p. 108, 2004.
- [42] T. Ando, N. Kodera, E. Takai, D. Maruyama, K. Saito, and A. Toda, "A high-speed atomic force microscope for studying biological macromolecules," *Proceedings of the national academy of sciences*, vol. 98, no. 22, pp. 12 468–12 472, 2001.
- [43] J. H. Kindt, G. E. Fantner, J. A. Cutroni, and P. K. Hansma, "Rigid design of fast scanning probe microscopes using finite element analysis," *Ultramicroscopy*, vol. 100, no. 3, pp. 259–265, 2004.
- [44] G. Schitter, K. J. Astrom, B. E. DeMartini, P. J. Thurner, K. L. Turner, and P. K. Hansma, "Design and modeling of a high-speed afm-scanner," *Control Systems Technology, IEEE Transactions on*, vol. 15, no. 5, pp. 906–915, 2007.
- [45] T. Fukuma, Y. Okazaki, N. Kodera, T. Uchihashi, and T. Ando, "High resonance frequency force microscope scanner using inertia balance support." *American Institute of Physics*, vol. 92, no. 24, pp. 243 119–243 121, 2008.
- [46] I. Bozchalooi, K. Youcef-Toumi, D. Burns, and G. Fantner, "Compensator design for improved counterbalancing in high speed atomic force microscopy," *Review of Scientific Instruments*, vol. 82, no. 11, p. 113712, 2011.
- [47] T. Sulchek, S. C. Minne, J. D. Adams, D. A. Fletcher, A. Atalar, C. F. Quate, and D. M. Adderton, "Dual integrated actuators for extended range high speed atomic force microscopy," *Applied Physics Letters*, vol. 75, no. 11, p. 1637, 1999.
- [48] G. Schitter, "Improving the speed of afm by mechatronic design and modern control methods," *Technisches Messen*, vol. 76, no. 5, pp. 266–273, 2009.
- [49] A. J. Fleming, "Dual-stage vertical feedback for high-speed scanning probe microscopy," *Control Systems Technology, IEEE Transactions on*, vol. 19, no. 1, pp. 156–165, 2011.

## Bibliography

- [50] B. J. Kenton and K. K. Leang, "Design and control of a three-axis serial-kinematic high-bandwidth nanopositioner," *Mechatronics, IEEE/ASME Transactions on*, vol. 17, no. 2, pp. 356–369, 2012.
- [51] D. Croft, G. Shed, and S. Devasia, "Creep, hysteresis, and vibration compensation for piezoactuators: atomic force microscopy application," *Journal of Dynamic Systems, Measurement, and Control*, vol. 123, no. 1, pp. 35–43, 2001.
- [52] G. Schitter and A. Stemmer, "Identification and open-loop tracking control of a piezoelectric tube scanner for high-speed scanning-probe microscopy," *Control Systems Technology, IEEE Transactions on*, vol. 12, no. 3, pp. 449–454, 2004.
- [53] O. M. El Rifai and K. Youcef-Toumi, "Coupling in piezoelectric tube scanners used in scanning probe microscopes," in *Proceedings of the 2001 American Control Conference*. IEEE, 2001, pp. 3251–3255.
- [54] G. E. Fantner, G. Schitter, J. H. Kindt, T. Ivanov, K. Ivanova, R. Patel, N. Holtzen-Andersen, J. Adams, P. J. Thurner, I. W. Rangelow *et al.*, "Components for high speed atomic force microscopy," *Ultramicroscopy*, vol. 106, no. 8, pp. 881–887, 2006.
- [55] T. Ando, "Control techniques in high-speed atomic force microscopy," in *American Control Conference, 2008*. IEEE, 2008, pp. 3194–3200.
- [56] A. Fleming and A. Wills, "Optimal periodic trajectories for band-limited systems," *Control Systems Technology, IEEE Transactions on*, vol. 17, no. 3, pp. 552–562, May 2009.
- [57] S. Salapaka, A. Sebastian, J. P. Cleveland, and M. V. Salapaka, "High bandwidth nano-positioner: A robust control approach," *Review of scientific instruments*, vol. 73, no. 9, pp. 3232–3241, 2002.
- [58] A. Sebastian and S. M. Salapaka, "Design methodologies for robust nano-positioning," *Control Systems Technology, IEEE Transactions on*, vol. 13, no. 6, pp. 868–876, 2005.
- [59] J. A. Butterworth, L. Y. Pao, and D. Y. Abramovitch, "A comparison of control architectures for atomic force microscopes," *Asian Journal of Control*, vol. 11, no. 2, pp. 175–181, 2009.
- [60] J. Steininger, M. Bibl, H. W. Yoo, and G. Schitter, "High bandwidth deflection readout for atomic force microscopes," *Review of Scientific Instruments*, vol. 86, no. 10, p. 103701, 2015.
- [61] *Low Power, 1 nV/sqrt(Hz), G<sub>v</sub> ≥ 10 Stable, Rail-to-Rail Output Amplifier, ADA4895-1/ADA4895-2*, Analog Devices, 2015, rev. B.
- [62] J. Steininger and G. Schitter, "Influence of the photodetector geometry on the deflection measurement in atomic force microscopes," in *Proceedings, ASPE 2014 Annual Meeting*, 2014, pp. 674–679.

## Bibliography

- [63] E. Hecht, *Optics: Pearson New International Edition*. London, United Kingdom: Pearson Education Limited, 2013.
- [64] T. E. Schaeffer, “Force spectroscopy with a large dynamic range using small cantilevers and an array qpd,” *Journal of Applied Physics*, vol. 91, no. 7, pp. 4739–4746, 2002.
- [65] “IEC60825 - safety of laser products - part 1: Equipment classification and requirements,” 05 2014.
- [66] J. Steininger, R. Paris, and G. Schitter, “Increasing sensitivity while reducing crosstalk of the force sensor in atomic force microscopes,” in *Proceedings of the 14th euspen International Conference*, R. Leach, Ed., vol. I, Jun 2014, pp. 321–324.
- [67] C. A. J. Putman, B. G. De Groot, N. F. V. Hulst, and J. Greve, “A detailed analysis of the optical beam deflection technique for use in atomic force microscopy,” *Journal of Applied Physics*, vol. 72, no. 1, pp. 6–12, 1992.
- [68] A. S. Householder, “Unitary triangularization of a nonsymmetric matrix,” *Journal of the ACM (JACM)*, vol. 5, no. 4, pp. 339–342, 1958.
- [69] B. J. Kenton, A. J. Fleming, and K. K. Leang, “Compact ultra-fast vertical nanopositioner for improving scanning probe microscope scan speed,” *Review of Scientific Instruments*, vol. 82, no. 12, p. 123703, 2011.
- [70] K. Grothe and J. Feldhusen, Eds., *Dubbel, Taschenbuch für den Maschinenbau*. Berlin, Germany: Springer Vieweg, 2014.
- [71] D. Neyer, “Duale aktuation in nanositioniersystemen,” MSc thesis, ACIN, TU Wien, Vienna, Austria, 2015.
- [72] Q. Zou, K. Leang, E. Sadoun, M. Reed, and S. Devasia, “Control issues in high-speed afm for biological applications: Collagen imaging example,” *Asian Journal of Control*, vol. 6, no. 2, pp. 164–178, 2004.
- [73] K. K. Leang and S. Devasia, “Design of hysteresis-compensating iterative learning control for piezo-positioners: Application to atomic force microscopes,” *Mechatronics*, vol. 16, no. 3, pp. 141–158, 2006.
- [74] R. Fletcher, *Practical methods of optimization*. Chichester, United Kingdom: Wiley, 1987.
- [75] T. Yamaguchi, M. Hirata, and J. C. K. Pang, *High-speed precision motion control*. Boca Raton: CRC press, 2011.
- [76] G. Schitter, P. J. Thurner, and P. K. Hansma, “Design and input-shaping control of a novel scanner for high-speed atomic force microscopy,” *Mechatronics*, vol. 18, no. 5, pp. 282–288, 2008.

## Bibliography

- [77] A. J. Fleming and S. R. Moheimani, "Sensorless vibration suppression and scan compensation for piezoelectric tube nanopositioners," *Control Systems Technology, IEEE Transactions on*, vol. 14, no. 1, pp. 33–44, 2006.
- [78] G. Schitter, P. Menold, H. Knapp, F. Allgöwer, and A. Stemmer, "High performance feedback for fast scanning atomic force microscopes," *Review of Scientific Instruments*, vol. 72, no. 8, pp. 3320–3327, 2001.
- [79] S. Devasia, E. Eleftheriou, and S. R. Moheimani, "A survey of control issues in nanopositioning," *Control Systems Technology, IEEE Transactions on*, vol. 15, no. 5, pp. 802–823, 2007.
- [80] G. Schitter, A. Stemmer, and F. Allgöwer, "Robust two-degree-of-freedom control of an atomic force microscope," *Asian Journal of Control*, vol. 6, no. 2, pp. 156–163, 2004.